Chapter One
Introduction

1.1 History and future of semiconductor industry

Over the last few years, microelectronic components have become more and more involved in our lives. They are used in almost everything, from watches to space shuttles. They are used in the control of nearly everything: medical appliances, cars, airplanes, and power plants. And they are used in all the communication systems such as, phones, radios, and fax machines.

Computers are a clear example of the importance of microelectronics. They are used almost everywhere from military bases to department stores. Not very long ago computers were huge boxes that could not do very complex calculations. Now computers are much smaller and can do much more.

The key innovation that permitted this wide use of microelectronics is the invention of the monolithic integrated circuits by Jack Kilby and Robert Noyce in 1960. The dramatic increase in performance and cost reduction in the electronics industry is attributable to innovations in integrated circuit fabrication process. Integrated circuits (ICs) are silicon chips that are doing the job of a very large number of transistors connected together in an electrical circuit. Most of an IC physical volume is the metallic wires connecting the chip

itself with the other component of the electric circuit. The chip itself is a much smaller and composed of n-type, p-type silicon, and other silicon layers.

As the IC becomes smaller, more functionality can be built into the same size chip, or the functionality can be obtained in a smaller size. Research in this size reduction is very rapid, as one can tell by checking the price of computers. The prices of computers have dropped very significantly in a very short period: the new systems are much faster, smaller, lighter, and can do much more than the older ones.

1.2 Lithography

The process used in manufacturing ICs is called lithography. The word lithography is defined in Webster as "the art or process of putting writing or designs on stone with a greasy material and producing printed impressions therefrom: also any process based on the same principal, as one using zinc, aluminum, or some other substance instead of stone". Webster's definition is a reasonable description of the art as it is practiced in the semiconductor industry even though the definition was written many years before the advent of the semiconductor device. The lithography process consists of transferring the desired pattern (i.e., the electrical circuit) to the chip by the use of what is called a mask. The process can also be described as transferring an image onto a receptive surface by shining light through the non-opaque portions of a pattern on a mask. The mask is the masterpiece containing the electrical circuit, desired to be printed many times to produce many chips. The lithography process consists of many steps. Starting from a blank

silicon wafer, the first step is the deposition process, where a layer of either electrically insulating or electrically conductive material (i.e., metal, polysilicon or oxide) is deposited on the surface of a silicon wafer. The circuits image is exposed on the surface of the deposited layer on the mask in the lithographic imaging process, then some material will be removed from the area exposed with photomask image in the etching process, in which. The process is repeated as many times as the number of layers needed to complete the computer chip. Figure 1.1 shows the main steps of the lithographic process.

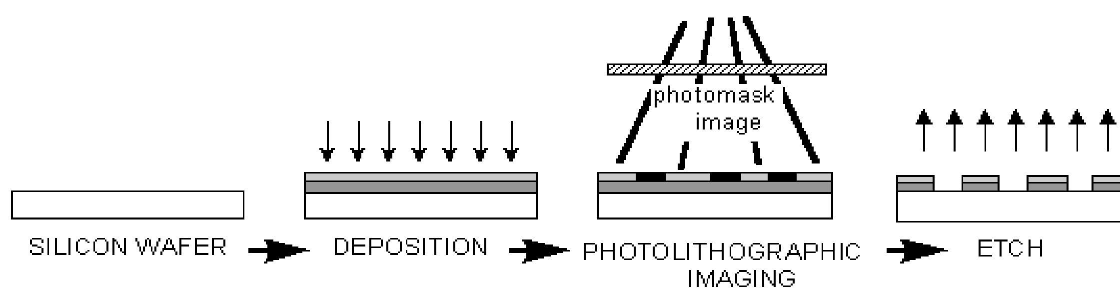

Figure 1.1. Schematic of the lithography process [ref. 1.1].

A lithographic system includes exposure tool, mask, resist, and all of the processing steps to accomplish pattern transfer from a mask to a wafer. Using lithography, a mask pattern can be rapidly replicated to produce many chips. The type of lithographic process used determines the throughput and the final cost of the electronic component.

The lithographic minimum printable size is very important, as it directly influences the size, speed, and performance of the chips, their associated packages, and hence, the computer systems. As the accuracy of imaging increases, smaller features can be used: hence the minimum printable size is decreased.

Figure 1.2 shows some features obtained by optical lithography, the feature thickness is almost 0.25 μm. Also it shows the map of the world printed in an area of 1.2 μm by 0.9 μm.

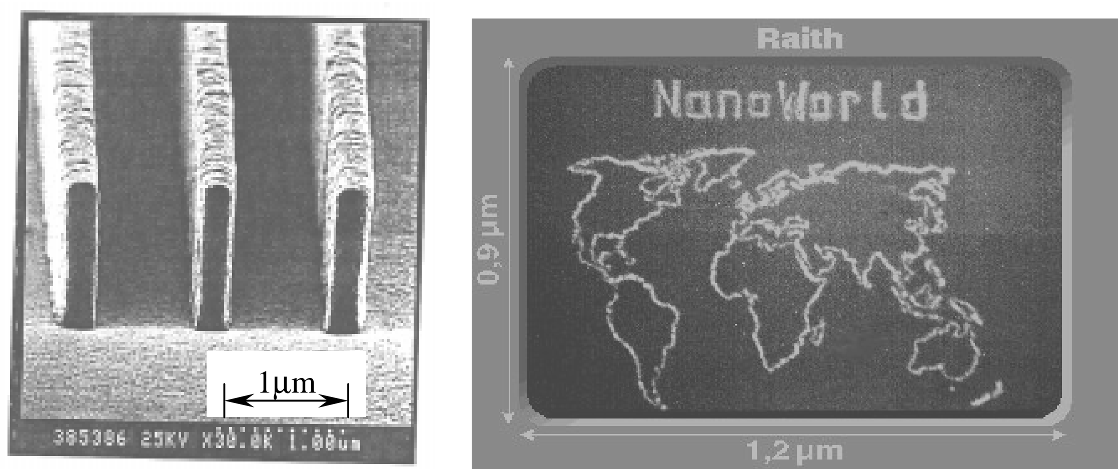

Figure 1.2. The lithography process needs really small feature sizes [ref.1.1].

1.3 Optical lithography

Lithography methods are categorized as, optical lithography, X-ray lithography, ion-beam lithography, electron-beam lithography (SCALPEL), and extreme ultraviolet (EUV) lithography. Optical lithography is the oldest method in IC manufacturing and is currently the only commercial method used to manufacture semiconductors. The other four are candidates for the next generation lithography manufacturing methods.

From the late 1960s, when integrated circuits had line-widths of 5 μm, to 1997, when the minimum line-widths reached 0.35 μm in 64Mb DRAM circuits, optical lithography was

ubiquitously used for manufacturing [ref. 1.2]. This dominance of optical lithography in production is the result of a worldwide effort to improve optical exposure tools and resists. Although lithography system costs (which are typically more than one third the cost of processing a wafer to completion) increase, as minimum feature size on a semiconductor chip decreases, optical lithography remains attractive because of its high wafer throughput.

Figure 1.3 shows the limitation of the feature size, which can be achieved using optical lithography and other technologies.

Optical lithography has a limit for minimum feature size. The size of a feature that can be printed by photolithography is limited by the wavelength of the exposing radiation just as the resolution of an optical microscope is limited by the wavelength of the "white" light used for imaging. Photolithography systems can print about 1.3 times the exposure wavelength in size. Resolution can always be improved by shifting to shorter wavelengths, but we must also take into account that some times the material used may be opaque at those wavelengths [ref. 1.4].

From the chart in Figure 1.3, one can see that to manufacture features smaller than 0.10 μm, the chip industry must choose from several non-optical lithography options. Selecting one technology as early as possible is critical to accelerating development and minimizing industry costs.

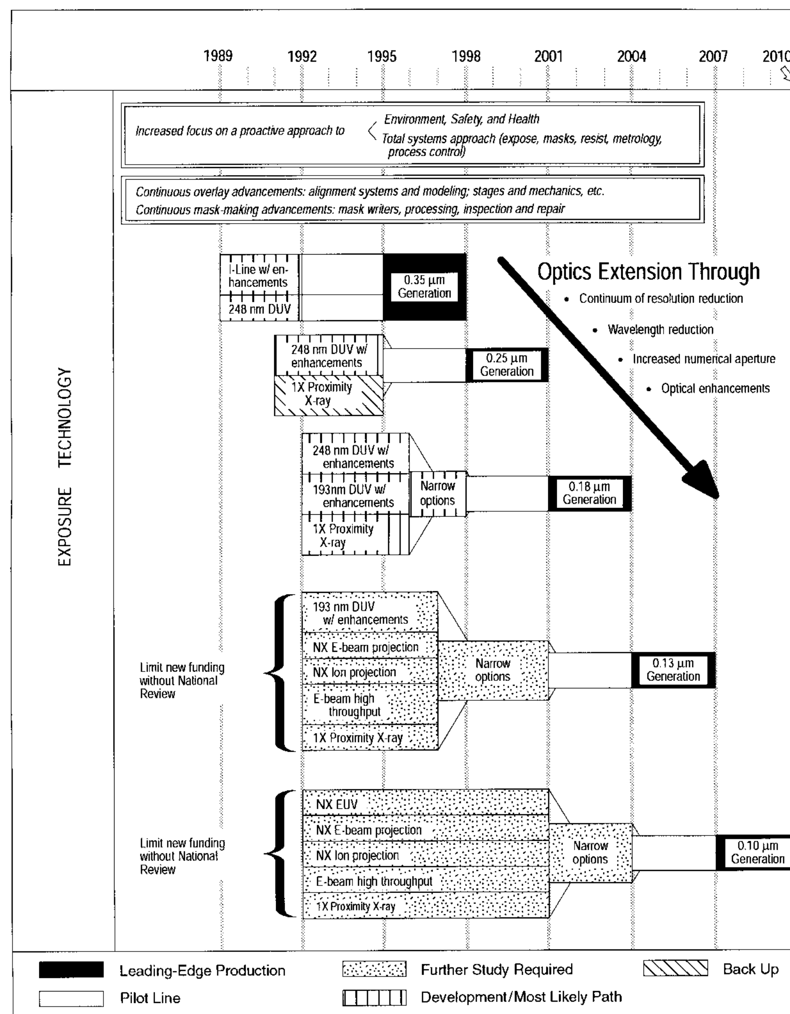

Figure 1.3. Exposure Technology Roadmap by the Semiconductor Industry Association [1.3].

To understand how optical lithography works, one must look at how a simple transistor is manufactured [ref. 1.4]. Figure 1.4 shows the main steps in the manufacture of a transistor using optical lithography.

The process sequence for producing the first two levels of a transistor (or an integrated circuit) with a negative resist is as follows:

(a) First masking. The silicon substrate is coated first with silicon dioxide, which does not conduct electricity, and then with a photoresist. The photoresist is a thin coating applied over the silicon dioxide and subsequently exposed (through the mask) such that when shining a light through a patterned mask, it strikes selected areas of the photoresist material.

The exposed photoresist is then subjected to a development step, which generally involves immersion in an appropriate solvent (step b). Depending upon the chemical nature of the photoresist, the exposed areas may be rendered more soluble in the developing solvent than the unexposed areas, thereby producing, what is so called, a positive tone image of the mask. Or conversely the exposed areas may be rendered less soluble, producing a negative tone image of the mask. The net effect of this process is to produce a three dimensional relief image in the photoresist material that is a replication of the opaque and transparent areas on the mask.

(b) First etching. A solvent dissolves the unexposed layer of photoresist, uncovering part of the silicon dioxide. Next, the silicon dioxide is chemically etched. The hardened photoresist is then dissolved to leave a ridge of silicon dioxide.

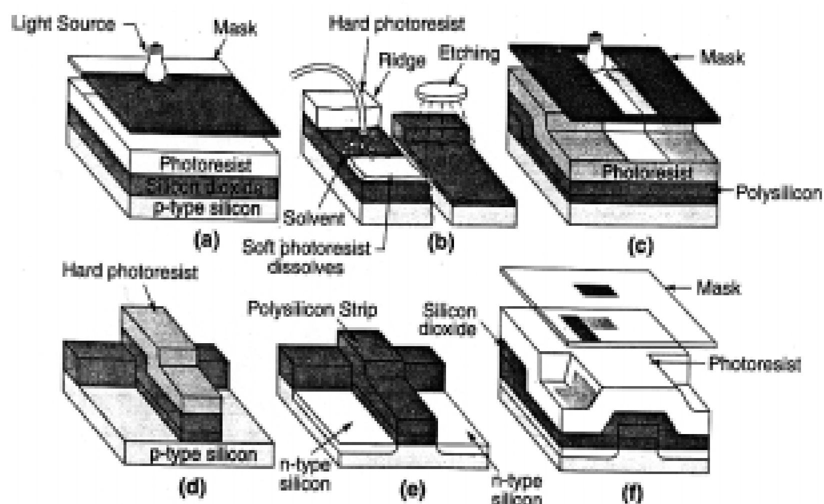

Figure 1.4. Process of manufacturing of a transistor chip [ref. 1.4].

(c) Second masking. Layers of polysilicon, which conduct electricity, and photoresist are applied, and a second masking operation is then executed.

(d) Second etching. The unexposed photoresist is dissolved, and another etching treatment removes the polysilicon and silicon.

(e) Doping. The hard photoresist is removed. Now the layers undergo an operation called doping, which transforms the newly revealed strips of p-type silicon into n-type silicon.

(f) Third masking and etching. Layers of silicon dioxide and photoresist are added. Masking and etching create holes through the layers to the doped silicon and central polysilicon strip. The final product is a three-dimensional transistor as shown in Figure 1.5.

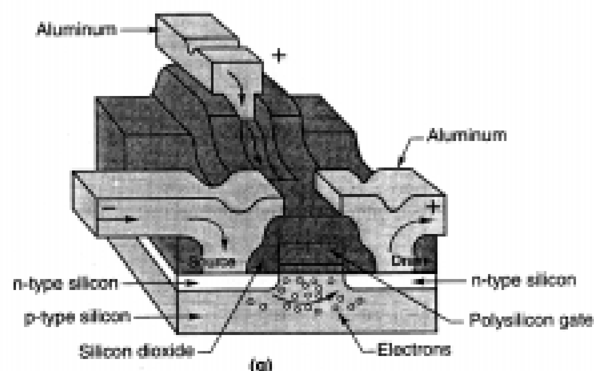

Figure 1.5. A transistor chip [ref. 1.4].

1.4. Objective of this work

Optical lithography still has some technical advantages over all other possible replacement technologies for next generation manufacturing processes. Also, the cost of switching from optical lithography to any other technology will be very large. Consequently, it is important to extend the use of optical lithography as much as possible. In the meantime, research will continue to determine which one of the new technologies is the best replacement for the next generation use.

To extend the use of optical lithography, with even smaller feature sizes, two things may be done. One is to improve the accuracy of the process (i.e., the imaging resolution) and the other is to reduce distortion produced during the manufacturing process due to loading conditions (such as mounting, thermal environment, and others).

Alternative lithographic techniques to improve the accuracy of the imaging process are based on the idea that the minimum feature size is a function of the wavelength of the

lighting source. Thus, continuously decreasing the wavelength of the light source permits a corresponding decrease in the feature size. Since the minimum feature size will be about 1.3 times the light source wavelength, the semiconductor industry has used light sources including mercury G-line, having a wavelength of 436 nm, mercury H-line (404 nm), mercury I-line (365 nm), and laser KrF (248 nm). Light sources wavelengths can be further reduced with the laser ArF (193 nm) and laser F_2 (157 nm) [ref. 1.4, ref. 1.5 and ref. 1.6].

Changing the lighting source wavelength produces other problems. It was found that the mask material must be changed from fused silica, which is the best for wavelengths greater than 157 nm because its low expansion coefficient, to another material because fused silica is opaque at wavelengths less than or equal to 157 nm [ref. 1.8]. In the current work, a comparison between the fused silica and calcium fluoride will be presented.

In order to achieve the minimum error required for the maximum pattern displacement for optical lithography technology, all manners of distortions will have to be identified, then eliminated or minimized. In the current work, distortion due to thermal loading during the exposure process is investigated in detail [ref. 1.7]. Figure 1.6 shows one distorted and another undistorted optical lithographic product.

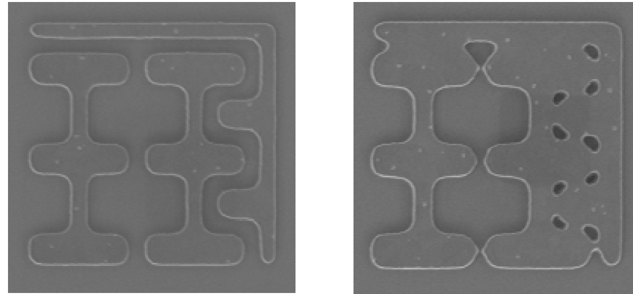

Figure 1.6. Undistorted and distorted optical lithography product [ref. 1.1]

1.5 References

[1.1] WWW.Photronic.com

[1.2] G. L.-T. Chiu and J. M. Shaw, Guest editors, "Optical Lithography: Introduction," IBM Journal of Research & Development, Vol. 41, no.1/2-Optical lithography, 1997.

[1.3] Semiconductor Industry Association, "National Technology Roadmap for Semiconductors," 1994.

[1.4] L. F. Thompson, C. G. Willson, and M. J. Bowden, "Introduction to Microlithography," ACS Professional Reference Book, 1994.

[1.5] R. Pätzel, "Excimer Lasers for Optical Lithography" Vacuum & Thin film, pp. 30-33, March 1999.

[1.6] U. Stamm, I. Bragin, S. Govorkov, J. Kleinschmidt, R. Pätzel, E. Slobodtchikov, K. Vogler, F. Voβ, D. Basting, "Eximer Laser for 157 nm Lithography," Proceedings of the 1999 SPIE symposium on Emerging Lithography Technologies III, Vol. 3676, pp. 816-826, 1999.

[1.7] J. Chang, A. Abdo, B. Kim, T. Bloomstein, R. Engelstad, E. Lovell, W. Beckman and J. Mitchell, "Thermomechanical Distortions of Advanced Optical Reticles during Exposure," Proceedings of the 1999 SPIE symposium on Emerging Lithography Technologies III, Vol. 3676, pp. 756-767, 1999.

[1.8] T. M. Bloomstein, M. W. Horn, M. Rothschield, R. R. Kunz, S. T. Palmacci, and R. B. Goodman, "Lithography with 157 nm lasers," J. Vac. Sci. Technology B 15 (6), pp. 2112-2116, Nov/Dec 1997, ©1997 American Vacuum Society.

Chapter Two
Optical lithography process

2.1 Introduction

The basic imaging idea is that a light from an illumination source passes through a photomask, which defines the images. The photomask consists of areas that are completely opaque and complementary areas that are transparent.

In industry, there are many methods of producing patterns with optical lithography using this basic idea. The earliest was called contact or proximity printing. Proximity printing (or shadow printing) exposes a wafer that was coated with a photosensitive polymer with ultraviolet light (wavelengths ranging from 150 nm to 450 nm) through a mask that is located close to the wafer. The mask contains clear and opaque features that define the circuit pattern. These image transfer techniques were the mainstay of device fabrication up to the mid-1970s. The fundamental resolution limitation of shadow printing is the diffraction (i.e., bending) of light at the edge of an opaque feature on the mask as the light passes through an adjacent clear area.

Figure 2.1 illustrates the typical light intensity distribution incident on the surface of a resist-coated wafer after the light has passed through a mask containing a periodic grating consisting of opaque and transparent lines or space of equal width b. Ideal image transfer would produce a pattern of light at the wafer surface whose intensity is shown by the

square waves depicted by the dotted line in Figure 2.1. The actual intensity pattern, shown by the solid line in Figure 2.1, deviates considerably from this square-wave pattern, especially as the feature size on the mask approaches dimensions comparable with the wavelength of the exposing radiation. The deviation from ideal image transfer results from diffraction, which causes the image of the mask edge at the wafer surface to be blurred and diffuse.

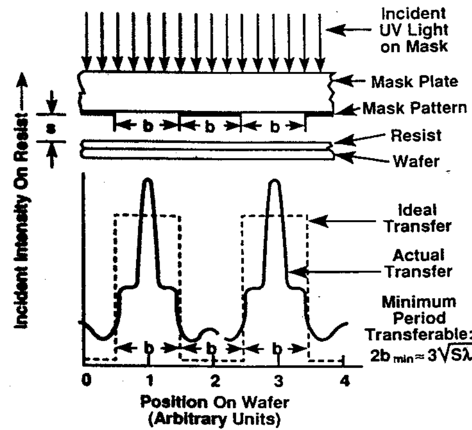

Figure 2.1. Intensity profiles for contact and proximity printing [ref. 2.1].

The theoretical resolution capability of shadow printing for a conventional photoresist and a mask consisting of equal lines and spacing of width b is given by

$$2b_{\min} = 3\sqrt{\lambda(s + (1/2)z)} \qquad (2.1)$$

where $2b$ is the grating period, s is the gap width maintained between the mask and the photoresist surface, λ is the wavelength of the exposing radiation, and z is the photoresist thickness [ref. 2.1].

From equation 2.1, for hard contact printing (i.e., with the gap *s* equal zero), the maximum resolution for 400 nm wavelength light in a 1 µm thick resist film will be slightly less than 1 µm. The resolution reduces as the gap distance *s* between the mask and wafer increases.

The difference between contact printing and proximity printing is the space between the mask and the wafer (i.e., the gap). For contact printing the space is zero, producing the best resolution; within diffraction limits, contact printing can transfer a mask pattern into a photoresist with almost 100% accuracy. The problem is the possible damage of both the mask and wafer in the process, as they are in direct surface contact. In proximity printing, there is a small gap between the mask and the wafer, which eliminates the possibility of damage, but results in less accuracy in the process. For any gap, the minimum transferable period is given by

$$2b_{\min} \approx 3\sqrt{s\lambda} \qquad (2.2)$$

For example, with all the other conditions the same as for contact printing at a gap of 10 µm, the maximum resolution will be about 3 µm: a minimum feature size three times larger than the case of contact printing.

The problems and limitations of contact and proximity printing led to the development of projection printing, in which the mask and the wafer are separated by many centimeters and lens elements are used to focus the mask image onto the wafer surface.

There are several different projection-printing strategies. In the current work, only two methods for the optical lithography process will be considered, namely full field exposure and step and scan exposure.

2.2 Full field exposure

The full field exposure process uses a mask containing the maximum number of chip patterns capable of being imagined in a single exposure. A series of exposures are used to expose all the needed field on the wafer. Figure 2.2 shows the schematic of the full field exposure process.

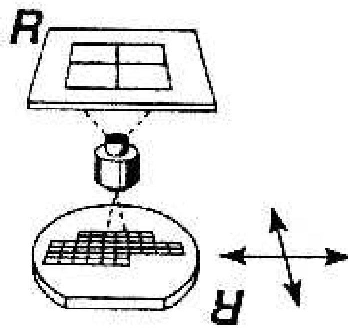

Figure 2.2. Schematic of the full field exposure process [ref. 2.1].

Reduction optics makes it possible for the size of a feature on the mask (also called the reticle) to be greater than the size of the corresponding image projected on the wafer. For example, imaging a 1.0 μm sized feature on a wafer with a 10:1 reduction lens would require a reticle with corresponding 10 μm sized feature. Because the maximum area of the object that can be imaged per single exposure is constant for a given lens system,

increasing the size of the reticle feature reduces the number of chips patterns that can be imaged per step, thereby increasing the time needed to completely expose the wafer. On the other hand, it is much easier to make a mask with 10 µm features than one with 1 µm features, which typically leads to an economic tradeoff having to be made between throughput, and ease and reliability of reticle manufacture. Figure 2.3 illustrates one field on the wafer produced by full field exposure with a mask by 5:1 reduction system.

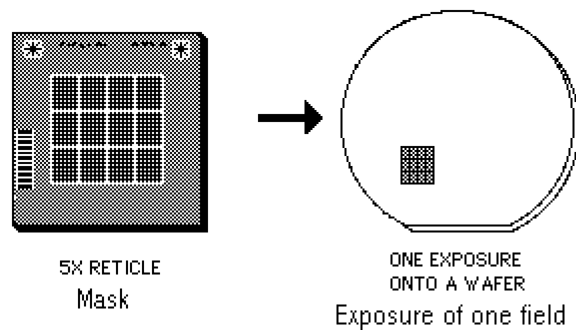

Figure 2.3. Mask and wafer after one exposure with 5:1 reduction system [ref. 2.2].

Figure 2.4 shows a complete wafer containing many fields; the magnified area is the size of one field. It also shows the relative dimension of one field (i.e., one mask pattern after reduction), relative to the final wafer size. It can be noticed from this figure the number of fields that the mask must step to complete one wafer.

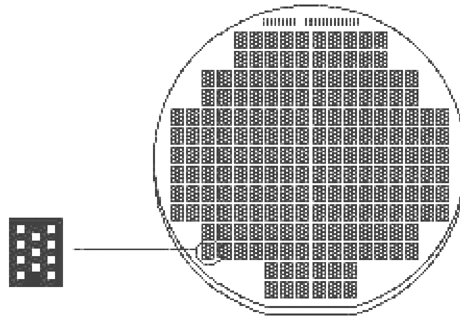

Figure 2.4. Dimension of one field relative
to the final wafer [ref. 2.2].

The mask content represents one single field on the wafer surface. During this process both the mask and the wafer, are stationary at the time of exposure. The wafer is stepped by means of a precise mechanical stepper after completing each field.

2.3 Step and scan exposure

One of the most successful exposure approaches is based on scanning projection, which was first introduced by Perkin-Elmer in 1973 [ref. 2.1 and ref. 2.3]. In this strategy, the mask pattern content is scanned forming the image for only one field on the wafer. This optical system is capable of transferring a large number of pixels (number of resolution elements) because only a small annular portion of the field is exposed. This annular strip is scanned transverse to the annulus, sweeping out the full area of the wafer. The process is repeated as the wafer is stepped to produce another field.

In the step and scan process both the mask and the wafer are moved simultaneously during exposure using a complex mechanical system. Figure 2.5 shows the schematic of the step and scan process.

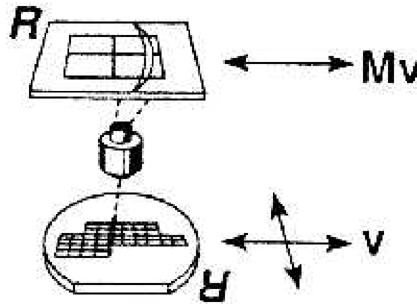

Figure 2.5. Schematic of the step and scan exposure process [ref. 2.3].

2.4 Sources of optical mask pattern displacement

All pattern generators create small errors in pattern placement and image quality. At the level of the smallest feature, there are many sources of pattern placement errors. When dealing with displacement in nanometers, even the gravitational forces of the mask itself is a source of pattern placement error. Every successful pattern generator relies on a strategy of prediction, measurement, and correction of pattern errors.

The current work is focused on the pattern placement errors due to thermal distortion of the mask during exposure. Figure 2.5 shows what a distorted shape looks like when compared with an undistorted mask pattern. These distortions are greatly enlarged as the actual distortions are in nanometers.

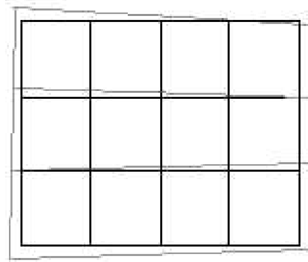

Figure 2.5. Schematic of the distorted and undistorted shapes of a mask [ref.2.2].

The exposure process is actually a heat deposition process: some of the applied heat will be absorbed within the mask and some will act as an applied heat flux due to absorption in the chrome layer on the mask (defining the electrical circuit).

This heat loading can lead to serious distortion of the mask. The current work is concerned with predicting the thermal distortion under varies exposure conditions. The commercial finite element package ANSYS® was used for thermal and structural simulations throughout the current work.

2.5 References

[2.1] L. F. Thompson, C. G. Willson, and M. J. Bowden, "Introduction to Microlithography," ACS Professional Reference Book, 1994.

[2.2] WWW.Photronic.com

[2.3] John H. Bruning, Tropel Corporation, Fairport, NY 14450, "Optical Lithography – Thirty Years and Three Order of Magnitude, The Evolution of Optical Lithography Tools," Proceedings of SPIE, Vol. 3048, pp. 14-27, 10-11 March 1997, Santa Clara, California.

[2.4] P. Rai-Choudhury, "Microlithography, Micromachining, and Microfabrication," SPIE Optical Engineering Press, 1997.

Chapter Three
Thermal response during exposure – Full Field Exposure

3.1 Introduction

In this chapter, the thermal response during full field exposure will be studied. The actual process was described in Section 2.2. In this chapter the numerical model that simulates the actual mask thermal process will be developed.

Figure 3.1 shows the physical imaging process. The mask is a piece of glass (usually fused silica) covered with the chrome pattern. The light, passing through the clear portions of the chrome side of the mask reacts with the photoresist, producing the desired image of the electrical circuit on the wafer surface.

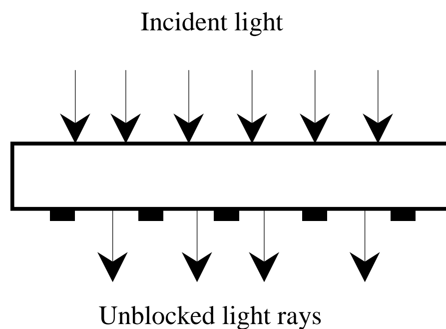

Figure 3.1. Imaging process.

As the mask produces many fields on a single wafer, the light is flashed “on” and “off”. During the “off” period the wafer is stepped to the next field. The mask remains stationary. Light is “on” during the imaging of a field, then the light is “off” during

wafer movement (stepping) to the following position to produce another field and so on till the wafer is completed. Figure 3.2 shows one possible duty cycle on the mask, the flash delay is the time delay after each exposure, where the light is “off”, and the wafer delay is the wait time needed to change the wafers.

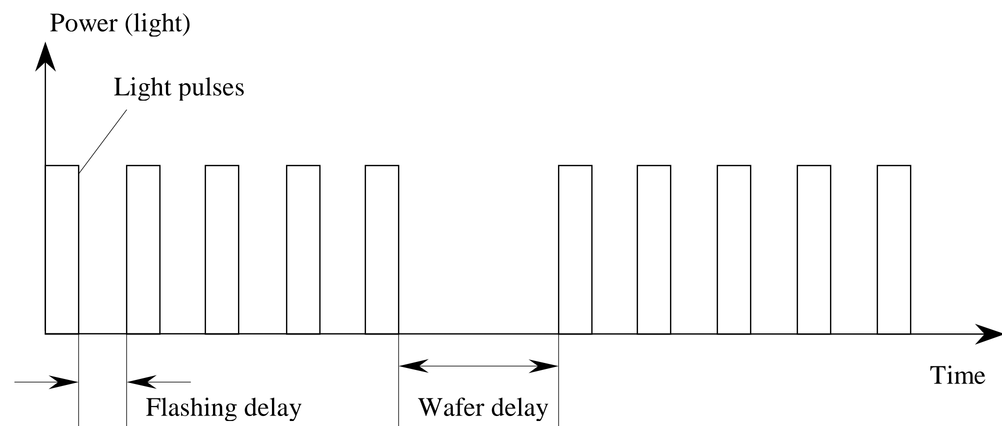

Figure 3.2. Heat applied profile (mask duty cycle).

Now looking on the thermal loading on the mask. The flashing incident light will produce two main thermal loads on the mask. The first is the portion of incident light absorbed in the mask thickness and depends on the mask material absorptivity. And the second is the portion of energy absorbed by the covered portion of the chrome layer. The chrome will absorb part of the incident energy, depending upon the chrome absorptance. Some of the reflected energy will be absorbed in the mask. The energy absorbed in the very thin chrome layer acts like an applied heat flux to the bottom (chrome) layer.

Figure 3.3 shows a cross section of the mask illustrating the thermal loading mechanisms. The shaded area is the portion of the mask where heat is absorbed, the upper arrows

represent the incident light and the lower upward facing arrows represent the heat flux applied at the chrome layer.

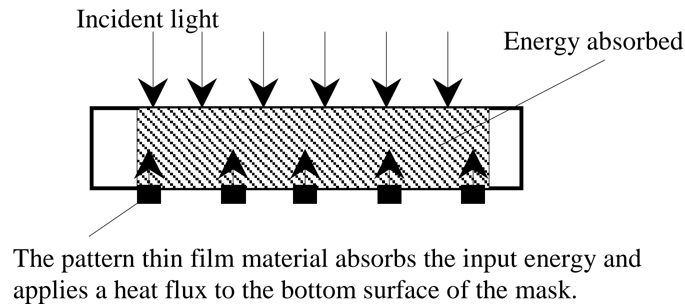

Figure 3.3. Thermal loading mechanism.

Figure 3.4 shows the heat loss mechanism from the mask. Heat will be lost from the system by natural convection, as the mask is stationary in a still air, by radiation to the surrounding and by heat conduction to the mounting system.

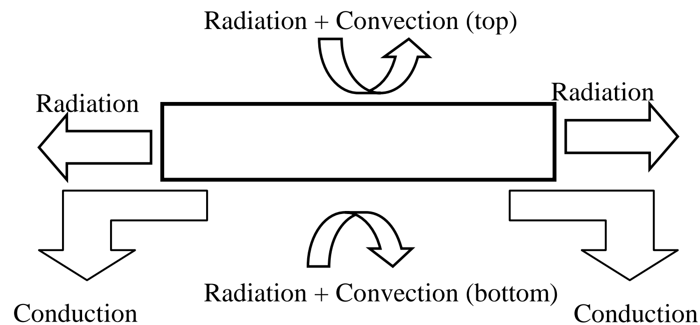

Figure 3.4. Heat loss mechanism.

To produce better image from this optical lithography process, a pellicle (which is a plastic transparent screen) is placed on the bottom surface of the mask just bellow the pattern side separated from the chrome pattern by few millimeters. The purpose of this pellicle is to make all the dust falling on the patterned side to be out of focus so that it

will not be printed on the wafer during the imaging process. Figure 3.5 shows the complete mask outline, including the pellicle, the mount and the pattern.

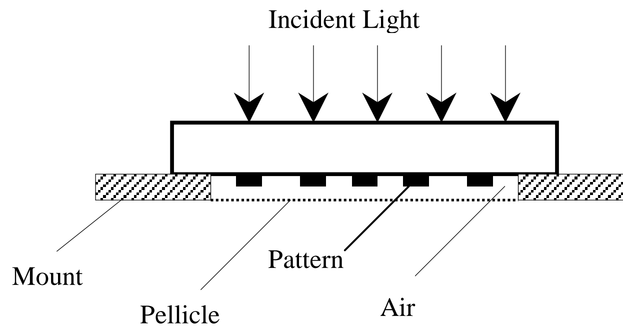

Figure 3.5. Mask outline.

The pellicle will have an important impact on the heat transfer process, as it contains still air trapped in the gap between the pellicle and the bottom side of the wafer. Consequently there is a difference between the heat transfer on the top surface and the bottom surface of the mask, as the heat transfer coefficient and emissivities are different.

3.2 Steady state analysis

As a first step in obtaining the thermal distortion for the actual exposure process, several numerical tests performed before simulating the actual case. As a start, steady state problems will be used first, then transient problems will be used for benchmarking ANSYS® [ref. 3.1] modeling.

3.2.1 Test case

For testing the commercial program package ANSYS® to be sure that we understand how it works and that it is used correctly, all the heat transfer characteristics must be tested with many simple test cases. Some simple problems will be solved with ANSYS® and the solution will be compared with their corresponding analytical solutions.

3.2.1.1 Circular plates

3.2.1.1a- Circular glass with applied heat generation, radiation loss and fixed edge temperature.

As a start, let us use an axisymetric problem in order to get its complete analytical solution. Assuming a circular glass with radius r_{out} with internal heat generation q_{gen}, from the center to radius r_{gen}, and with only radiation heat loss from top and bottom with emissivity ε. A fixed edge temperature T_{edge} will be assumed. To exclude the multidimensional conduction from this problem, infinite conductivity through the thickness of the glass δ will be assumed, the temperature is then function of radius r only. The governing equation for the heated zone (i.e., first zone) ranging from $r \geq 0$ to $r \leq r_{gen}$ is [ref. 3.2],

$$\frac{1}{r}\frac{d}{dr}(kr\frac{d\theta}{dr}) + q_{gen} - \frac{h\theta}{\delta} = 0 \tag{3.1}$$

where, θ is defined as

$$\theta(r) = T(r) - T_{\infty} \tag{3.2}$$

where T_∞ is the ambient temperature and *T(r)* is the temperature at any radius *r* (for this equation *r* will be ranging from zero to r_{gen}, *h* is the sum of the convection heat transfer coefficient and the linearized radiation coefficient,

$$h = 4\varepsilon\sigma T_{avg}^3 \tag{3.3}$$

Where, ε is the emissivity, σ is Stephan-Boltzman constant (5.67e-8 W/m^2-K^4) and T_{avg} is the average temperature between the maximum temperature and the ambient temperature, and could be calculated from

$$4T_{avg}^3 = (T_{max} + T_\infty)(T_{max}^2 + T_\infty^2) \tag{3.4}$$

$$\varepsilon\sigma(T_1^4 - T_2^4) = \varepsilon\sigma(T_1 - T_2)(T_1 + T_2)(T_1^2 + T_2^2) = 4\varepsilon\sigma T_{avg}^3(T_1 - T_2) \tag{3.5}$$

This linearized radiation coefficient works best if the two temperatures are closer to each other. In order to solve equation 3.1, another variable φ is defined as

$$\varphi = q_{gen} - \frac{h\theta}{\delta} \tag{3.6}$$

$$\frac{d\varphi}{dr} = -\frac{h}{\delta}\frac{d\theta}{dr} \tag{3.7}$$

Substituting with equation 3.6 and 3.7 into equation 3.1 leads to equation 3.8:

$$\frac{1}{r}\frac{d}{dr}(kr\frac{d\varphi}{dr}) - \frac{h\varphi}{\delta} = 0 \tag{3.8}$$

The general solution is given by Bessel function as follows.

$$\varphi(r) = C_1 I_o(mr) + C_2 K_o(mr) \tag{3.9}$$

Which can be differentiated to yield

$$\frac{d\varphi}{dr} = m[C_1 I_1(mr) - C_2 K_1(mr)] \tag{3.10}$$

where, I_o, K_o are Bessel functions of the first and second kind, C_1, C_2 are the integration constant and m is defined as,

$$m^2 = \frac{h}{k\delta} \tag{3.11}$$

At r equal to zero, the temperature must be finite, substituting into equation 3.9, it can be concluded that

$$\varphi(0) = C_1 I_0(0) - C_2 K_0(0) \tag{3.12}$$

As $K_0(0)$ is infinity C_2 must be zero. Combining equations 3.6 and 3.8 we obtain:

$$q_{gen} - \frac{h\theta}{\delta} = C_1 I_o(mr) \tag{3.13}$$

From which $T(r)$ is:

$$T(r) = T_\infty + [q_{gen} - C_1 I_o(mr)]\frac{\delta}{h} \tag{3.14}$$

Equation 3.14 is the temperature distribution in the first zone where the heat generation is applied (i.e., $r \geq 0$ to $r \leq r_{gen}$). For the second zone (i.e., $r \geq r_{gen}$ to $r \leq r_{out}$), the governing equation is modified as no heat generation is applied in this region. The governing equation is then:

$$\frac{1}{r}\frac{d}{dr}(kr\frac{d\theta_{out}}{dr}) - \frac{h\theta_{out}}{\delta} = 0 \tag{3.15}$$

where θ_{out} has the same difinition given from equation 3.2 but with r is ranging from r_{gen} to r_{out}. The general solution is given by Bessel function as

$$\theta_{out}(r) = C_3 I_o(mr) + C_4 K_o(mr) \tag{3.16}$$

Similarly, I_o and K_o are Bessel functions of the first and second kind, C_3, C_4 are the integration constant and m is defined by equation 3.11. After determining that C_2 must be zero, there are now only three constants C_1, C_3 and C_4. These constants need three boundary conditions, starting from the second zone, then,

1- At, $r = r_{out}$ the temperature is fixed to be T_{edge} or

$$\theta_{out}(r_{out}) = C_3 I_o(mr_{out}) + C_4 K_o(mr_{out}) \tag{3.17}$$

or by using equation 3.2, we get

$$T_{edge} - T_{\infty} = C_3 I_o(mr_{out}) + C_4 K_o(mr_{out}) \tag{3.18}$$

2- At the interface between the two zones, the heat conducted from one zone is equal to the heat conducted to the other zone. In other words the temperature gradiant must be the same. The temperature gradient in the first zone is calculated from equation 3.13 and 3.2 as:

$$\frac{dT}{dr} = \frac{d\theta}{dr} = -\frac{\delta}{h} m[C_1 I_1(mr_{gen})] \tag{3.19}$$

The temperature gradient in the second zone is calculated from equations 3.2 and 3.16 as:

$$\frac{dT_{out}}{dr} = \frac{d\theta_{out}}{dr} = m[C_3 I_1(mr_{gen}) - C_4 K_1(mr_{gen})] \tag{3.20}$$

Since $\frac{dT_{out}}{dr} = \frac{dT}{dr}$ at the interface then equation 3.19 must be equal to equation 3.20 or

$$-\frac{\delta}{h}[C_1 I_1(mr_{gen})] = [C_3 I_1(mr_{gen}) - C_4 K_1(mr_{gen})] \tag{3.21}$$

3- At the interface between the two zones (at $r = r_{gen}$), the temperatures must be equal, i.e., $T(r_{gen}) = T_{out}(r_{gen})$. The temperature from the first zone is calculated from equation 3.14 or,

$$T(r_{gen}) = T_{\infty} + [q_{gen} - C_1 I_o(mr_{gen})]\frac{\delta}{h} \tag{3.22}$$

While the temperature from the second zone is calculated from equation 3.16 as:

$$T_{out}(r = r_{gen}) = T_{\inf inity} + C_3 I_o(mr_{gen}) + C_4 K_o(mr_{gen}) \tag{3.23}$$

As $T(r = r_{gen}) = T_{out}(r = r_{gen})$ then both right hand sides of equations 3.22 and 3.23 are,

$$[q_{gen} - C_1 I_o(mr_{gen})]\frac{\delta}{h} = C_3 I_o(mr_{gen}) + C_4 K_o(mr_{gen}) \tag{3.24}$$

Table 3.1. Input parameters for the test cases.

Dimensions	Circular plate outer radius r_{out}	10 cm
	Exposure radius r_{gen}	5 cm
	Circular plate thickness δ	0.635 cm
Applied load	Lighting power q_{light}	5 W/cm^2
Pattern characteristics	Glass absorption coefficient	0.4% 1/cm
	Chrome absorptivity	90%
	Chrome coverage	50%
Heat transfer characteristics	Ambient temperature T_{∞}	300 K
	Emissivity ε	0.9
	Edge temperature T_{edge}	301 K
Material properties (Fused Silica)	Thermal conductivity k	0.0138 W/cm-K
	Density ρ	2202 E-6 g/cm^3
	Specific heat C	746 J/kg-K

Using equations 3.18, 3.21 and 3.24 we can solve for the three unknowns C_1, C_3, and C_4. An EES® program [ref. 3.3] was used to solve these equations and obtain the temperature

distribution. The temperature distribution was also calculated using ANSYS®. Both the analytical and ANSYS® solutions match each other very well, as will be shown later in this chapter. Table 3.1 is a list of the input parameters used in the comparison.

For the thermal loading calculations, two heating effects take place as described earlier in this chapter. The portion of light energy absorbed as it passes through the glass q_{gen} (W/cm^2), is calculated from:

$$q_{gen} = q_{light} * \alpha_{glass} + q_{light} * (Covg\% / 100) * (1 - \alpha_{chrome}) * \alpha_{glass} * \tau_{glass} \quad (3.25)$$

where, q_{light} is the heat from the light source (W/cm^2), α_{glass} is the absorption of the glass calculated from the glass transmissivity τ_{glass} and by neglecting the glass reflectivity as:

$$\alpha_{glass} = 1 - \tau_{glass} \quad (3.26)$$

The glass transmissivity τ_{glass} is calculated from the glass absorption coefficient κ (1/cm) as,

$$\tau_{glass} = e^{-2.3 * \kappa * \delta} \quad (3.27)$$

where, δ is the glass thickness (cm). The parameter *Cov%* is the percentage Chrome coverage over the bottom surface of the mask, while α_{chome} is the Chrome absorptivity. The first term for equation 3.25 account for the rays of light passing for the first time while the second term accounts for the reflected rays from the chrome covarege. Any rays reflected again are neglected as they will be very small relative to the incident and the reflected ones. The heat flux resulting from absorption in the chrome coating on the bottom surface of the mask q_{flux} (W/cm^2) can be calculated from

$$q_{flux} = q_{light} * (Covg\% / 100) * \alpha_{chrome} * \tau_{glass} \tag{3.28}$$

The applied heat flux is proportional to the heat from the light source q_{light} (W/cm^2) and the chrome coverage percentage *Cov%* and the chrome absorptivity α_{chome}. The amount of heat reaching the chrome surface is less than the amount input from the light source by a factor which is the glass transmissivity. This is due to the exponential profile of heat absorption in the glass thickness. Figure 3.6 shows the schematic of the heat loading on the mask described by equations 3.25 and 3.28 and Figure 3.7 shows the schematic of the axisymetric problem for the first test case.

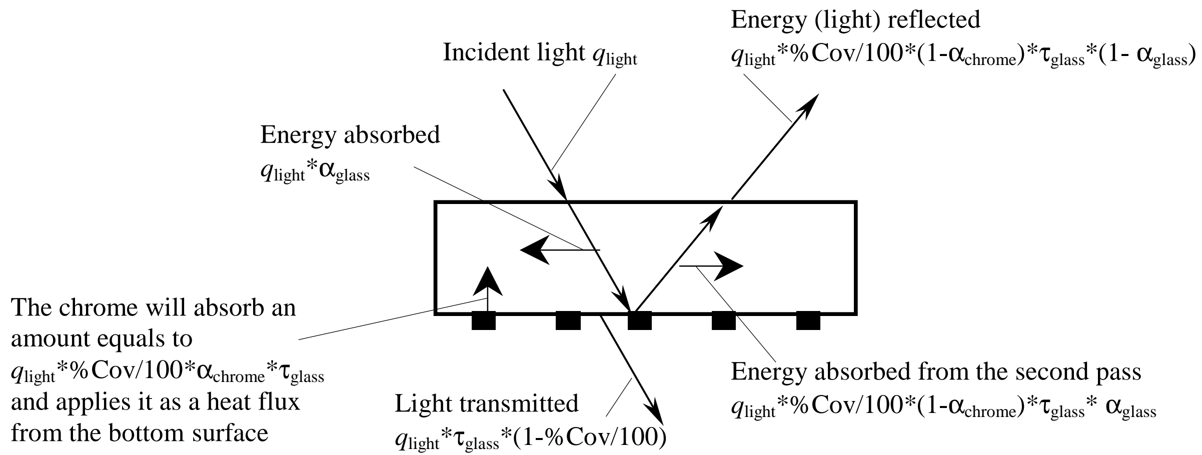

Figure 3.6. Schematic of the heat loading mechanism.

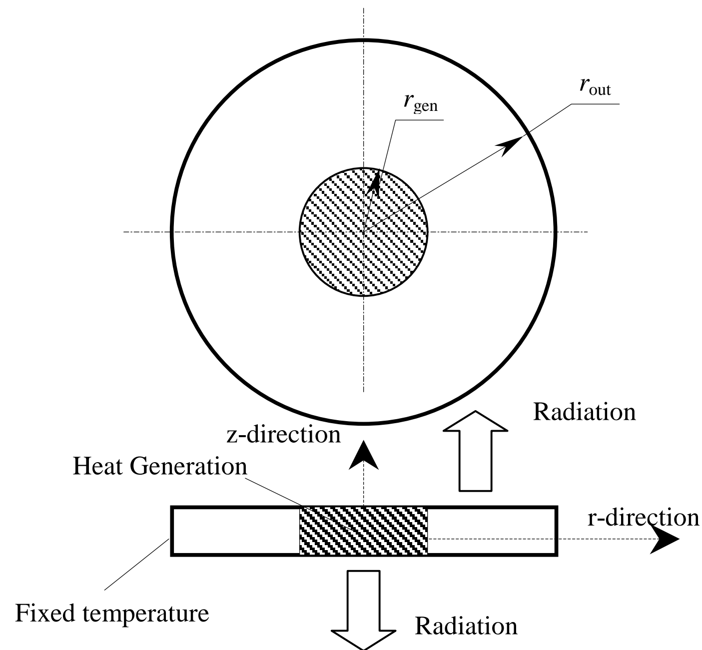

Figure 3.7. Axisymetric heat generation and radiation loss.

Figure 3.8 shows ANSYS® result using the parameters in Table 3.1, for the shell element (shell 57), while Figure 3.9 shows the result for a three-dimensional solid element (solid 70).

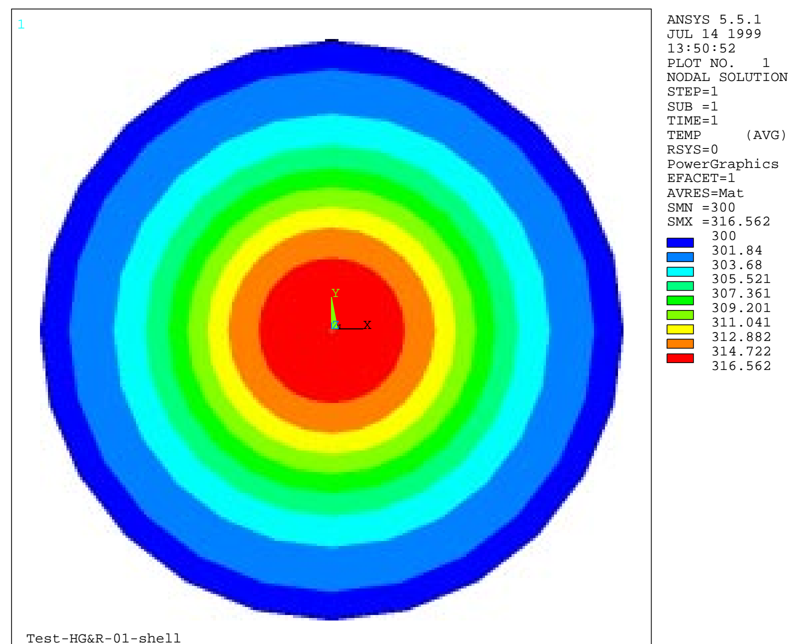

Figure 3.8. ANSYS® result for the shell element.

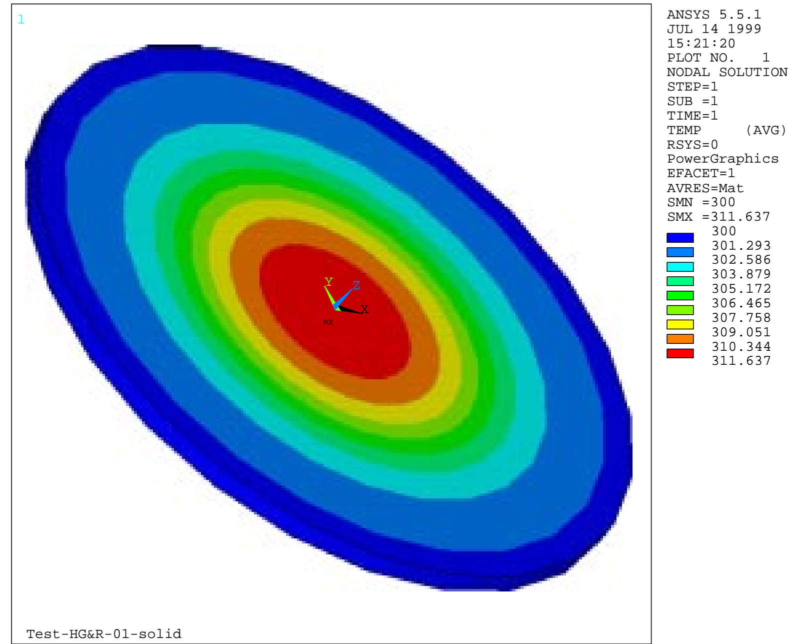

Figure 3.9 ANSYS® result for the solid element.

Figure 3.10 shows the comparison between the analytical solution and ANSYS® solution for two types of ANSYS® elements, shell element (shell 57) which is a thermal two-dimensional elements, and solid element (solid 70) which is a thermal three-dimensional element using the parameters in Table 3.1. Both figures show that the results agree very well.

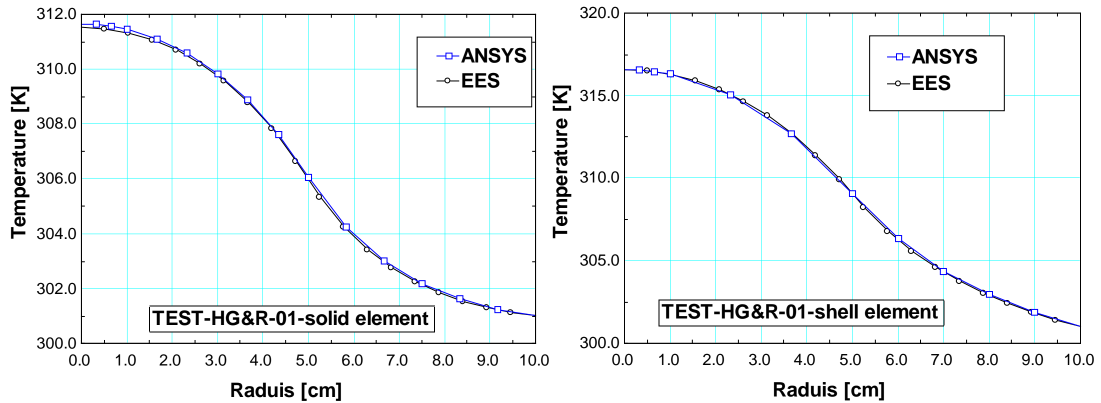

Figure 3.10. Comparison between both solutions for shell and solid elements.

The difference between the shell element and the solid element is that the first is a two dimensional element so the radiation is considered from only one side of the element while the other is a three-dimensional element and the radiation is considered from both sides of it.

3.2.1.1b- Circular glass with applied heat generation, radiation, convection losses and fixed edge temperature.

In order to check the convection heat loss, a test similar to the previous one was done to understand and check ANSYS® solution for radiation and convection problems independently. Figure 3.11 shows the schematic of the axisymetric problem.

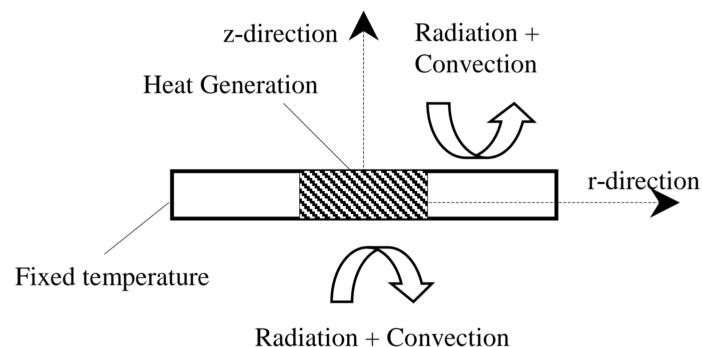

Figure 3.11. Axisymetric heat generation with radiation and convection losses.

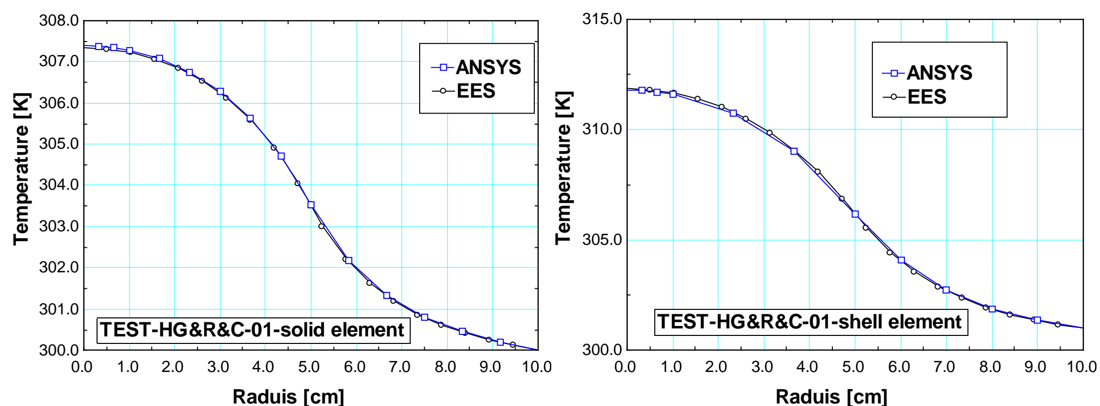

Figure 3.12. Comparison between both solutions for shell and solid elements.

Figure 3.12 shows the comparison between the analytical solution and ANSYS® solution using the parameters in Table 3.1, for both ANSYS®'s types elements.

3.2.1.1c- Circular glass with applied heat flux, radiation, convection losses and fixed edge temperature.

After testing problems with internal heat generation, ANSYS®'s ability to solve problems with surface heat flux were also tested. A heat flux is applied over the same circular plate with convection and radiation from both the top and the bottom surfaces. The heat flux was applied over a portion of the top of a circular plate. The edges had a fixed edge temperature. Figure 3.13 shows the schematic of the problem.

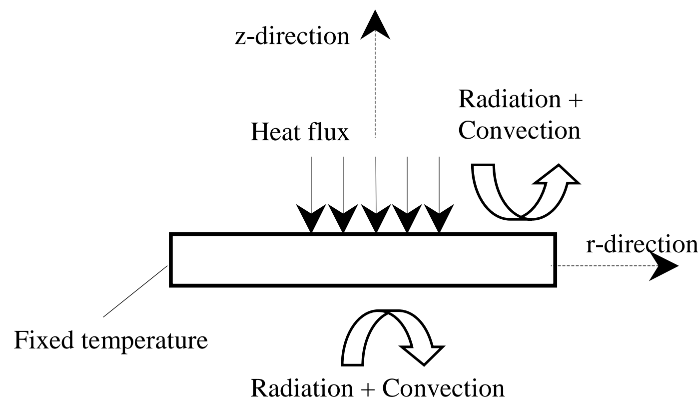

Figure 3.13. Axisymetric problem with surface heat flux, convection and radiation.

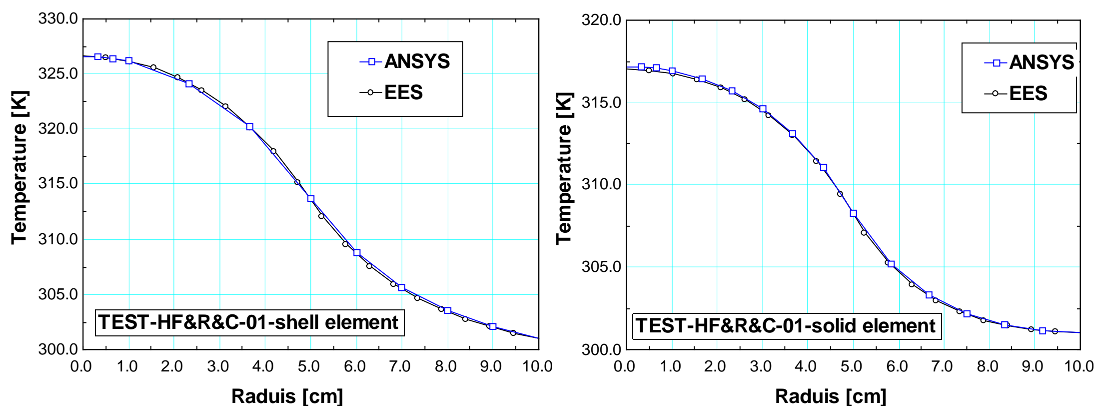

Figure 3.14. Comparison between both solutions for shell and solid elements.

Figure 3.14 shows the comparison between both solutions using the parameters in Table 3.1.

3.2.1.2-Square plate

3.2.1.2a-Heat generation loading with radiation heat loss.

The actual geometry of the optical mask is a square glass plate (or rectangular). The set of tests with the circular shape plates was used because the analytical solution was easy to obtain. The actual geometry must be tested before building a final model. In this problems a lumped system will be assumed, to simplify the problem by excluding any conduction problem. The analytical solution is only a heat balance to compare the steady state temperature analytically with ANSYS® solution. Figure 3.15 shows a schematic of the problem.

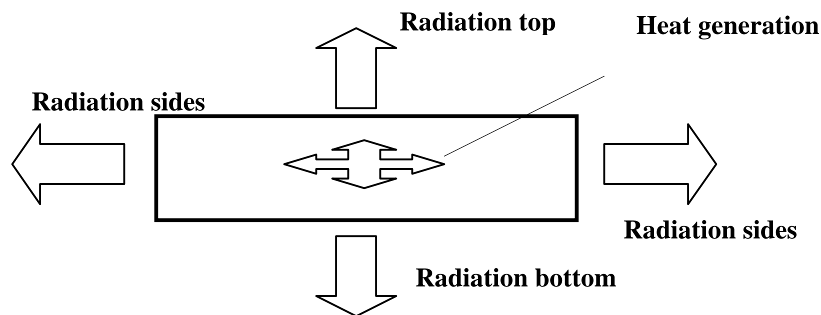

Figure 3.15. Heat generation with radiation for a square mask.

Table 3.2. Input parameters for the square mask test cases.

Dimensions	Outer sides length	10 cm
	Exposure sides length	8 cm
	Mask thickness δ	0.635 cm
Applied load	Lighting power q_{light}	0.1 W/cm^2
Pattern characteristics	Glass absorption coefficient	0.4% 1/cm
	Chrome absorptivity	50%
	Chrome coverage	90%
Heat transfer characteristics	Ambient temperature $T_{infinity}$	300 K
	Emissivity ε	0.9
	Heat transfer coefficient	5e-4 W/ cm^2-K
Material properties (Fused Silica)	Thermal conductivity k	0.0138 W/cm-K
	Density ρ	2202 E-6 g/cm^3
	Specific heat C	746 J/kg-K

The analytical solution is based on the following energy balance equation:

$$q_{gen} A_{exposure} \delta = \varepsilon \sigma A_{radiation} (T^4 - T_{infinity}^4) \tag{3.29}$$

where, q_{gen} is the heat generated in the mask thickness calculated by equation 3.25, $A_{exposure}$ is the area exposed by the incident light. δ is the mask thickness, ε is the emissivity, σ is the Stefan Boltzman constant, $A_{radiation}$ is the radiation area, $T_{infinity}$ is the ambient temperature and T is the mask temperature at steady state. The input parameters are given in Table 3.2, where a blank square mask was assumed (i.e., a piece of glass without the chrome pattern) with internal heat generation in the entire volume (as a thermal loading). Also, radiation heat loss occurs from the entire free surface with different emissivities on the top, bottom and sides. The ANSYS® steady state temperature for this case is 300.313 K, while the analytical solution gives 300.312 K. The solutions are very close, the difference result from the large, but finite, thermal conductivity assumed in ANSYS®.

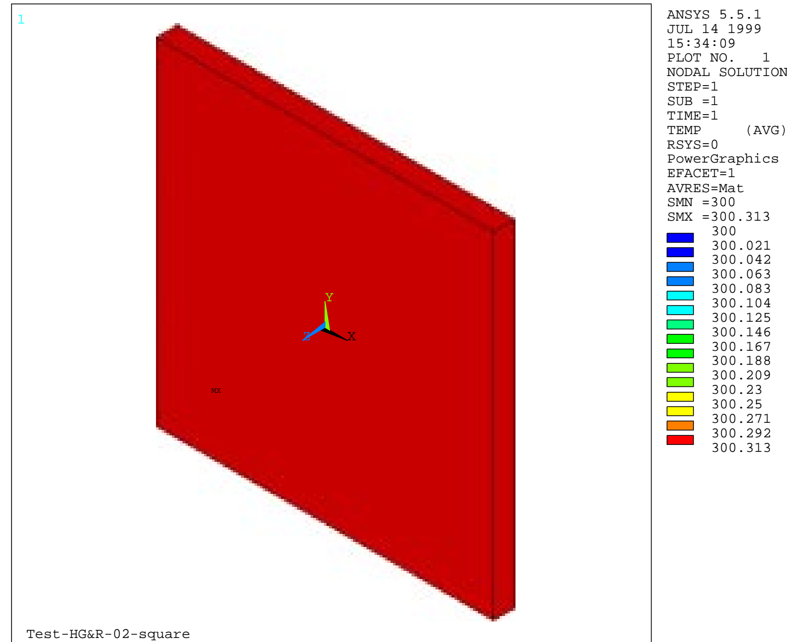

Figure 3.17 ANSYS® steady state results for the square mask.

Figure 3.17 shows ANSYS® steady state results for the square mask using three-dimensional thermal solid element (solid70) using the parameters in Table 3.2.

3.2.1.2b- Heat generation loading with radiation and convection heat losses.

The previous tests are combined together, by assuming internal heat generation inside the square glass mask is uniform and the convection and radiation heat loss from the top and bottom. Figure 3.18 shows the schematic of the problem.

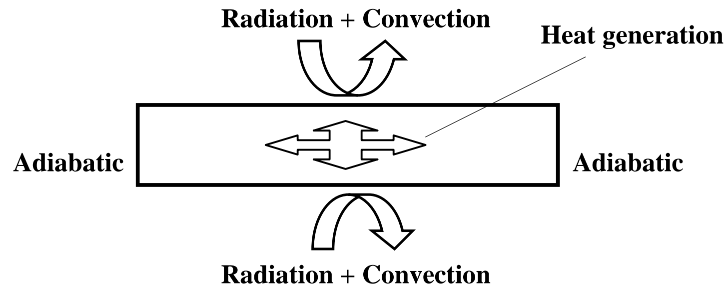

Figure 3.18. Heat generation with convection and radiation for a square mask.

The analytical solution of the problem is again just an energy balance to get the steady state temperature using the parameters in Table 3.2. The equation used for the analytical solution is an energy balance as follows:

$$q_{gen} A_{\exp osure} \delta = \varepsilon \sigma A_{radiation} (T^4 - T_{\inf inity}^4) + h A_{convection} (T - T_{\inf inity}) \tag{3.30}$$

The equation is similar to equation 3.29 where h is the convective heat transfer coefficient and $A_{\text{convection}}$ is the convection area. Both ANSYS® and EES® steady state temperature are 300.173 K.

3.2.1.2c- Heat flux with convection heat loss.

This test case is to check the modeling of both convection heat loss and the heat flux loading on a square mask. A patterned square mask will be used with a uniform heat flux (as a thermal loading) applied on the entire bottom surface. The analytical solution can be obtained from equation 3.28. Heat loss mechanism is convection from the top and bottom surfaces, with different heat transfer coefficient. The four side edges are assumed to be adiabatic. The analytical solution is based on the following equation:

$$q_{flux} A_{\exp osure} = h A_{convection} (T - T_{\inf inity})$$

Figure 3.19 shows the square mask problem, the arrow on the bottom surface represent the heat flux, convection will be considered from the top and bottom surfaces while the edges will be adiabatic.

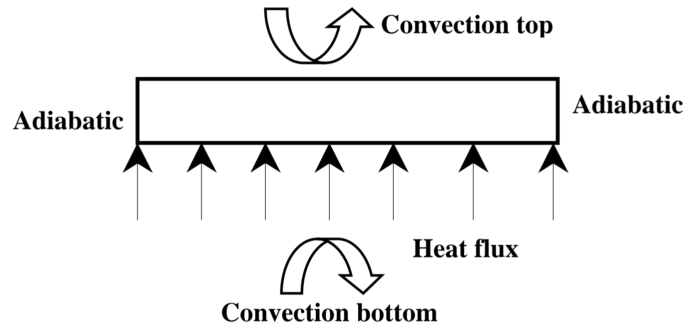

Figure 3.19. Heat flux with convection for a square mask.

The analytical steady state solution and ANSYS® solution both give the same temperature of 345.00 K.

Conclusion of test cases

The results of the test cases demonstrates that ANSYS® solutions match very well the analytical solutions, hence, it can be concluded that we know how ANSYS® works and how to use it and that can be used for the modeling of more difficult problems which have no analytical solutions.

3.2.2 Blank mask

The first case to be investigated that does not have an analytical solution is a three dimensional temperature profile. A blank mask (a piece of glass without any pattern) is modeled to find the steady state response during exposure to a light with convection form

top and bottom surfaces and with radiation heat loss from all its free surfaces. Figure 3.20 shows the schematic of the blank mask problem showing the exposure area.

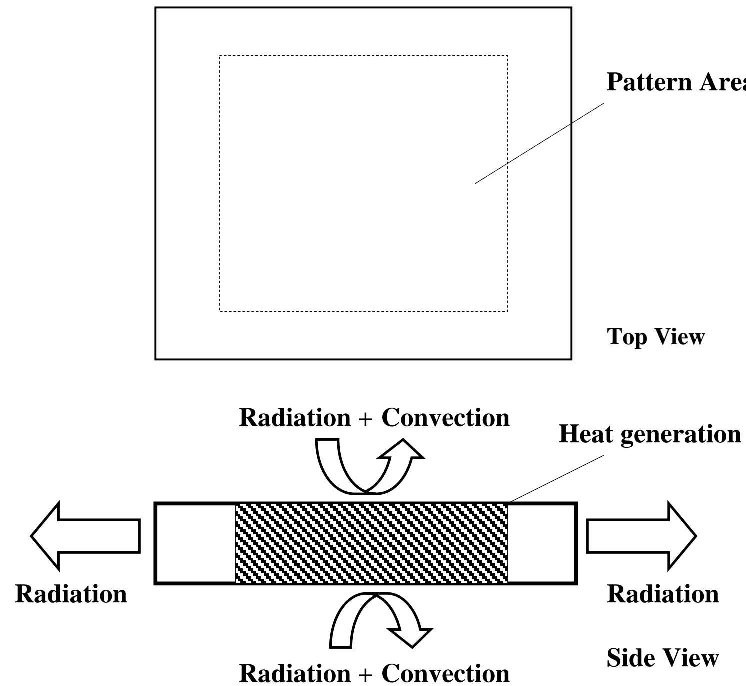

Figure 3.20. Schematic of the blank mask problem.

The thermal loading in this case results from the energy absorbed inside the glass thickness due to the glass absorptivity, and which can be calculated from equation 3.24. The energy absorbed is simulated with uniform heat generation in the exposed area. This case will be different than the fourth test case (section 3.2.1 case number four), since the conduction is finite resulting in a three-dimensional temperature profile. ANSYS® results for this problem are shown in Figure 3.21. The input parameters of the problems are listed in Table 3.3. Although it is not possible to compare the results with an analytical solution, the results appear reasonable.

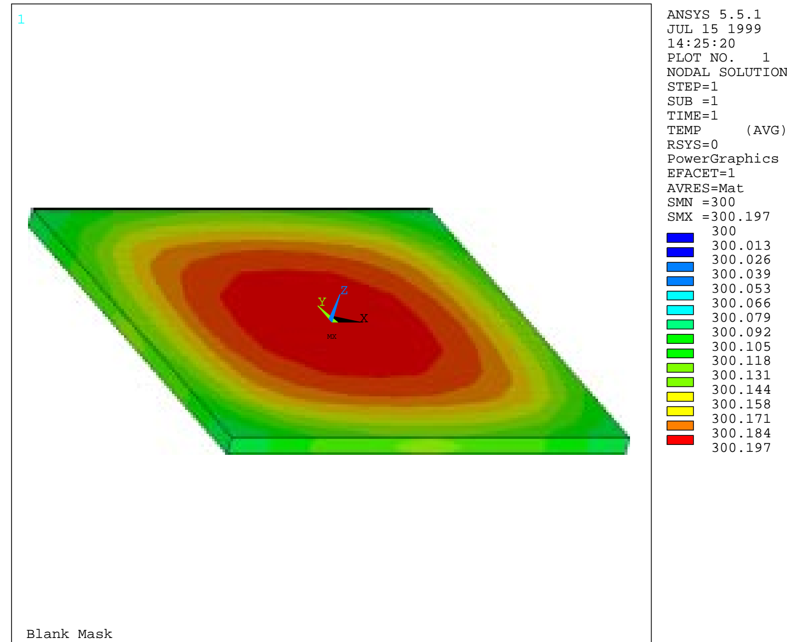

Figure 3.21 ANSYS® steady state results for the blank square mask.

Table 3.3. Input parameters for the blank square mask problem.

Dimensions	Outer sides length	15.24 cm
	Exposure sides length	13.2 cm
	Mask thickness δ	0.635 cm
Applied load	Lighting power	0.1 W/cm^2
Pattern characteristics	Glass absorption coefficient	0.4% 1/cm
	Chrome absorptivity	0%
	Chrome coverage	0%
Heat transfer characteristics	Ambient temperature T_∞	300 K
	Emissivity ε	0.9
	Top heat transfer coefficient	5e-4 W/ cm^2-K
	Bottom heat transfer coefficient	2.5e-4 W/ cm^2-K
Material properties (Fused Silica)	Thermal conductivity k	0.0138 W/cm-K
	Density ρ	2202 E-6 g/cm^3
	Specific heat C	746 J/kg-K

3.2.3 Mask with pattern

When the chrome pattern on the bottom surface of the mask is included, its effect must be included in the model. The thin chrome layer will absorb a portion of the energy incident on it in proportion to the chrome absorptivity. The effect is a heat flux applied to the bottom of the mask as shown in Figures 3.22. In Figure 3.22, the shaded area in the mask thickness represents the area with internal heat generation while the arrows from the bottom surface represents the surface heat flux applied from the chrome pattern. Using equation 3.28, the amount of heat flux applied on the bottom surface of the mask can be calculated assuming uniform chrome coverage.

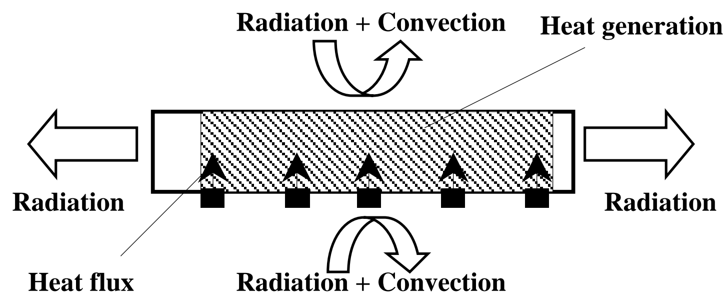

Figure 3.22. Mask with pattern.

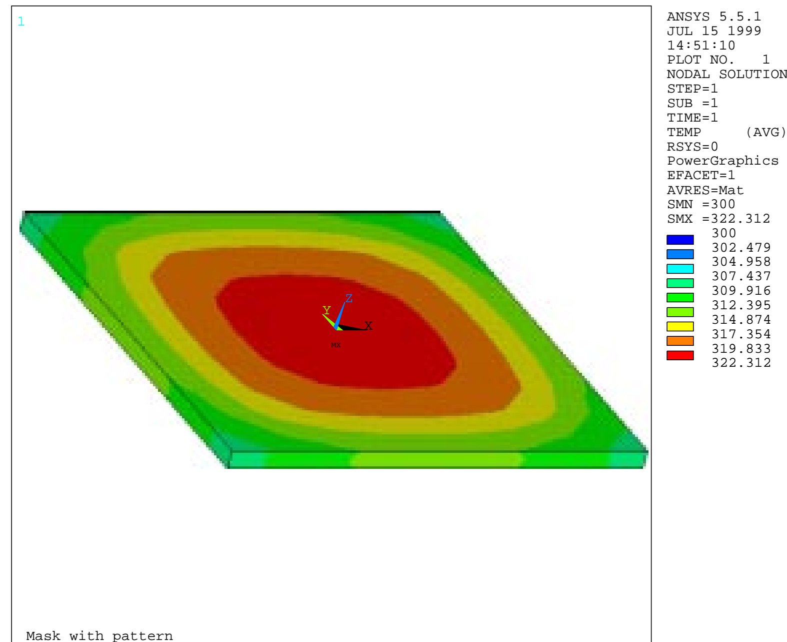

Figure 3.23 ANSYS® steady state results for mask with pattern.

Figure 3.23 shows the result of a mask with 50% coverage and 90% chrome absorptivity, all the other parameters are exactly the same given in Table 3.2. Again the results appear reasonable. The chrome layer increases the maximum mask temperature by more than 22 K.

3.3 Transient analysis

The actual process consists of illuminating the mask for a short period of time sufficient to print one field on the wafer, and then shutting the light off to allow the wafer to step to another position to print the following field. This process continues until the entire wafer is exposed. A new wafer then must be brought into position. During this period, the light

will be shut down a longer amount of time. The time delay between flashes will be called "flashing delay" and the time delay between wafers will be called "wafer delay".

3.3.1 Test cases

As was done for the steady state test cases, before starting to build the transient model, some test cases will studied. Four tests will be done on a square masks. Two with heat generation, the first with radiation on one side and the other with radiation from both sides, both assuming a lumped system. The third test adds heat flux on the bottom and has both convection and radiation for lumped system. The last case combines both heat flux and heat generation with convection, radiation and one-dimensional conduction.

3.3.1a- Transient response of a lumped system with internal heat generation and radiation loss from only one side.

A transient three-dimensional lumped square system, with internal heat generation and with radiation loss from only one of its surfaces, is the first test case to be used. The analytical solution can be obtained for this case. Starting from the energy balance on the square mask, the amount of energy generated per unit volume q_{gen} (calculated with equation 3.24) is multiplied by the mask volume $\forall$, to obtain the input heat into the mask. The energy loss is by radiation, which is the emissivity ε times Stefan-Boltzman constant σ times the area of one surface A times the difference between the element temperature T and the ambient temperature T_∞ to the fourth power. An energy balance on the mask relates the net energy input to the differential energy rise with the time:

$$q_{gen}\forall - \varepsilon\sigma A(T^4 - T_{i\infty}^4) = \rho\forall C\frac{dT}{d\tau} \qquad (3.31)$$

Here ρ is the density, C is the specific heat and τ is the time. Equation 3.31 can be re-written on the form,

$$\frac{d\tau}{\rho\forall C}=\frac{dT}{q_{gen}-\varepsilon\sigma A(T^4-T^4_{\inf inity})} \tag{3.32}$$

Or on the form

$$\frac{d\tau}{\rho\forall C}=\frac{dT/\varepsilon\sigma A}{(T^4_{\inf inity}+q_{gen}/\varepsilon\sigma A)-T^4} \tag{3.33}$$

Integrating equation 3.33 yields a long expression for the temperature with the time as,

$$2*(T^4_{\inf inity}+q_{gen}/\varepsilon\sigma A)^3*(\frac{\varepsilon\sigma A}{\rho\forall C})*\tau=\tan^{-1}[\frac{T_{final}}{(T^4_{\inf inity}+q_{gen}/\varepsilon\sigma A)}]-\tan^{-1}[\frac{T_{initial}}{(T^4_{\inf inity}+q_{gen}/\varepsilon\sigma A)}]$$
$$+\frac{1}{2}\{\ln[\frac{(T^4_{\inf inity}+q_{gen}/\varepsilon\sigma A)+T_{final}}{(T^4_{\inf inity}+q_{gen}/\varepsilon\sigma A)-T_{final}}]-\ln[\frac{(T^4_{iinitial}+q_{gen}/\varepsilon\sigma A)+T_{final}}{(T^4_{iinitial}+q_{gen}/\varepsilon\sigma A)-T_{final}}]\} \tag{3.34}$$

Numerical evaluation of equation 3.34 can be obtained using EES®. The analytical solution matches exactly ANSYS® results, as shown in Figures 3.24 and 3.25 in which one can see that for the both cases the temperature rise is 0.103 K in 300 seconds. All the input parameters used for this problem are given in Table 3.3.

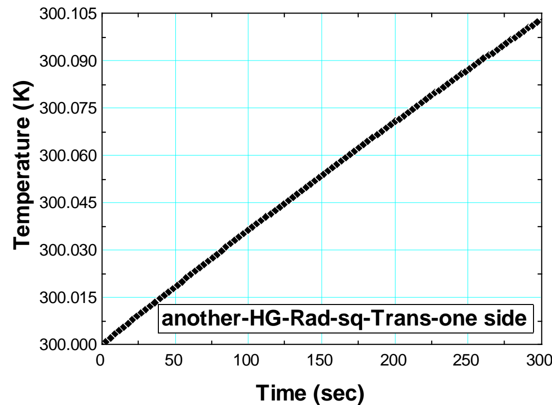

Figure 3.24 EES® result shows a temperature of exactly 300.103 K after 300 sec.

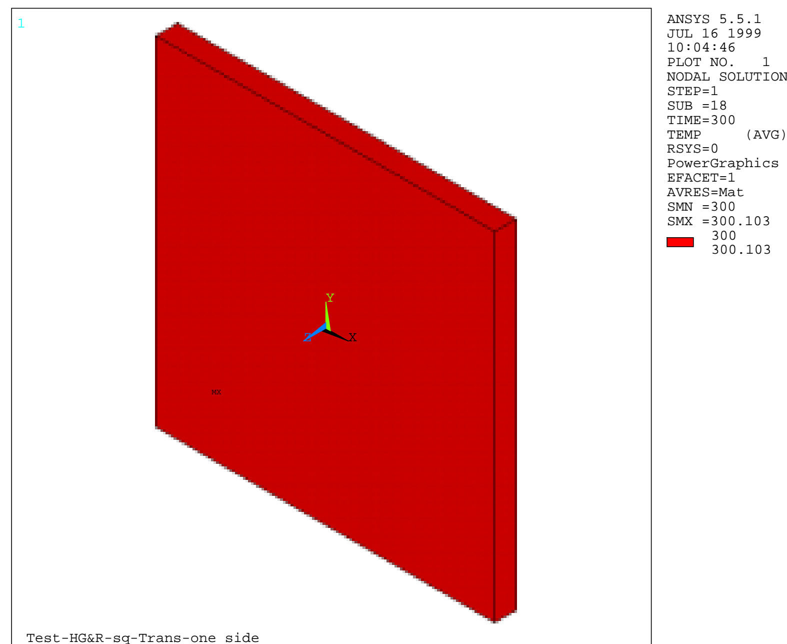

Figure 3.25 ANSYS® result shows a temperature of 300.103 K after 300 sec.

3.3.1b- Transient response of a lumped system with internal heat generation and radiation loss from both sides.

To be confident in radiation modeling using ANSYS®'s solid elements, the same problem is used again but with radiation from both sides. ANSYS® is compared to a finite

difference solution to the problem. The finite difference solution procedure uses the Euler approximation for the time derivative. Also, the area will be doubled to account for radiation from top and bottom surfaces.

$$q_{gen}\forall - \varepsilon\sigma A(T_i^4 - T_{\text{inf}\,inity}^4) = \rho\forall C\frac{T_i - T_{i-1}}{\Delta\tau} \tag{3.35}$$

Where $\Delta\tau$ is the time step, T_i is the temperature at the current time step while T_{i-1} is the temperature at the previous time step. Starting from an initial temperature of 300 K and a resonable time step for stability criteria then next value of the temperature at the node can be calculated from the previous temperature.

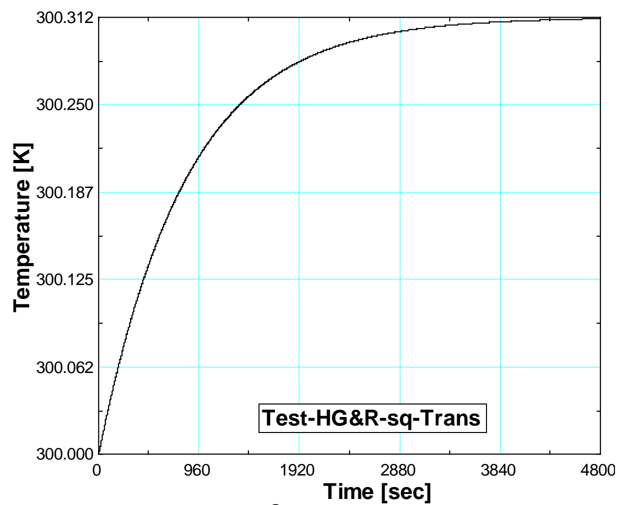

Figure 3.26 EES® result shows a temperature of 300.311 K after 4800 sec.

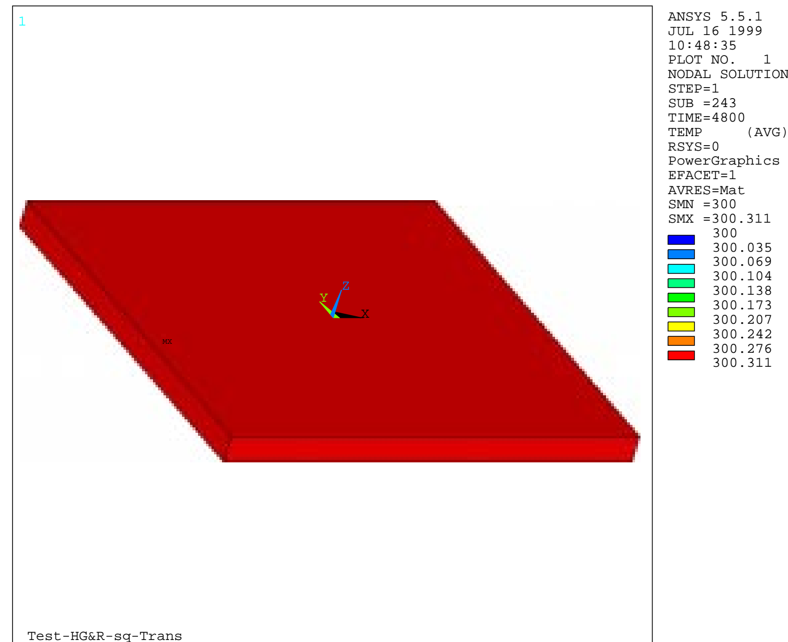

Figure 3.27 ANSYS® result shows a temperature of 300.311 K after 4800 sec.

Figures 3.26 and 3.27 show both the finite difference and ANSYS® solutions, which are identical as they are both show a temperature rise of 0.311 K over 4800 seconds. All the input parameters used for this problem are given in Table 3.3.

3.3.1c- Transient response of a lumped system with heat flux, radiation and convection heat loss from both sides.

Stepping one more step after the previous test case, and testing the transient behavior for the case of heat flux and convection over a square glass plate. The finite difference solution is basically the same one described in the previous two sections, the modifications are, changing the loading conditions and adding the convection heat loss, the same solution procedure will be used. Figure 3.28 shows the finite difference

solution of temperature response using EES®; it shows a temperature rise of 19.024 K over a 4800-second period. ANSYS® solution for this case give a temperature rise of 19.025 K over the 4800 second period, which means a very good agreement between ANSYS® and the finite difference solution.

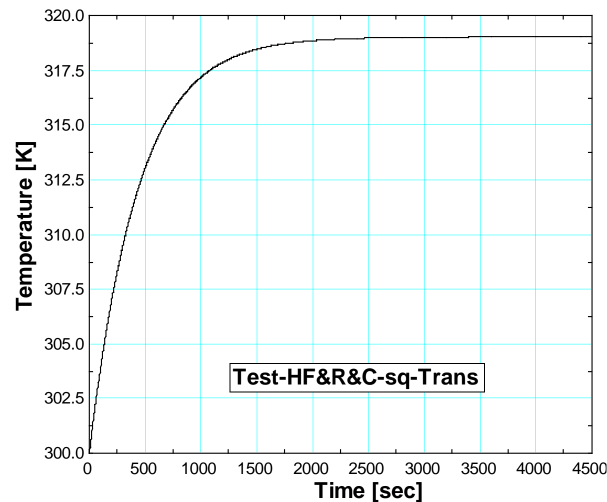

Figure 3.28 EES® result shows a temperature of 319.024 K after 4800 sec.

ANSYS® results also show a temperature of 317.042 K after 988 seconds, which agrees very well with Figure 3.28. All the input parameters used for this problem are given in Table 3.3.

3.3.1d- Transient response of a square plate with heat generation, heat flux, one-dimensional conduction, radiation and convection heat loss from both sides.

Now approaching more to the actual simulation condition and that by combining all the main heat loading together and heat loss together all for a transient analysis. The only difference between this case and the actual case is that in this case we are assuming one-

dimensional heat conduction to get the temperature distribution through the thickness with the time.

No analytical solution is available for this case, that is why a finite difference solution is used to be compared with the ANSYS® solution. Substituting with the boundary conditions including, convection, radiation, internal heat generation and surface heat flux in the transient one-dimensional conduction equation yields equation 3.36:

$$q_{flux}A + q_{gen}\forall - hA(T - T_{\inf inity}) - \varepsilon A\sigma(T^4 - T^4_{\inf inity}) = \rho C\forall \frac{dT}{d\tau} \tag{3.36}$$

Equations 3.37, 3.38 and 3.38 are finite difference scheme (using Crank-Nicolson method) used for solving equation 3.36.

$$\begin{aligned} & q_{flux}A_{top} + q_{gen}A_{top}\frac{\Delta\delta}{2} - hA_{top}\left[\frac{(T_{1,j} - T_{\inf inity}) + (T_{1,j-1} - T_{\inf inity})}{2}\right] \\ & - \varepsilon_{top}A_{top}\sigma\left[\frac{(T_{1,j}{}^4 - T^4_{\inf inity}) + (T_{1,j-1}{}^4 - T^4_{\inf inity})}{2}\right] - kA_{top}\left[\frac{(T_{1,j} - T_{2,j}) + (T_{1,j-1} - T_{2,j-1})}{2\Delta\delta}\right] \\ & = \rho C A_{top}\frac{\Delta\delta}{2}\left[\frac{T_{1,j} - T_{1,j-1}}{\Delta\tau}\right] \end{aligned} \tag{3.37}$$

Equation 3.37 valid only for the top surface node, where the heat flux q_{flux} is applied, $T_{1,j}$ is the temperature at the node number one (top surface node) and j is the time index indicating the current time step (where $j-1$ is the previous time step), A_{top} is the top surface area, h_{top} is the top surface heat transfer coefficient, ε_{top} is the emissivity of the top surface, k is the thermal conductivity. Also, q_{gen} is the heat generation rate per unit

volume, $\Delta\delta$ is the distance between ant two successive nodes in the thickness and $\Delta\tau$ is the time step.

For any intermediate node, the equation is different. There is no surface heat flux, no radiation, no convection; then the equation is:

$$\begin{aligned} & q_{gen}\Delta\delta A+\frac{kA}{\Delta\delta}\{[(T_{i-1,j}-T_{i,j})+(T_{i-1,j-1}-T_{i,j-1})]- \\ & [(T_{i,j}-T_{i+1,j})+(T_{i,j-1}-T_{i+1,j-1})]\}=\rho C\forall[\frac{T_{i,j}-T_{i,j-1}}{\Delta\tau}] \end{aligned} \tag{3.38}$$

For the bottom surface node, convection and radiation must be included but there is no heat flux term as:

$$\begin{aligned} & q_{gen}A_{bot}\frac{\Delta\delta}{2}-hA_{bot}[\frac{(T_{last,j}-T_{\inf inity})+(T_{last,j-1}-T_{\inf inity})}{2}] \\ & -\varepsilon_{top}A_{bot}\sigma[\frac{(T_{1,j}{}^{4}-T_{\inf inity}^{4})+(T_{1,j-1}{}^{4}-T_{\inf inity}^{4})}{2}]+kA_{top}[\frac{(T_{last-1,j}-T_{last,j})+(T_{last-1,j-1}-T_{last,j-1})}{2\Delta\delta}] \\ & =\rho CA_{bot}\frac{\Delta\delta}{2}[\frac{T_{last,j}-T_{last,j-1}}{\Delta\tau}] \end{aligned}$$

(3.39)

Solving this set of equations simultaneously, the transient temperature response can be obtained as a function of the position and the time.

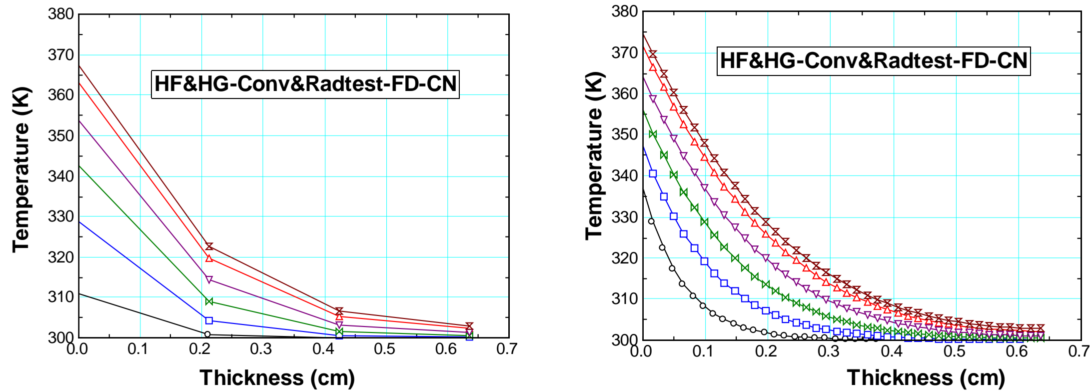

Figure 3.29 Temperature distribution through the thickness and with the time for 4-nodes and 40-nodes in the mask thickness.

Figure 3.29 shows the finite difference result for four nodes and forty nodes. The temperature through the mask is shown at the first 6 second (i.e., after 1, 2, 3, 4, 5 and 6 seconds). All the input parameters used for this problem are given in Table 3.3. After 6 seconds, the four-node solution has a maximum temperature of about 368 K while the forty-node solution has a maximum temperature of 377 K.

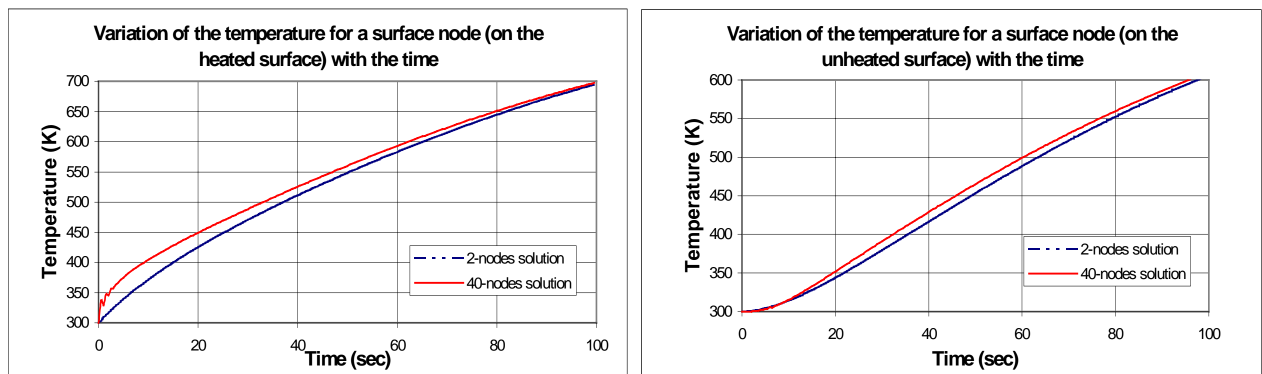

Figure 3.30 Comparison between the temperature variation with the time for 2-nodes solution and 40-nodes solution using finite difference technique.

It is true that the transient temperature response is different when changing the number of nodes in the depth, but that difference diminishes as the time go on and steady state

conditions (or periodically steady state) is approached. Figure 3.30 shows the temperature response for two nodes, one on the heated surface and the other on the unheated surface, with the time for both 2-nodes and 40-nodes solution. It can be noticed that with increasing the time, there will be no difference in the solution.

3.3.2 Mask with pattern

Predicting the full three-dimensional temperature field is the goal of this section. Also, the timing of the on-off heating process must be added to simulate the actual manufacturing process. During manufacturing, the energy input will be pulsed on the mask surface such that the power is on during "light on" periods and the power is off during "light off" periods. The cycle repeats and ultimately reaches a periodic steady state.

The period during which the light is on is simulated by a certain amount of energy absorbed through the mask thickness (described by equation 3.25) and another amount of energy applied as heat flux over the bottom surface of the mask (described by equation 3.28). The magnitude of these energy terms depends on the lighting energy. During the period where the light is off, heat generation and heat flux are turned off in the simulation. Heat loss by conduction, radiation and convection are always on.

3.3.2.1-Preliminary run.

A preliminary test case is investigated as a step towards the actual manufacturing conditions. A case with a half-second on and a half-second off light is simulated until it reaches the periodic steady state condition. The duty cycle is shown in Figure 3.31.

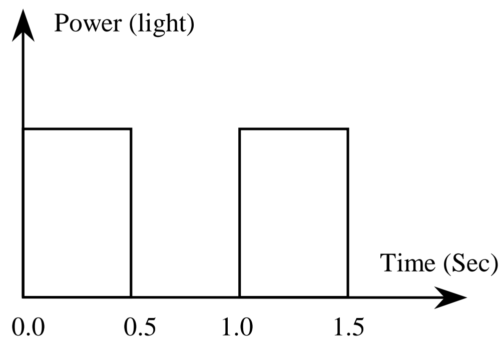

Figure 3.31. Mask duty cycle for preliminary run case.

For this transient analysis, a patterned mask will be simulated, by assuming uniform chrome coverage. Heat transfer coefficient and emissivities from the top and bottom are different due to the pellicle effect as discussed in Section 3.1 in this chapter. A quarter symmetry model is used to reduce the number of nodes, which reduces the needed storage space for this transient analysis. The thermal boundary condition assumed in this problem is that the points of contact between the mask and the mounting are at a fixed temperature of 300 K. This boundary condition was assumed as the mass and the thermal conductivity of the mounting are much higher that that of the fused silica mask.

Figure 3.32 shows the maximum temperature versus the time for two time ranges to show the steady state in the long-term graph and to show details in the short term one. It is shown that about 2500 seconds are needed to reach the periodic steady state condition, and that the temperature rise is about 11 K. The short-term period figure shows the heating and cooling cycle of the mask surface due to the on-off thermal loading. The short-term temperature variation is about 0.1 K.

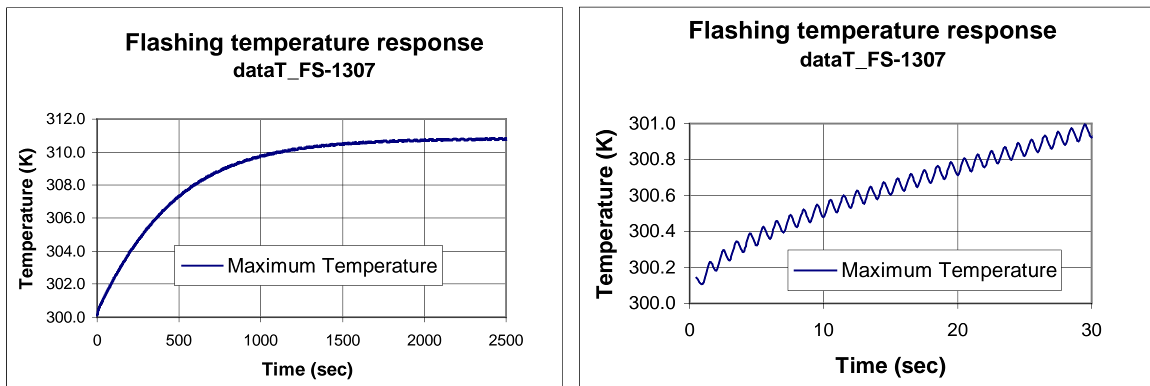

Figure 3.32 Temperature response with time.

Figure 3.33 shows the contour plot of the temperature distribution at the periodic steady state. The parameters used for this simulation are summarized in Table 3.4.

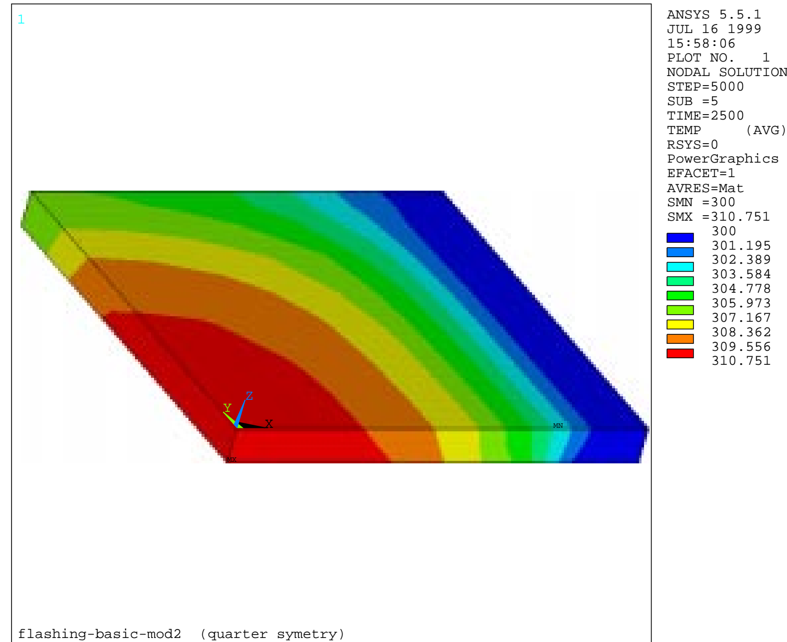

Figure 3.33 Temperature contours at periodic steady state.

Table 3.4. Input parameters for the flashing problem.

Dimensions	Outer sides length	15.24 cm
	Exposure sides length	13.2 cm
	Mask thickness δ	0.635 cm
Applied load	Lighting power	0.1 W/cm^2
Pattern characteristics	Glass absorption coefficient	0.4% 1/cm
	Chrome absorptivity	50%
	Chrome coverage	90%
Heat transfer characteristics	Ambient temperature T_∞	300 K
	Emissivity ε	0.9
	Top heat transfer coefficient	5e-4 W/ cm^2-K
	Bottom heat transfer coefficient	2.5e-4 W/ cm^2-K
Model parameters	Duration of light on	0.5 sec
	Duration of light off	0.5 sec
Material properties (Fused Silica)	Thermal conductivity k	0.0138 W/cm-K
	Density ρ	2202 E-6 g/cm^3
	Specific heat C	746 J/kg-K

To check the ANSYS® model used for this simulation some simple checks were performed.

1- A lumped system was assumed with half the power all the time. The thermal conductivity in ANSYS® was set to a large value. The numerical EES® formulation is given in section 3.3.1d.
2- The steady state temperature for the lumped system was calculated by assuming one half of the power was on all the time until steady state was reached. This steady state problem was solved with both EES® and ANSYS®.

Both testes were performed and good agreement was found between the ANSYS® and EES® solutions.

3.3.2.2-Simulating the actual duty cycle.

All of the work previously presented was to reach a high confidence level in simulating the actual full field exposure process. The model includes the actual duty cycle performed on the mask during wafer fabrication. The actual duty process is different from the previous preliminary run only by the timing for light application and delay timing. The flash delay time, which occurs after completing one field on the wafer (i.e., during wafer stepping), must be included. Also, the wafer delay, which is the time delay after completing one wafer (i.e., during wafer changing), must be included. The mask duty cycle represented in the current simulation is shown in Figure 3.2. The parameters used in the simulation of this problem are listed in Table 3.5.

Table 3.5. Input parameters for the flashing problem.

Dimensions	Outer sides length	15.24 cm
	Exposure area	10.0cm ×12.8cm
	Mask thickness δ	0.635 cm
Applied load	Lighting power	16.64 mW/cm^2
Pattern characteristics	Glass absorption coefficient	0.4% 1/cm
	Chrome absorptivity	50%
	Chrome coverage	90%
Heat transfer characteristics	Ambient temperature T_∞	300 K
	Top Emissivity	0.9
	Bottom Emissivity	0.5
	Top heat transfer coefficient	5e-4 W/ cm^2-K
	Bottom heat transfer coefficient	2.5e-4 W/ cm^2-K
Model parameters	Light applied duration	38 msec
	Flash delay	100 msec
	Wafer delay	15 sec
	Number of field per wafer	30
Material properties (Fused Silica)	Thermal conductivity K	0.0138 W/cm-K
	Density ρ	2202 E-6 g/cm^3
	Specific heat C	746 J/kg-K

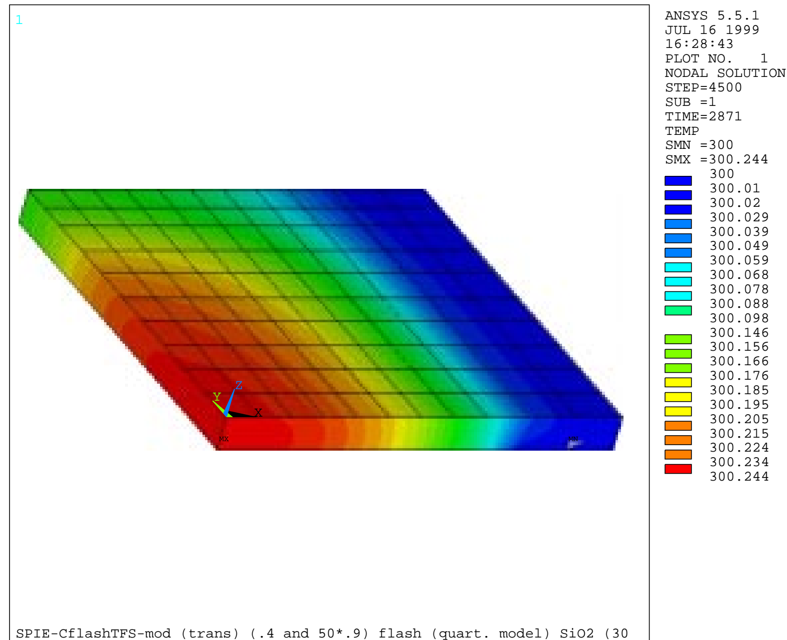

Figure 3.34. Contour plot of the temperature using ANSYS®.

The results from the ANSYS® solution is given in Figure 3.34 where a temperature contour plot is shown for the mask after reaching periodic steady state condition. A schematic of the mask showing the dimensions and the boundary conditions are given in Figure 3.35.

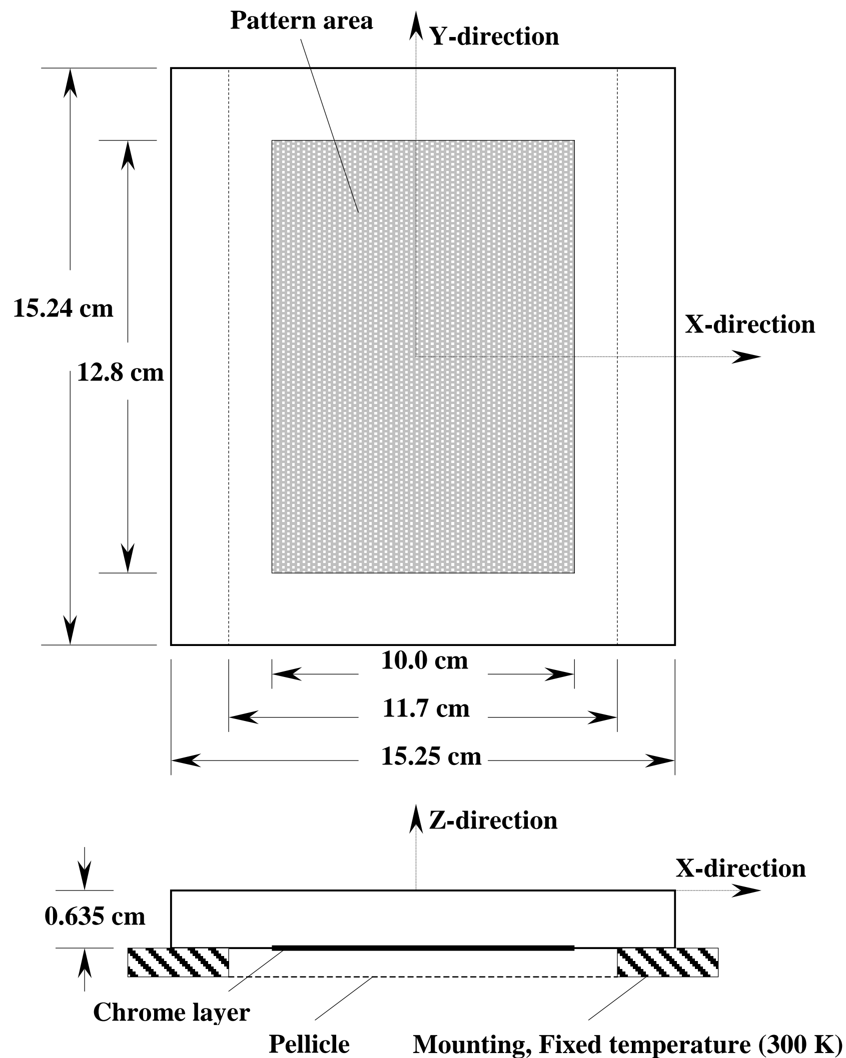

Figure 3.35 Mask dimensions and Boundary conditions [ref. 3.4].

3.4 Summary

In this chapter, some ANSYS® test models were developed and checked with an analytical solution or a finite difference solution in order to reach a high confidence level in the modeling before simulating the actual exposure process. These test models were presented in the ascending order of complication till the modeling reached the actual exposure process itself. The thermal result of the full field exposure was presented in this chapter.

3.5 References

[3.1] ANSYS® versions 5.3, 5.4 and 5.5, ANSYS, Inc. 1999.

[3.2] F. P. Incropera and D. P. DeWitt, "Fundamentals of Heat and Mass Transfer," Fourth edition, John Wiley & Sons, Inc., 1996.

[3.3] S. A. Klein and F. L. Alvarado, "EES, Engineering Equation Solver," University of Wisconsin-Madison, Version 5.115, 1999.

[3.4] J. Chang, A. Abdo, B. Kim, T. Bloomstein, R. Engelstad, E. Lovell, W. Beckman and J. Mitchell, "Thermomechanical Distortions of Advanced Optical Reticles during Exposure," Proceedings of the 1999 SPIE symposium on Emerging Lithography Technologies III, Vol. 3676, pp. 756-767, 1999.

Chapter Four
Thermal distortion during exposure – Full Field Exposure

4.1 Introduction

The main goal of this work is to predict the distortion due to thermal loading on an optical mask during exposure. The procedure of predicting this thermal distortion must be done in two steps. The first step is to solve the problem using thermal elements to obtain the temperature distribution due to the thermal loading. The second step is to use the thermal results as input to structural elements to obtain the distortion. The main concern in the previous chapter was solving for the temperature history on the mask during full field exposure. In this chapter the second step results will be presented.

The thermal distortion simulations will be performed for both the steady-state analysis and for the transient analysis already discussed in the previous chapter. As was done for the thermal model some test cases to benchmark the ANSYS® structural models will be presented first.

4.2. Test cases

Both simple and complex problems will be used to verify the ANSYS® structural models. The simple problems are a circular hot spot in a finite circular plate and a circular hot spot in an infinite circular plate, both with well-known analytical solutions. The complicated problem is a square mask subjected to heat flux with classical boundary

conditions. Bloomstein [ref. 4.1] obtained the analytical solution for the square mask. The last case, a square hot spot in an infinite square plate, will be presented to compare the result of ANSYS® using two different solution methods. (The analytical solution to this problem [ref. 4.2] appears to be in error, as it shows no σ_x on the x-axis or on the diagonal out of the hot area, which can not be true).

4.2.1 Circular hot spot in a finite circular plate.

The circular hot spot in a finite circular plate problem will be solved by two methods using ANSYS®, and both will be compared with the analytical solution. The first method uses shell 63, a two-dimensional element type that supports both mechanical and thermal loading. The second method separates the solution by solving first the thermal domain by using the two-dimensional thermal element, shell 57, then solving for the distortion using the structural element shell 63.

Dr. Ted Bloomstein from MIT Lincoln Labs obtained the analytical solution for this problem [ref. 4.1] and is summarized in the following paragraphs. It is assumed that the temperature profile in the hot zone is in the form of a hat: the temperature in a circular area of radius r_{hot} is uniformly higher than the temperature outside the hot zone from r_{hot} to r_{out}. The temperature difference ΔT and the stress in the hot zone σ_{hot} are related by:

$$\sigma_{hot} = \frac{E\alpha\Delta T}{2}\left(1 - \frac{r_{hot}^2}{r_{out}^2}\right) \qquad (4.1)$$

where E is the modulus of elasticity (N/m^2) and α is the coefficient of thermal expansion(1/K). This stress is constant inside the hot zone ($0 \le r \le r_{hot}$). Outside the hot zone ($r_{hot} \le r \le r_{hout}$) the radial stress σ_r is different than the tangential stress σ_t (the third direction stress is assumed to be zero for this two-dimensional problem). The radial stress σ_r and the tangential stress σ_t are given by:

$$\sigma_r = \sigma_{hot} \frac{r_{hot}^2}{r_{out}^2 - r_{hot}^2}(1 - \frac{r_{out}^2}{r^2}) \tag{4.2}$$

$$\sigma_t = \sigma_{hot} \frac{r_{hot}^2}{r_{out}^2 - r_{hot}^2}(1 + \frac{r_{out}^2}{r^2}) \tag{4.3}$$

where r is any radius between r_{out} and r_{hot}. Figure 4.1 shows a comparison between the analytical given by equations 4.1, 4.2 and 4.3 and the two ANSYS® solutions: the agreement is very good. σ_X and σ_Y in the ANSYS® solution is equivelant to σ_r and σ_t in the analytical solution, as a Cartesian coordinate system was used in ANSYS®.

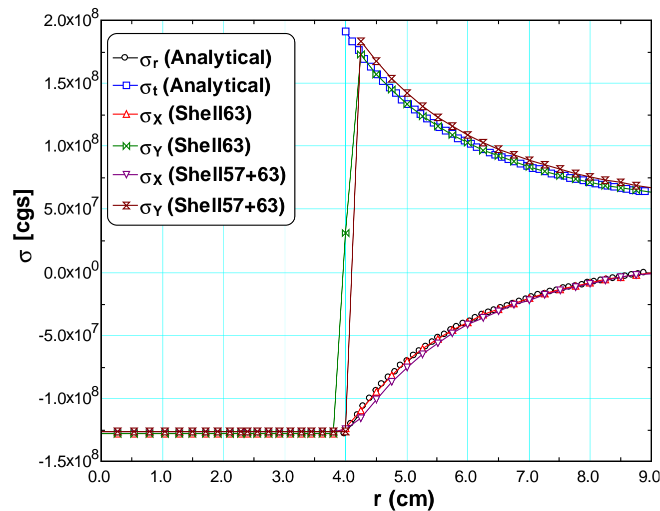

Figure 4.1 Comparison between the analytical solution and the ANSYS® solutions.

Figure 4.2 shows the temperature contours using ANSYS® for the case of finite hot spot.

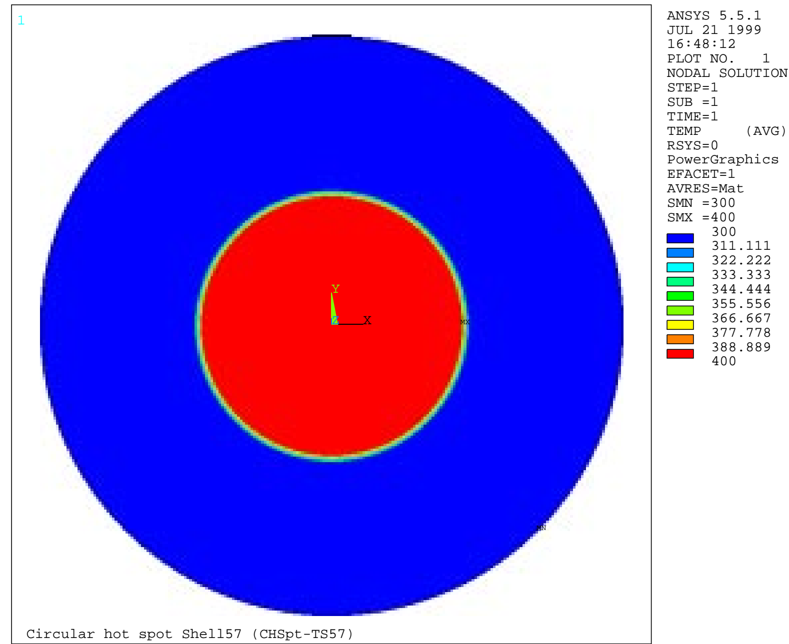

Figure 4.2 ANSYS® temperature contour plot.

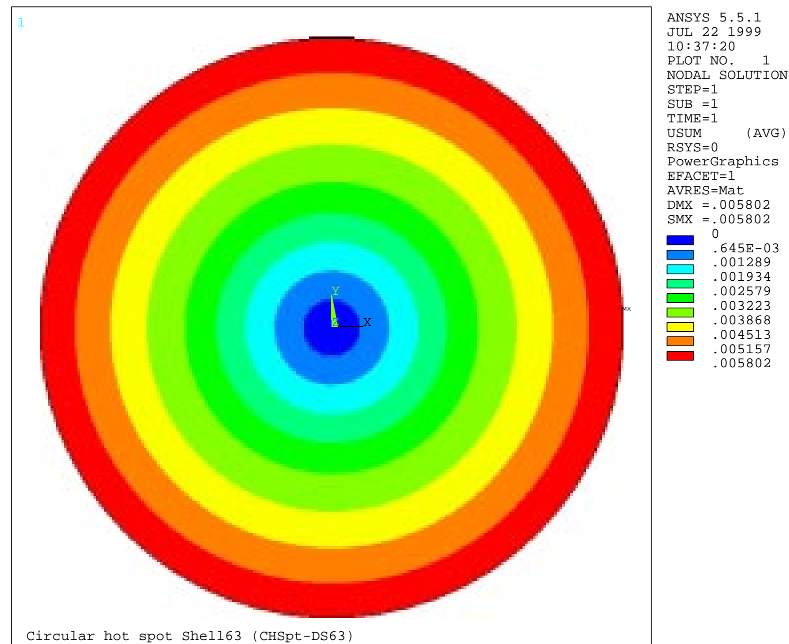

Figure 4.3 ANSYS® radial displacement contour plot.

Figure 4.3 shows ANSYS® contour plot for the radial displacement. As expected for this problem, the circular plate expands in the radial direction.

4.2.2 Circular hot spot in an infinite circular plate.

Another problem with known analytical solution is the circular hot spot in an infinite circular plate. The analytical solution for the hot spot in finite circular plate i.e., equations 4.1, 4.2 and 4.3 are valid for the case of hot spot in infinite circular plate. The case is not true the other way, i.e., the special solution for circular hot spot in infinite plate is not valid for the finite plate problem. The difference between the finite hot spot and the infinite hot spot is the area ratio of the circular hot region to the total area of the circular plate. For this case, the hot area to the total area ratio is about 70. This time a solid element was used in the analysis, solid 70 for the thermal modeling and solid 45 for the structural modeling, to check if there will be any difference between solid and shell elements.

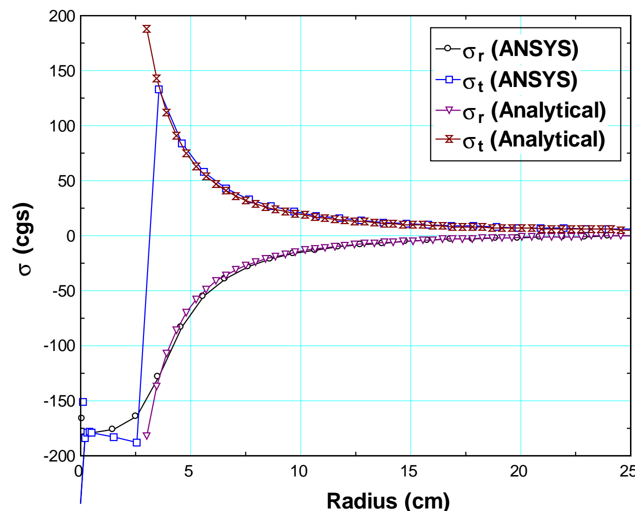

Figure 4.4 Comparison between the analytical solution and the ANSYS® solution.

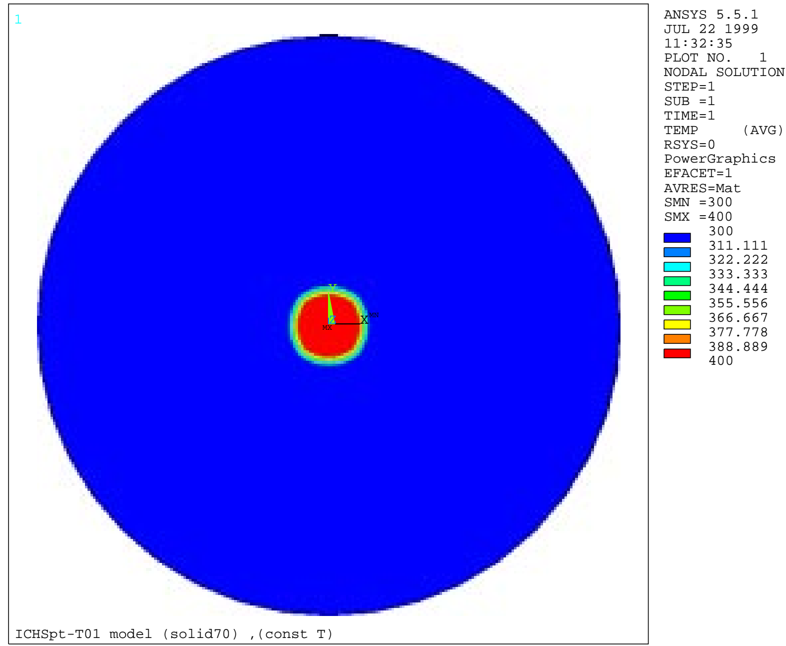

Figure 4.5 ANSYS® temperature contour plot.

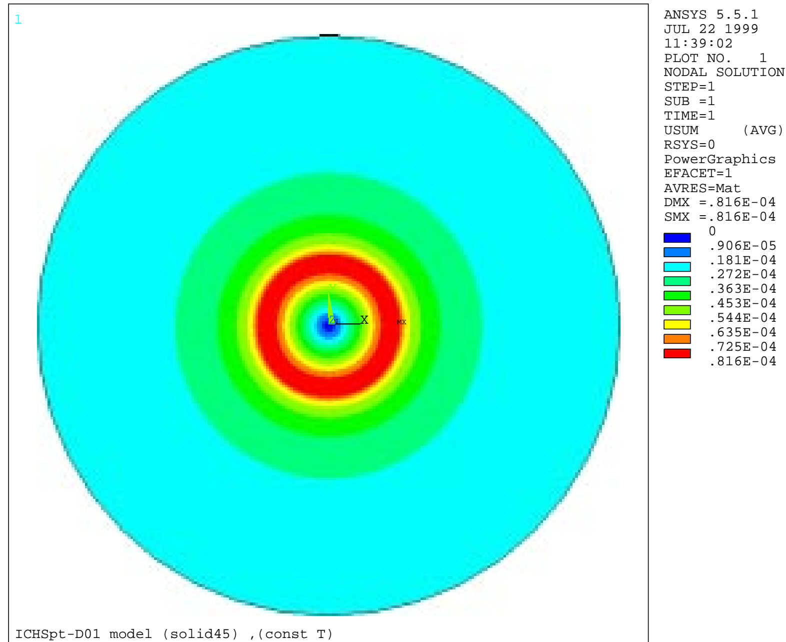

Figure 4.6 ANSYS® radial displacement contour plot.

Figure 4.4 shows a comparison between the analytical solution and ANSYS® solution using three-dimensional solid elements (solid 70 and solid 45). Figures 4.5 and 4.6 show ANSYS®solutions for both temperature and displacement. The solution with solid element produces shear stress which affects the solution if compared with the corresponding two-dimensional problem, that is the reason of the small difference shown in Figure 4.4 even by taking a very thin solid element in the solution.

4.2.3 Square hot spot in an infinite plate.

Now let us move to the next step closer to our goal. The mask under investigation is of a rectangular or square shape. The circular hot spot was used because its exact analytical solution was completely known. The analytical solution for the square hot spot was found in some references [ref. 4.2 and ref. 4.3] but it was very difficult and it was not easy to understand, the solution was different than what we got from ANSYS® simulation. As the analytical solution could not be compared with ANSYS®'s solution, two independent and different ANSYS® solutions will be compared with each other. They are both the problem of a square hot spot in an infinitely large square plate. The first solution used shell 63 element, which is a thermo-mechanical element, by defining a thermal stress due to hot zone. The other solution is to use thermal shell element (shell 57) and constrain the nodes in the hot zone to be higher than the nodes outside it by the desired temperature difference, then take the temperature distribution and solve for the stresses by using structural shell element (shell 63). Both solutions gave the same answer

for x-direction and y-direction stress distribution along a vertical line and a horizontal line.

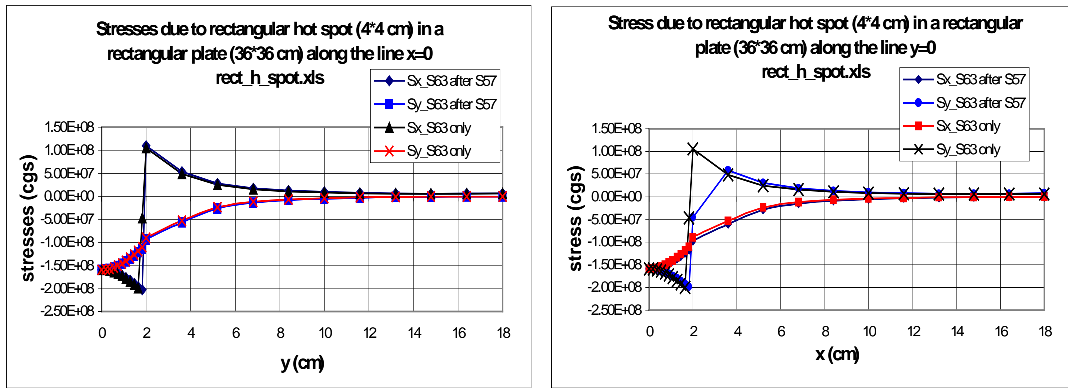

Figure 4.7 Solution for square hot spot in infinite plate using two ANSYS® methods.

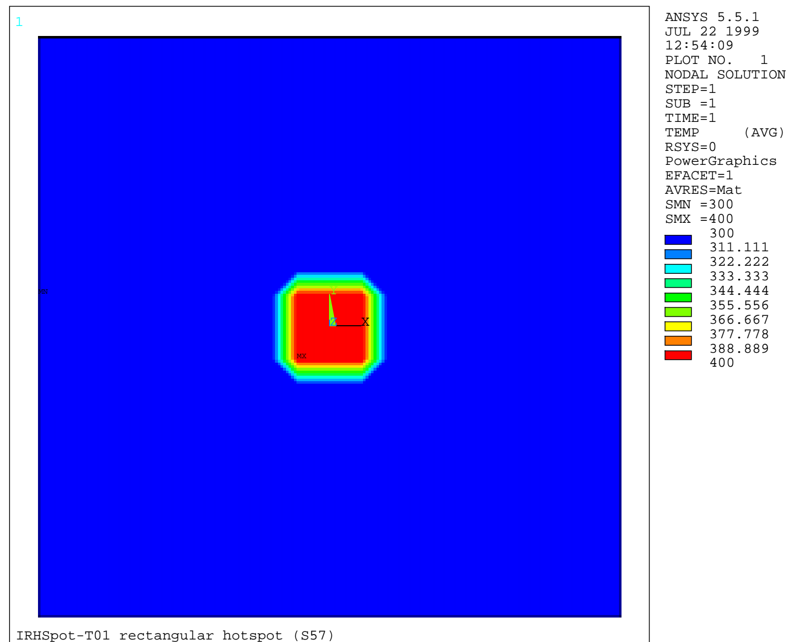

Figure 4.8 ANSYS® temperature contour plot (shell 57 only).

Figure 4.7 presents the comparison between the two ANSYS® solutions; it can be seen that the two solutions agree.

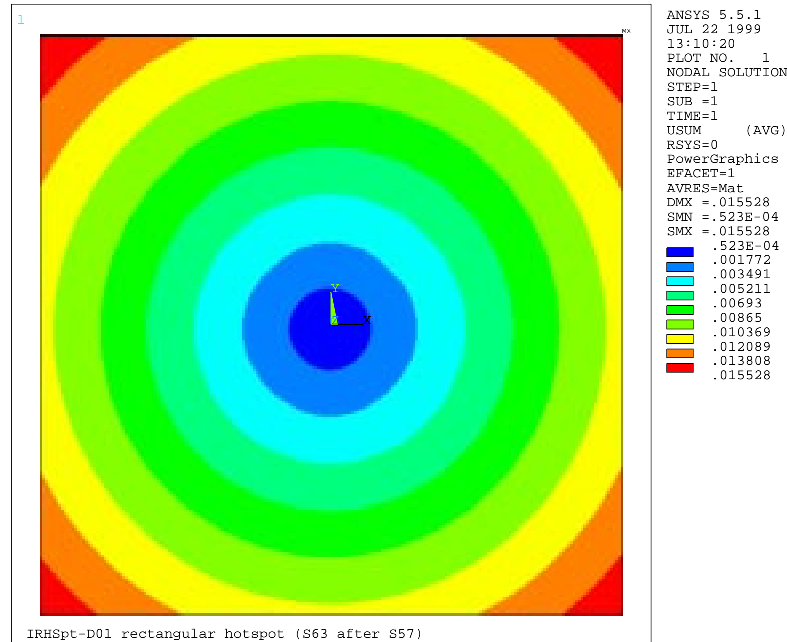

Figure 4.9 ANSYS®radial displacement contour plot (shell 63 after 57).

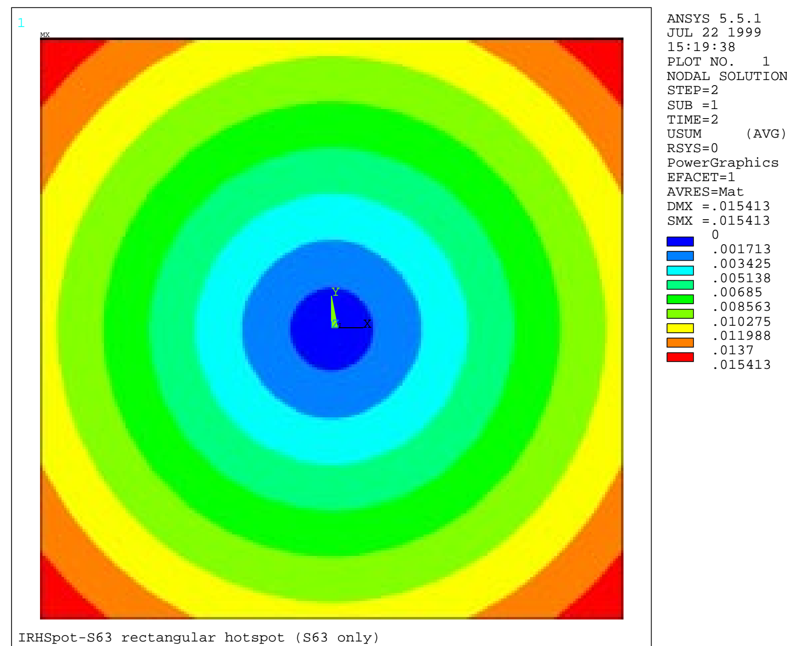

Figure 4.10 ANSYS®radial displacement contour plot (shell 63 only).

Figures 4.8 and 4.9 show ANSYS® result by using both shell (shell 57 then shell 63) elements independently, while Figure 4.10 shows ANSYS® results when using only one element (shell 63).

4.2.4 Simplified full field exposure case.

As the analytical solution could not be obtained for the square hot spot, another analytical solution is used to benchmark ANSYS®. The actual full field exposure could not be solved analytically; some simplifications must be made in order to obtain an analytical solution to allow this comparison. A square mask will be considered with an applied heat flux only on a smaller square area of the top surface, which is the exposure area or the patterned area shown in Figure 3.20. The thermal boundary condition is such that the four edges of the square mask will be fixed at the ambient temperature. The analysis is steady state with no radiation or convection heat losses. An ANSYS® three-dimensional thermal element, solid 70, will be used to obtain the thermal results. This thermal result is then used as an input to ANSYS® using three-dimensional structural element, solid 45, for the structural analysis. The mechanical boundary condition is such that the translation is constrained in the out of plane direction (normal to the mask plane) at the mid-surface along the four edges, i.e., simply supported. ANSYS® temperature and out of plane (OPD) distribution on mid-plane of the mask was compared with the analytical solution given by Dr. Ted Bloomstein from MIT Lincoln Labs [ref. 4.1] for both fused silica and calcium fluoride materials and a perfect agreement was found. Figure 4.11 shows the comparison between ANSYS® solution and the analytical solution for the case of fused

silica material. ANSYS® solution shows the temperature distribution on the symmetric axis over the top, mid plane and bottom surfaces, it can be noticed that there is not much difference between them. The analytical solution was presented only on the mid plane surface. Figure 4.11 also present the out of plane distortion (OPD) distribution on the symmetric axis over the top, mid plane and bottom surfaces of the mask, the analytical solution is presented only on the midplane surface of the mask and it shows a very good agreement with ANSYS® results.

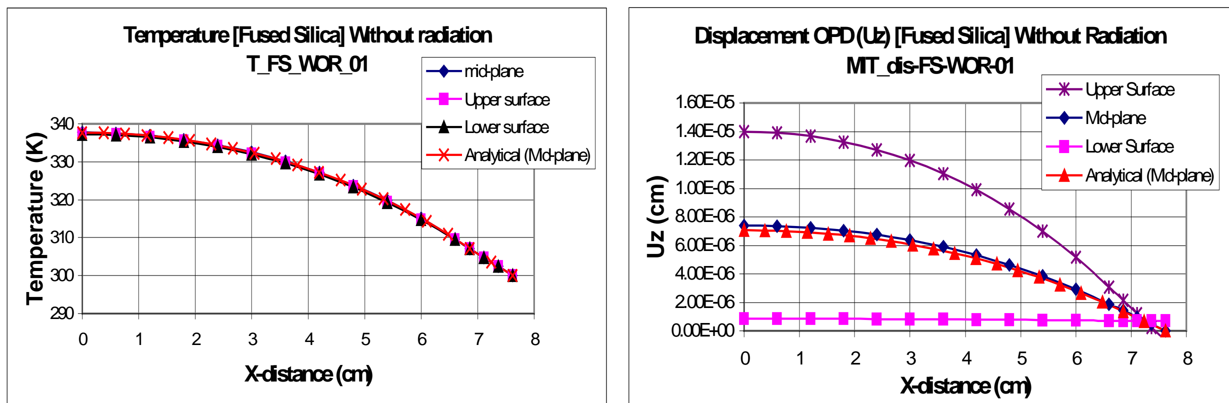

Figure 4.11 Comparison between analytical solution and ANSYS® solution for SiO_2.

Figure 4.12 shows the temperature contour plot over a quarter symmetry model for the fused silica material. Figure 4.13 shows the contour plot of the OPD for a quarter symmetry model (fused silica).

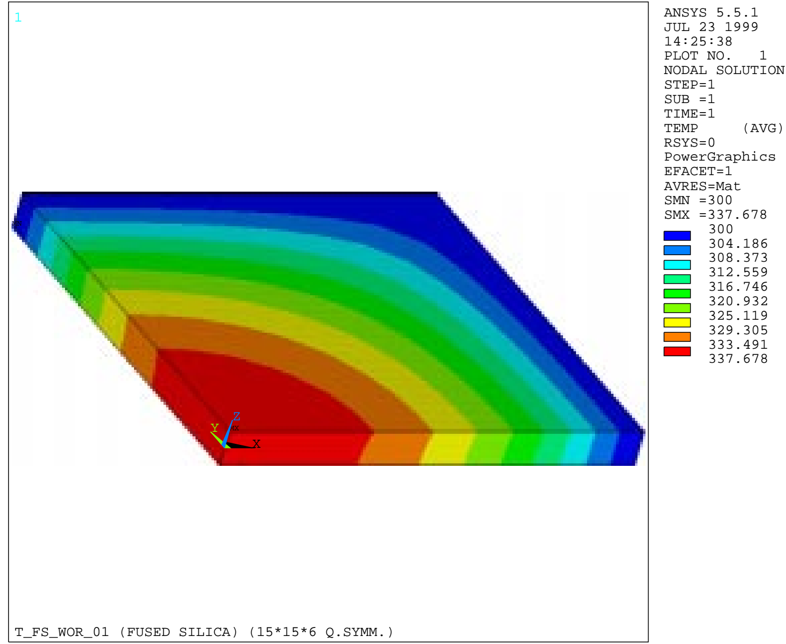

Figure 4.12 Temperature contours for fused silica without radiation.

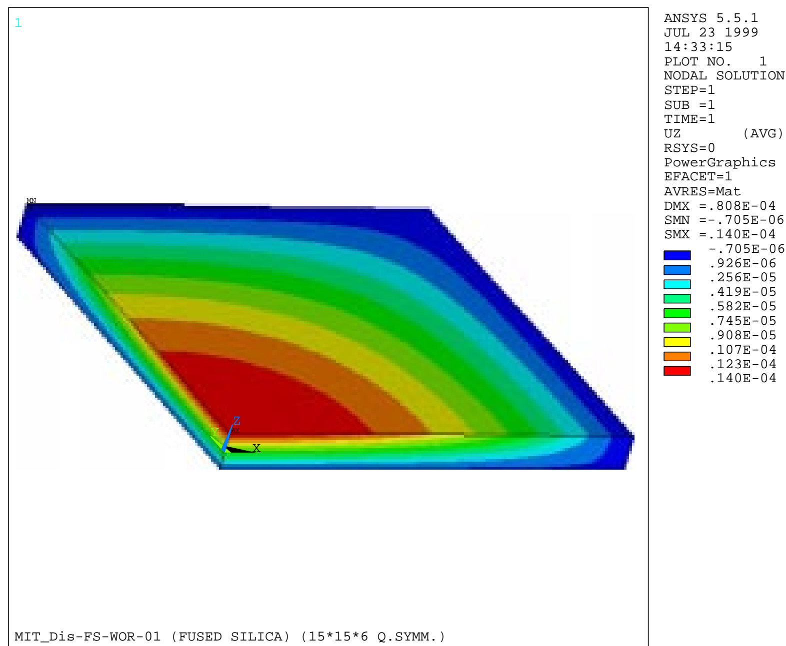

Figure 4.13 OPD contours for fused silica without radiation.

Figure 4.14 shows the comparison again between ANSYS® results and the analytical results for the calcium fluoride material. Comparing the results for both calcium fluoride and fused silica materials show that calcium fluoride has a lower temperature rise and higher OPD. The reason of that the calcium fluoride has a higher OPD compared to fused silica is that calcium fluoride (k = 0.097 W/cm-K) has about nine times the thermal conductivity of fused silica (k = 0.0138 W/cm-K) and calcium fluoride (α = 18.9E-6 1/K) has about forty times the thermal expansion of fused silica (α = 0.51E-6 1/K).

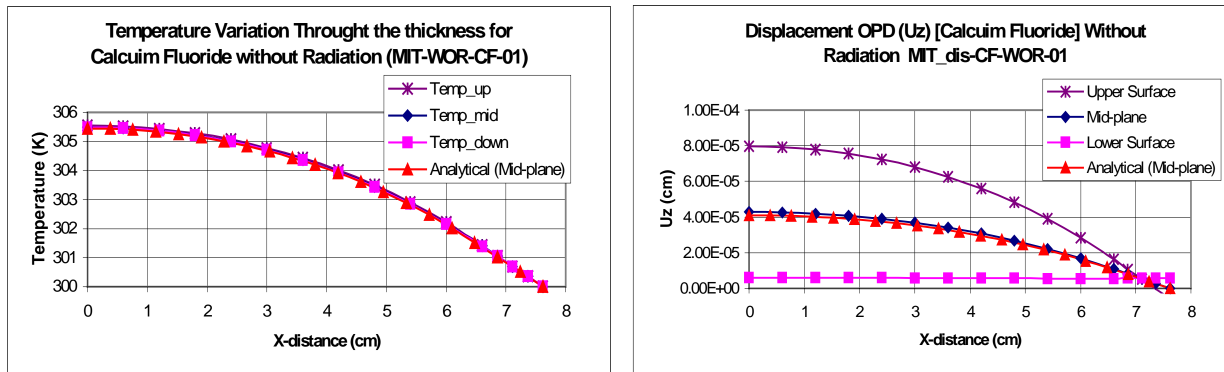

Figure 4.14 Comparison between analytical solution and ANSYS® solution for CaF_2.

The analytical solution is not valid for the case with radiation heat loss, but after the validation of the ANSYS® model, it can be used for the solution of the problem with radiation heat loss. Figures 4.15 shows the temperature and OPD results for fused silica with radiation heat loss. The temperature and OPD distributions are shown on the symmetric axis over the top, mid plane and bottom surfaces of the mask. Figures 4.16 shows the same results for calcium fluoride material.

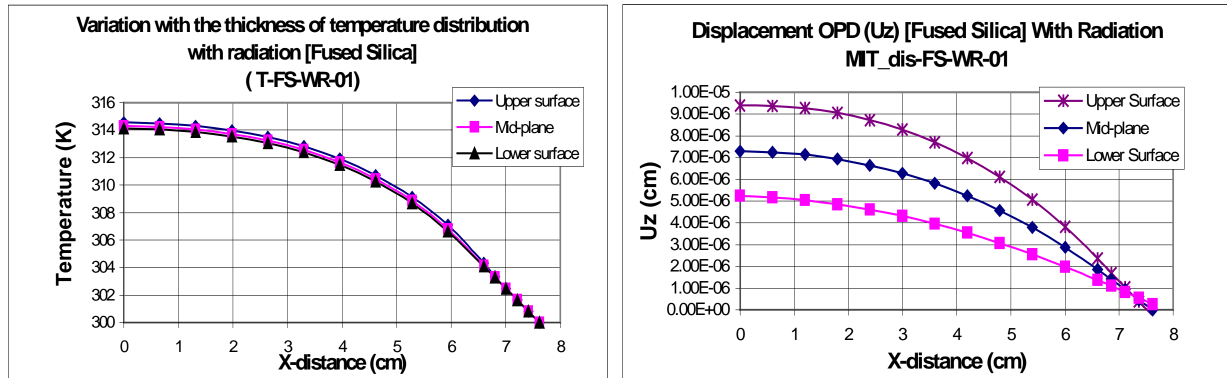

Figure 4.15 ANSYS® solution for SiO_2 case with radiation.

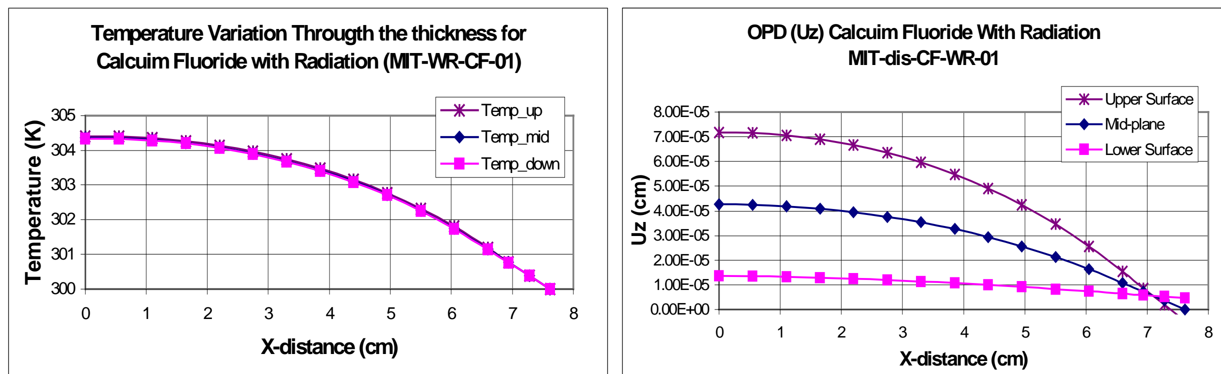

Figure 4.16 ANSYS® solution for CaF_2 case with radiation.

For checking the complete model a full mask model was used to repeat the quarter symmetry model results and check that there is no mistake in the models. Figure 4.17 and 4.18 show the temperature and OPD contours for calcium fluoride with radiation heat loss.

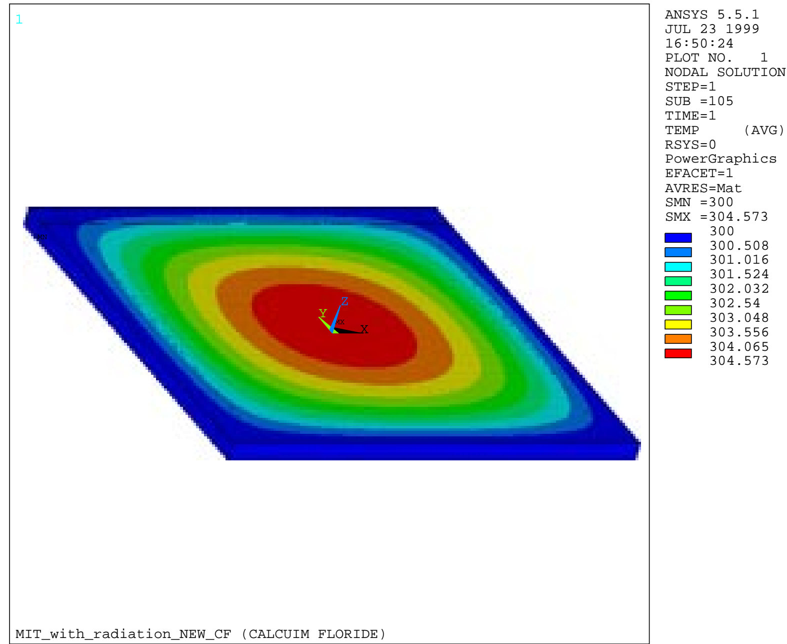

Figure 4.17 ANSYS® temperature contour for CaF_2 case with radiation (full model).

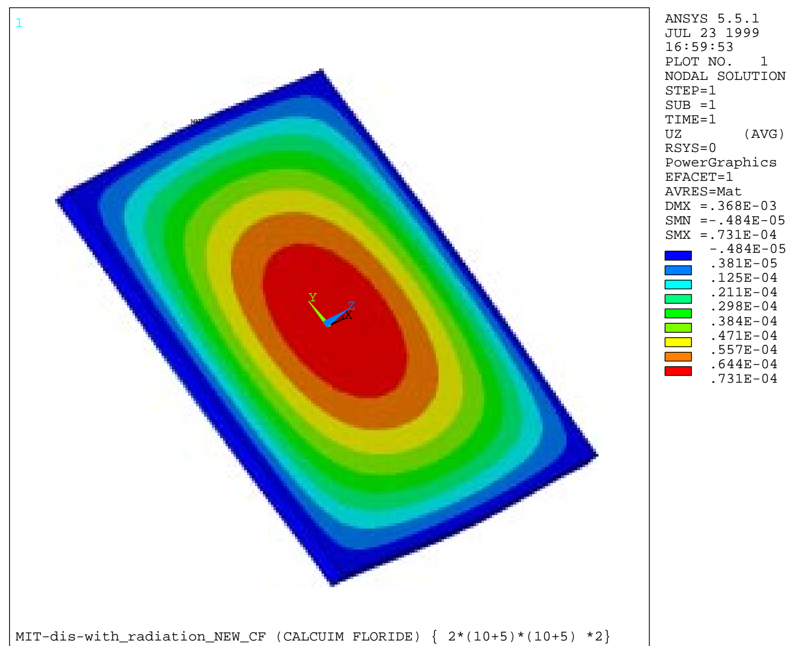

Figure 4.18 ANSYS® OPD contour for CaF_2 case with radiation (full model).

Some other simple test cases were obtained during the solution of the previous problem to understand the ANSYS® structural solution. These solutions are very simple checks to benchmark ANSYS® and to be sure that the ANSYS®'s structural solution is fully understood.

4.2.4.1 Constant temperature difference.

In the first test case a temperature difference of 5 ° was applied to all the nodes (between the initial state and the final state) of a square mask. The procedure was to set the reference temperature to 300 K and then set the ANSYS® thermal element solid 70 to be 305 K on all nodes. The next step is to solve this problem for distortion using the thermal results and using ANSYS® structural element solid 45. The advantage of this simple test is that we can compare ANSYS® result to the simple equation of thermal expansion, which is

$$\Delta\delta = \alpha\delta\Delta T \quad (4.4)$$

where, δ is the original thickness (0.635 cm) , $\Delta\delta$ is the change in the thickness, α is the ceffecient of thermal expansion (for this test case it was assumed to be 18.7e-6 1/K) and ΔT is the temperature difference (5 K). By applaying this equation we can find that the change in thickness $\Delta\delta$ will be 0.0000593725 cm. Figure 4.19 shows the result from the ANSYS® solution for the nodes on the symmetric axis over the top, midplane and bottom surfaces. The figure shows that the difference between top and bottom is exactly the same number calculated from equation 4.4. In the solution the midplane nodes do not

move, the upper surface nodes move upward half the OPD and the bottom surface nodes move downward the other half of the OPD.

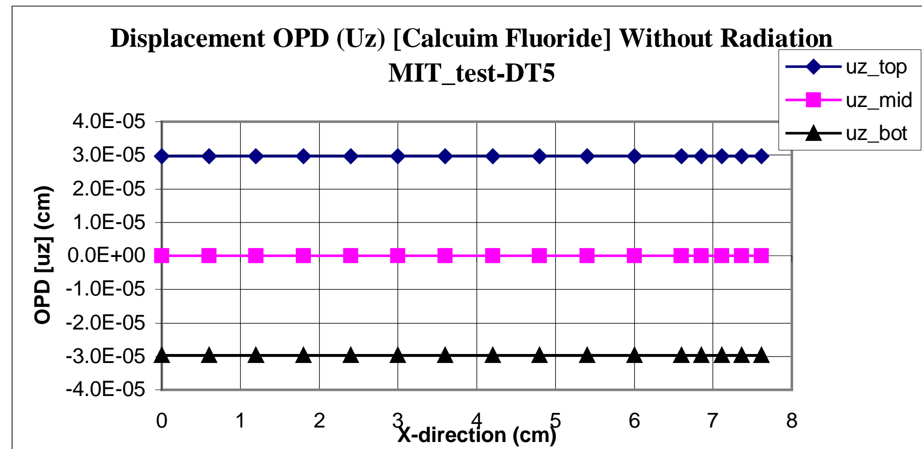

Figure 4.19 OPD for calcium fluoride with fixed temperature difference.

4.2.4.2 Infinite thermal conductivity in the thickness.

The same problem as discussed in section 4.2.4.1 was investigated but with infinite thermal conductivity in the z-direction (i.e., the thickness). With an infinite thermal conductivity in the z-direction, the temperature will be the same at the top and bottom surfaces (no temperature gradient in the thickness). For this case, the OPD will be symmetric on the top and bottom surfaces as shown in Figure 4.20. The mask will expand such that the upper OPD is positive, the bottom OPD is of the same value but negative and no OPD for the midplane surface.

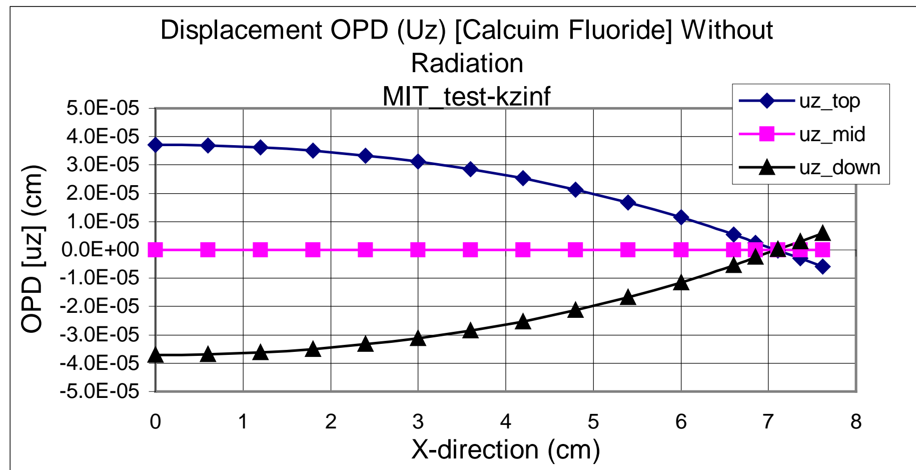

Figure 4.20 OPD distribution for CaF_2 with infinite thermal conductivity in the z-direction.

4.3. Thermal distortion during full field exposure.

4.3.1 Steady state analysis

The verified model is now ready to predict the thermal distortion during exposure for more complicated problems. A three-dimensional solid element with full thermal and mechanical characteristics simulating the actual exposure process will be used in this analysis. Steady state analysis will be used first, the distortion due to thermal loading during exposure for the case of a mask with pattern presented in Section 3.2.3 will be simulated and discussed in this section. Steady state analysis does not require very long computational time relative to transient problems. The input parameters for the problem are given in Table 4.1. The mechanical boundary conditions were assumed to be such that the central node at midplane was completely clamped.

Table 4.1. Input parameters for the square mask test cases.

Dimensions	Outer sides length	10 cm
	Exposure sides length	8 cm
	Mask thickness δ	0.635 cm
Applied load	Lighting power q_{light}	0.1 W/cm^2
Pattern characteristics	Glass absorption coefficient	0.4% 1/cm
	Chrome absorptivity	50%
	Chrome coverage	90%
Heat transfer characteristics	Ambient temperature T_∞	300 K
	Emissivity ε	0.9
	Heat transfer coefficient	5e-4 W/ cm^2-K
Material properties (Fused Silica)	Thermal conductivity k	0.0138 W/cm-K
	Density ρ	2202 E-6 g/cm^3
	Specific heat C	746 J/kg-K
	Young's modulus of elasticity E	72.6E5 N/ cm^2
	Poisson's ratio ν	0.164
	Thermal expansion coefficient α	0.51E-6 1/K

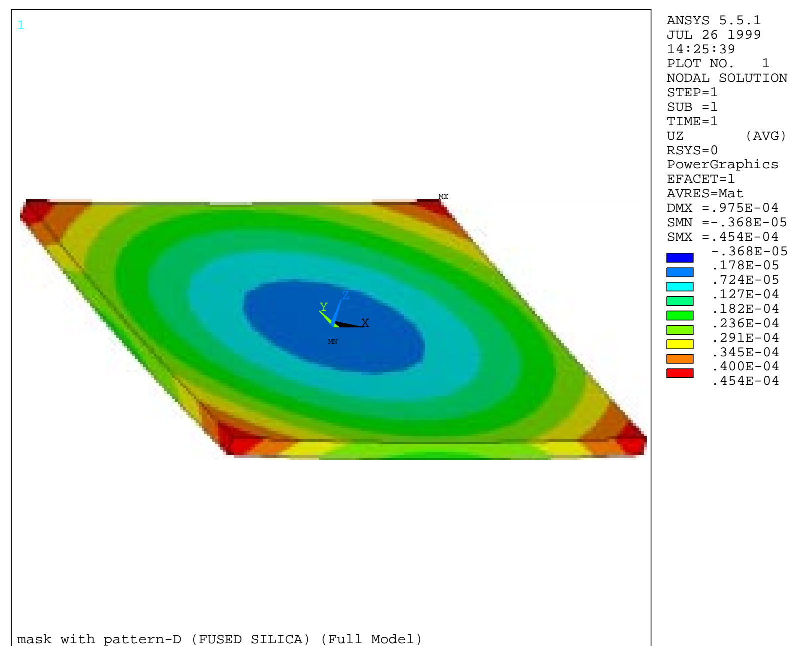

Figure 4.21 ANSYS® OPD distribution for SiO_2 result shown in Figure 3.23.

Figure 4.21 shows the OPD contour plot for the mask with pattern using the input parameters provided in Table 4.1 and the temperature contour is shown in Figure 3.23. It should be mentioned that the distortion is very much dependant on the mechanical boundary conditions.

4.3.2 Transient analysis

4.3.2.1 Preliminary run

The model is now used to predict the transient thermal distortion during full field exposure. The structural model uses the results from the ANSYS® thermal element result (solid 70) discussed in section 3.3.2 case number one, as input for ANSYS® structural element (solid 45) to obtain the distortion due to the thermal loading. The model parameters are the same as those given in Table 4.1 but the timing must be adjusted to be half second “light on” and half second “light off” to perform the duty cycle shown in Figure 3.30. Figure 4.22 shows the maximum in plane distortion (IPD) history in the pattern area for the preliminary run case. The corresponding thermal results are presented in section 3.3.2.1. Figure 4.23 shows the OPD contours for the quarter symmetry mask. The mechanical boundary condition in this case is such that the mask is clamped from the bottom surface at the two edges of the mask, as shown before in Figure 3.33.

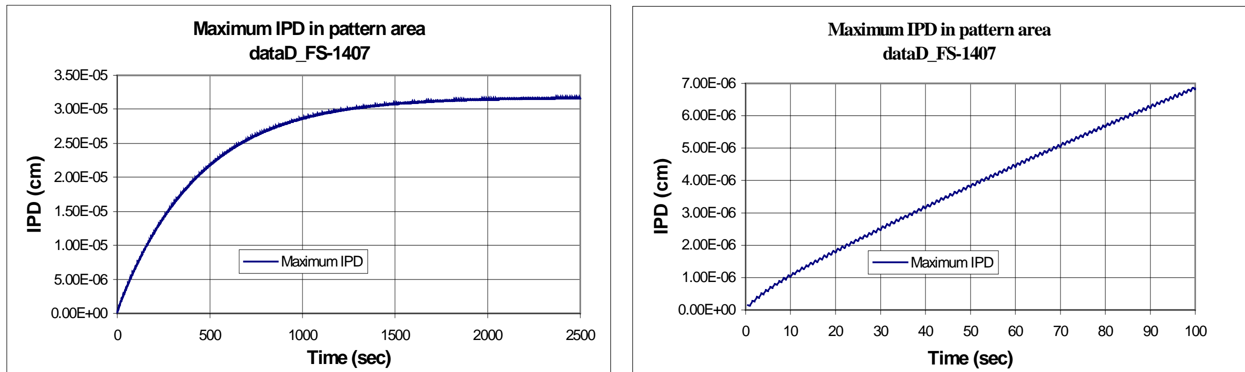

Figure 4.22 ANSYS® results for maximum IPD history for SiO_2 corresponding to Figure 3.31.

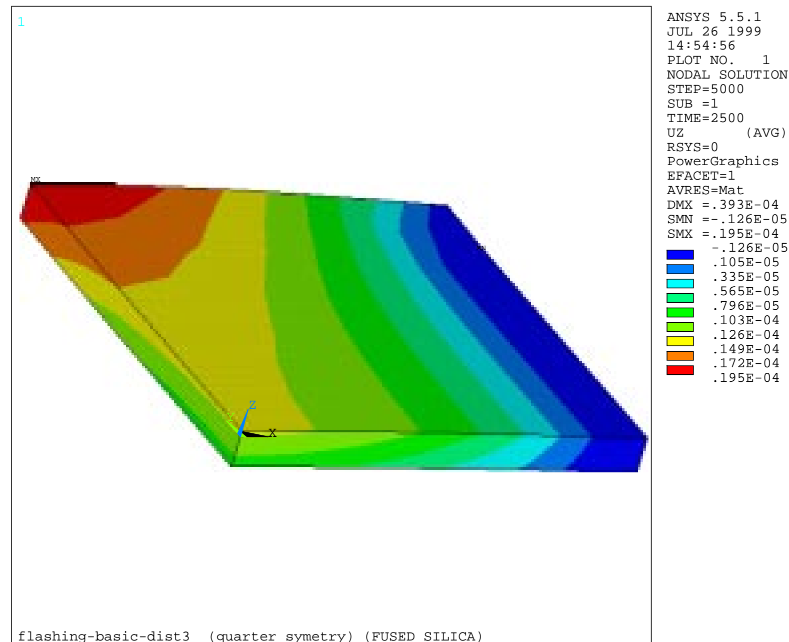

Figure 4.23 ANSYS® results for OPD contour plot for SiO_2 corresponding to Figure 3.32.

4.3.2.2 Simulating the actual duty cycle

The model is now used to predict the transient thermal distortion during full field exposure with the actual duty cycle shown in Figure 3.2. The thermal results represented in section 3.3.2.2 are used as input to the structural model to obtain the thermal distortion.

Figure 4.24 shows the contour plot for the y-direction displacement for a fused silica quarter symmetry model. The influence of the boundary condition can be seen as the y-direction displacement is zero along the right edge of the graph as all the nodes on the bottom surface are clamped from displacement as shown in Figure 3.35.

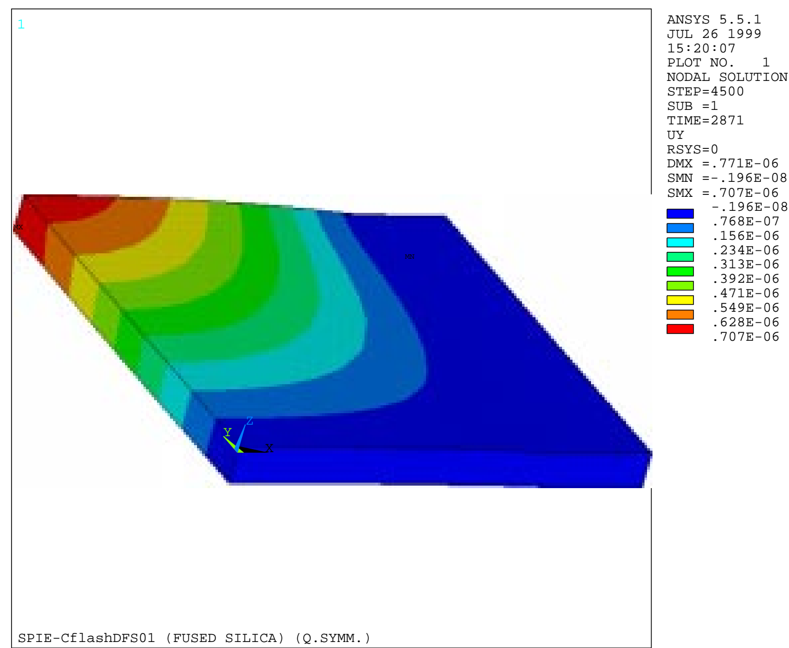

Figure 4.24 ANSYS® results for IPD contour plot for SiO2 corresponding to Figure 3.34.

The parameters for this case are given in Table 4.2, also schematic of the problem is given in Figure 3.35 [ref. 4.4].

Table 4.2. Input parameters for the flashing problem.

Dimensions	Outer sides length	15.24 cm
	Exposure area	10.0cm ×12.8cm
	Mask thickness δ	0.635 cm
Applied load	Lighting power	16.64 mW/cm^2
Pattern characteristics	Glass absorption coefficient	0.4% 1/cm
	Chrome absorptivity	50%
	Chrome coverage	90%
Heat transfer characteristics	Ambient temperature T_∞	300 K
	Top emissivity	0.9
	Bottom emissivity	0.5
	Top heat transfer coefficient	5e-4 W/ cm^2-K
	Bottom heat transfer coefficient	2.5e-4 W/ cm^2-K
Model parameters	Light applied duration	38 msec
	Flash delay	100 msec
	Wafer delay	15 sec
	Number of field per wafer	30
Material properties (Fused Silica)	Thermal conductivity k	0.0138 W/cm-K
	Density ρ	2202 E-6 g/cm^3
	Specific heat C	746 J/kg-K
	Young's modulus of elasticity E	72.6E5 N/ cm^2
	Poisson's ratio ν	0.164
	Thermal expansion coefficient α	0.51E-6 1/K

4.4 Summary

In this chapter, some ANSYS® structural test models were developed and checked with analytical solution in order to reach a high confident level in the structural modeling before simulating the actual full field exposure process to obtain the thermal distortion. Simple and complex problems were used to benchmark ANSYS® and a good agreement were found for all test cases. The thermal distortion during full field exposure was presented in this chapter for both fused silica and calcium fluoride material.

4.5 References

[4.1] T. Bloomstein, MIT Lincoln Laboratory, Private Communication.

[4.2] S. P. Timoshenko, "Theory of Elasticity," third edition, McGraw-Hill book company,1970

[4.3] H. Parkus, "Thermoelasticity," second revised and enlarged edition, Springer-Verlag, Wien New York, 1976

[4.4] J. Chang, A. Abdo, B. Kim, T. Bloomstein, R. Engelstad, E. Lovell, W. Beckman and J. Mitchell, "Thermomechanical Distortions of Advanced Optical Reticles during Exposure," Proceedings of the 1999 SPIE symposium on Emerging Lithography Technologies III, Vol. 3676, pp. 756-767, 1999.

Chapter Five
Thermal response during exposure – Scanning Exposure

5.1 Introduction

Scanning exposure process is another technique of pattern transfer from the mask to the wafer. It was first introduced to solve economic and handling problems of optical lithography with full field exposure technique. Few years ago, when optical lithography was extended to the 0.25 μm level using 248 nm wavelength light with a field size of 26 mm by 26 mm, full field exposure technique required an optical lens estimated to weigh 1800 pounds and cost over a million dollars (estimate from SVG Lithography System, Inc.). Both the extreme mass and cost of the lens resulted in stepper suppliers designing alternatives to full-field stepping with conventional lens designs. One of these alternatives was the scanning exposure technique [ref. 5.1].

The scanning exposure can be described, as a moving light beam of narrow width incident on the mask, which allows the pattern transfer to the stationary wafer. Figure 5.1 shows a schematic of the process from the mask side.

In the modeling of the scanning exposure problem, the difference from the full field exposure case is in the exposure area and the exposure timing. As it is practically impossible to simulate the scanning process as a strip of light moving over the mask as a continuum, two approaches are used to simulate this process. The first approach assumes

that the light strip is small enough that it could be simulated with a "one strip" moving with no overlap, i.e., the exposed area is equal to the strip area, and the light strip is shifting to the next position with the full strip width δ. Figure 5.2 illustrates the idea of the one strip model.

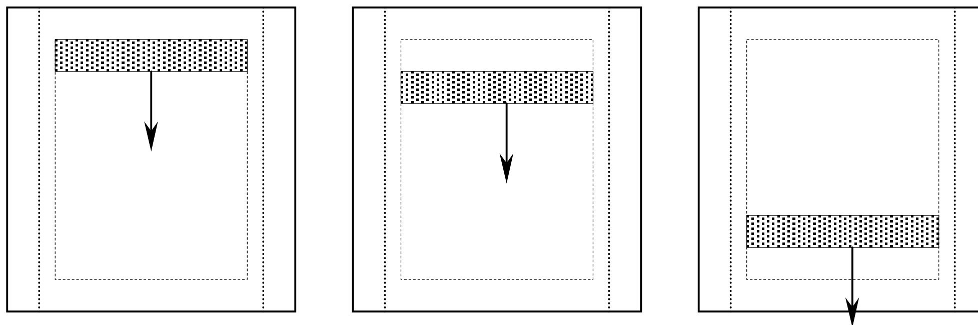

Figure 5.1 Schematic of the scanning process.

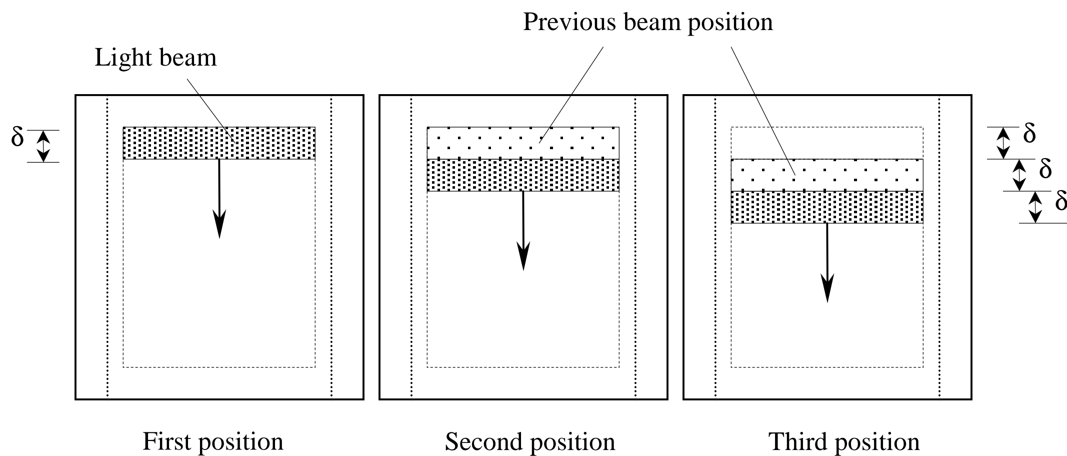

Figure 5.2 "One Strip" model schematic.

It is assumed in this modeling that the strip of light is exposed on the mask during a finite time period, calculated from the strip dimension and the mask speed of motion. This approach is sufficient when the strip width δ is small and the mask is moving fast so that the overlap of the light has a negligible effect on the final result. The second approach is

more accurate as it accounts for the overlap in the light beam. Figure 5.3 shows the schematic of the model, where the beam is assumed to be fully exposed over four steps from the start, each step representing a quarter of the light beam. When the full width is exposed, the light beam keeps overlapping with its quarter width until finishing the complete scan, i.e. the beam is moving forward by only its quarter width. If the width is divided to more than four quarters, this approaches better approximates the continuum

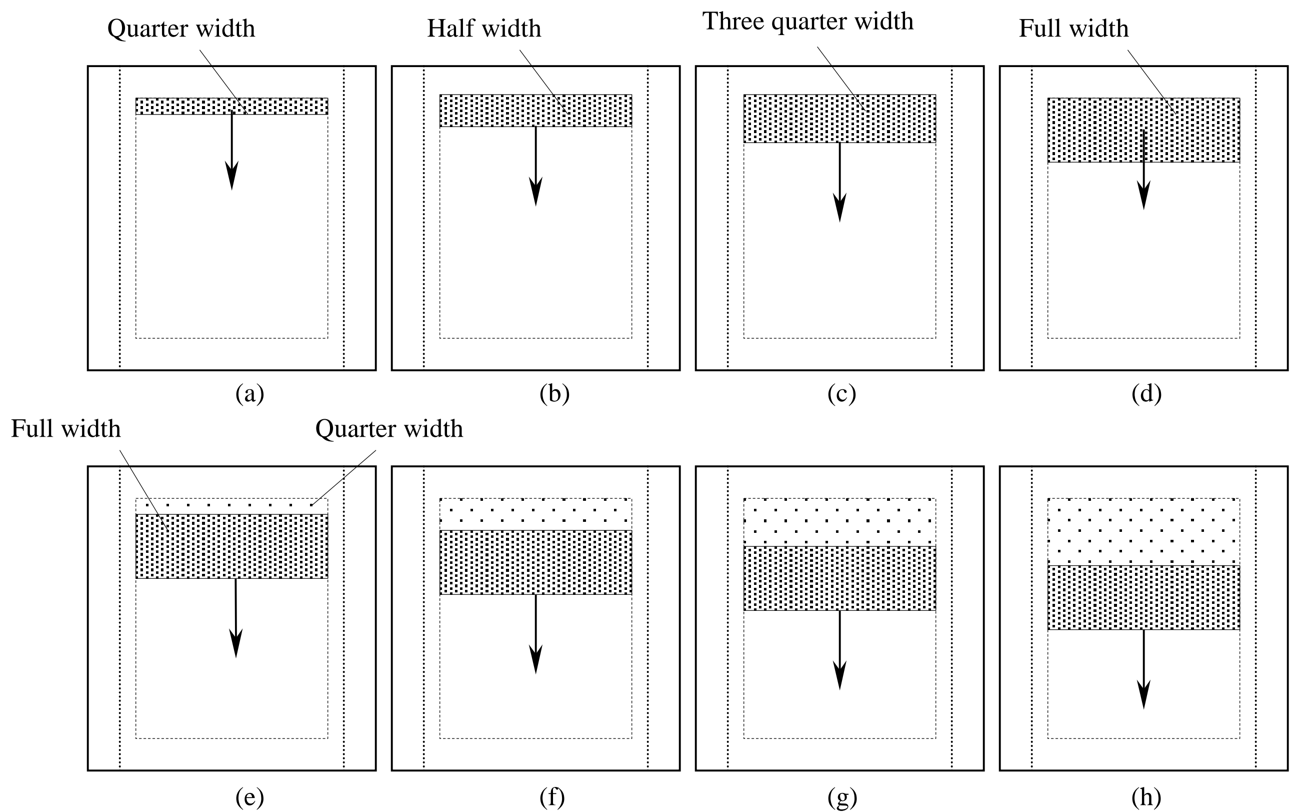

scanning process, but also it significantly increases the computational time.

Figure 5.3 “Overlapping Strip” model schematic.

The time needed in the exposure process for the “overlapping strip” model is calculated the same way as the “one strip” model, except that a parameter is introduced to the

equation, which is the fraction of the width of the beam which moves forward in the exposure.

5.2 One strip model

The "one strip" model is used as a preliminary test for the model as it takes less computational time. Figure 5.4 shows some of the scanning parameters, the exposure area is $W \times \delta$ where W is the light beam length (the exposure area width) and δ is the light beam width.

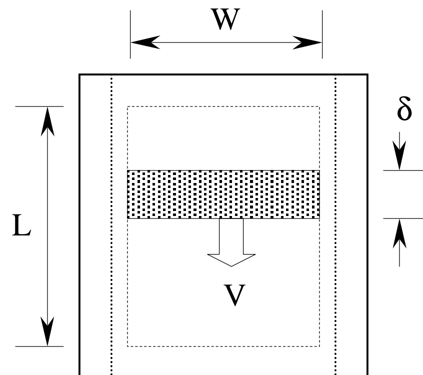

Figure 5.4 Scanning model parameters.

The time needed for finishing one scan is equal to L/V where L is the length of the exposure area shown in Figure 5.4 and V is the scanning velocity. The time needed for exposing one strip is calculated from the time needed to complete one scan (L/V), divided by the number of strips (n_strip $=L/\delta$) so that the time is δ/V. After completing one scan, the light was assumed to be "off" for a certain amount of time (scan delay time), then the light scans from the other direction (alternating direction). This process is repeated n_scan times, equal to the number of fields on the wafer surface. After that, the light

beam is "off" by a longer period of time (wafer delay time) which is needed to replace the wafer by a new blank one, starting the process over. The process is repeated until all the wafers (n_wafer) are exposed. Table 5.1 shows some of the parameters used for the modeling of the problem.

Table 5.1 Input parameters for the "one strip" scanning model.

Dimensions	Mask outer dimensions	14.9cm× 12.2cm
	Exposure area ($L \times W$)	12.8cm× 10.4cm
	Mask thickness	0.635 cm
Applied load	Lighting power	0.1 W/cm^2
Pattern characteristics	Glass absorption coefficient	0.4% 1/cm
	Chrome absorptivity	50%
	Chrome coverage	90%
Heat transfer characteristics	Ambient temperature T_∞	300 K
	Emissivity	0.9
	Top heat transfer coefficient	5e-4 W/ cm^2-K
	Bottom heat transfer coefficient	2.5e-4 W/ cm^2-K
Model parameters	Modeling method	One Strip
	Light beam width δ	0.5 cm
	Scan velocity V	200 mm/sec
	Scan delay	1 sec
	Wafer delay	10 sec
	Number of field/wafer (n_scan)	5 (test case)
	Number of wafers (n_wafer)	3 (test case)
Material properties (Fused Silica)	Thermal conductivity k	0.0138 W/cm-K
	Density ρ	2202 E-6 g/cm^3
	Specific heat C	746 J/kg-K

The boundary conditions for this simulation are convection from the top and bottom and radiation from all the free surfaces. For presenting ANSYS® results for the "one strip" scanning model, ten nodes along the line of symmetry on the bottom surface of the mask (the patterned side) are chosen to represent the temperature response with time. The

temperature of the nodes on the bottom surface is much higher than the nodes on the same locations but on the top surface, as the chrome pattern is located on the bottom surface only. Figure 5.5 shows the location of the nodes for which the results are presented.

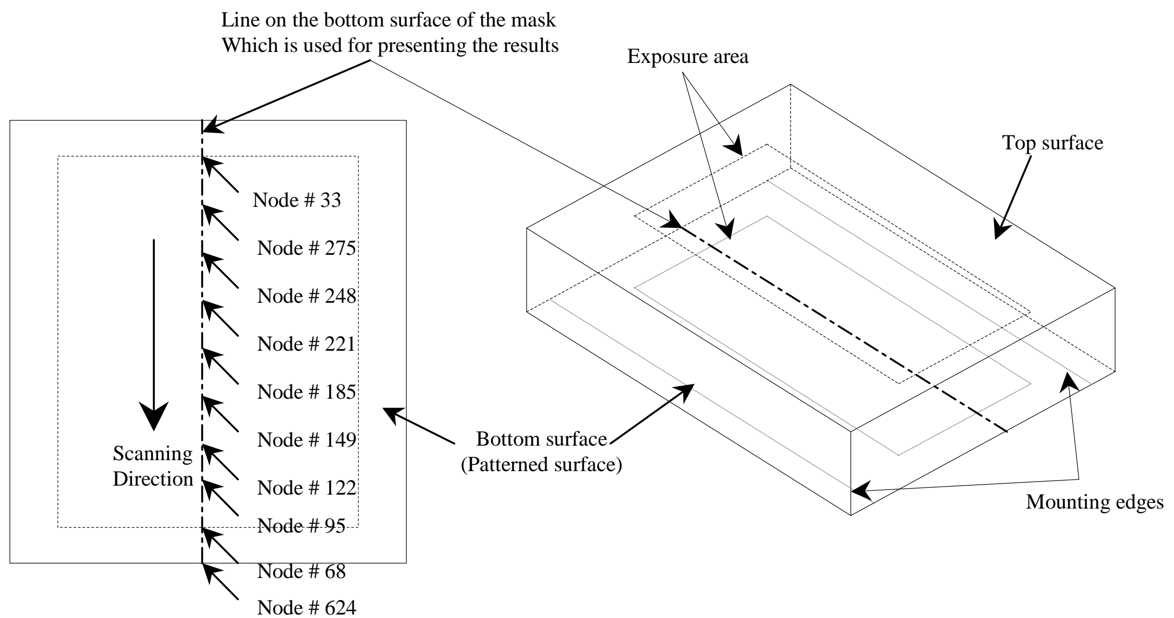

Figure 5.5 Relative position of the nodes used for presenting the results.

Figure 5.6 presents ANSYS® thermal results for the nodes shown in Figure 5.5. Two time ranges were presented in Figure 5.6, the short time range, for the first 3 seconds and a longer time range, for the first 60 seconds.

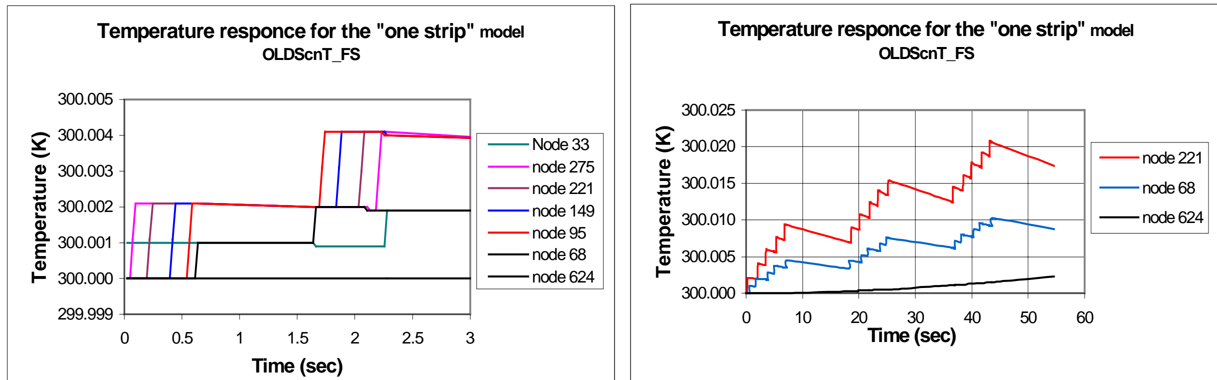

Figure 5.6 ANSYS® results for temperature response, using the parameters in Table 5.1.

Since the scanning method alternates direction, the temperature rises first for node 33, then 275 and so on till nodes 95 and 68, (one scan is completed) and then the temperature rises for nodes 68 (because the alternating direction of the beam) then node 95 till nodes 275 and 33. The temperature rise of nodes 33 and 68 are one half of the temperature rise of all the other nodes in the exposure area, since they are on the edge of the exposure area as shown in Figure 5.5. Since node 624 is outside the patterned area, it can be seen in Figure 5.6 that its temperature response is much lower than the other nodes. Figure 5.7 shows the temperature contours on the patterned (back) surface of the mask for the first light beam application i.e., first step.

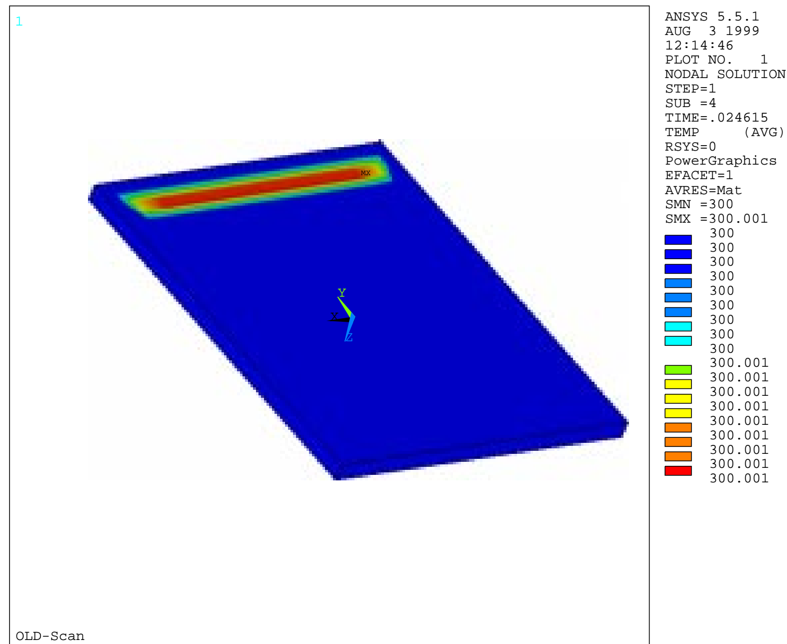

Figure 5.7 ANSYS® temperature contour for the first step of scanning.

To show any significant temperature contours, the contour plan view must be taken from the backside. The temperature rise at this step is so low that no temperature change can be seen on the top surface of the mask.

Figures 5.8 and 5.9 show the temperature contours as the scanning light beam is progressing downward in the scanning direction shown in Figure 5.5.

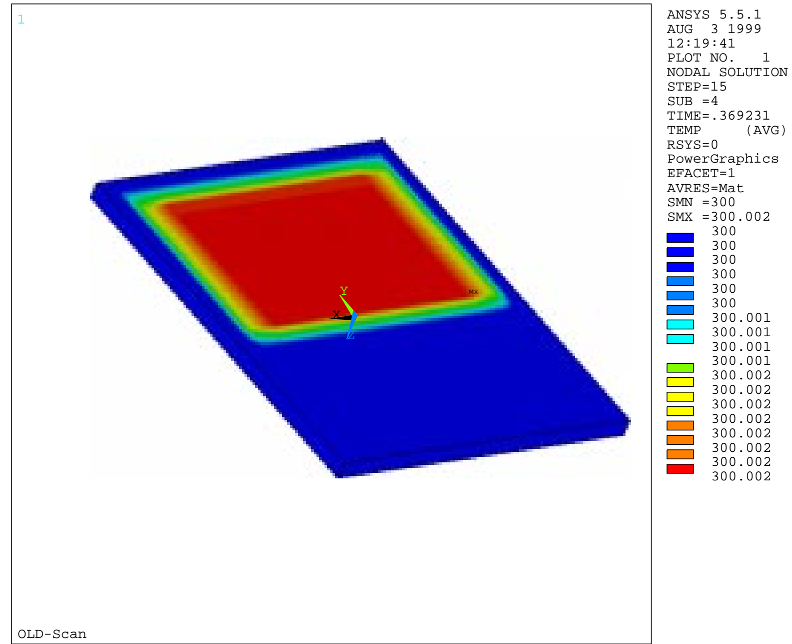

Figure 5.8 ANSYS® temperature contour when the beam in the 15th position.

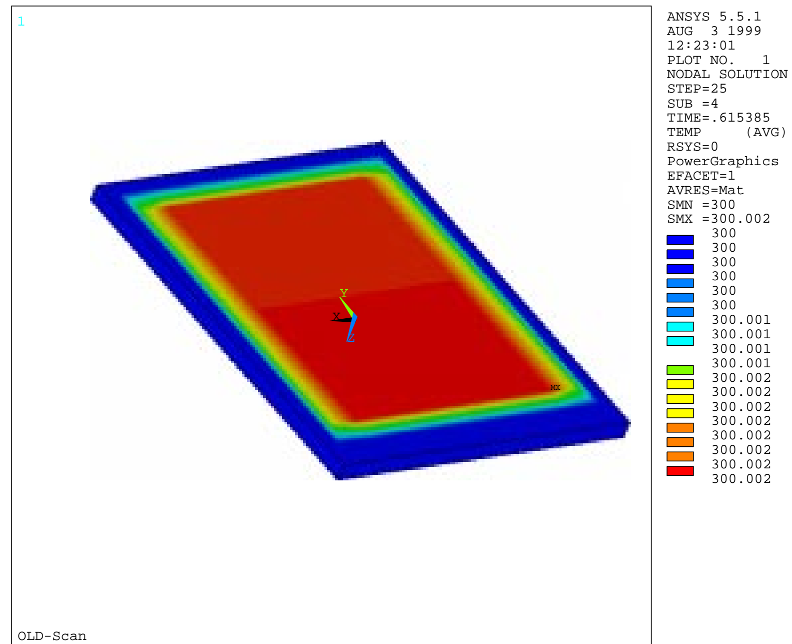

Figure 5.9 ANSYS® temperature contour when the beam in the 25th position.

Figure 5.10 shows ANSYS® temperature contours after completing of one scan and one scan delay time. An interesting observation is that the temperature is very uniform in the exposure area as if the energy input has been applied over the entire exposure area.

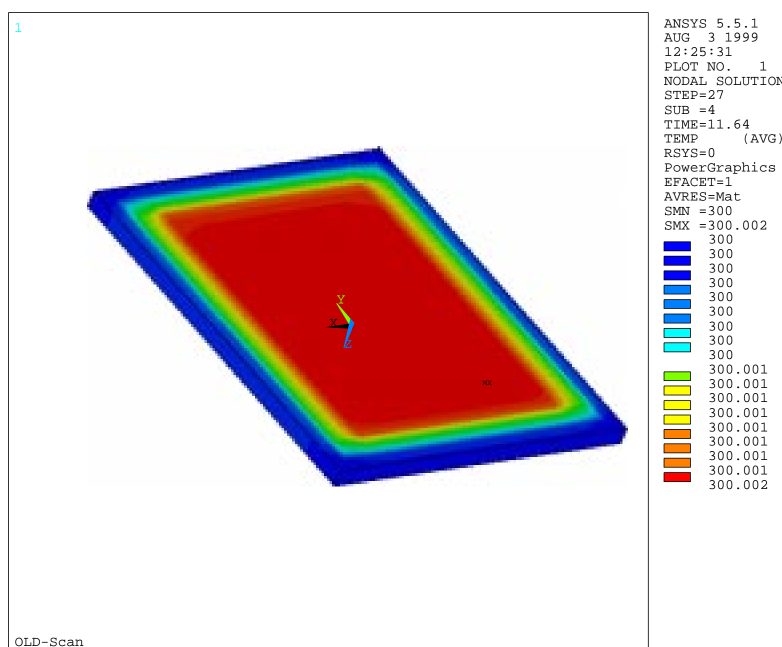

Figure 5.10 ANSYS® temperature contour after the scan delay time.

The results of this preliminary study are useful for building more complicated model.

5.3 Overlapping strip model

After getting confidence in the modeling using the "one strip" model, a more accurate model "the overlapping strip model" is used to simulate the scanning process. The "overlapping strip" model requires much longer time for the simulation as the number of

thermal loading steps are significantly increased. Table 5.2 shows the input parameters used in the modeling.

Table 5.2 Input parameters for the "overlapping strip" scanning model.

Dimensions	Mask outer dimensions	15.24cm (Square)
	Exposure area ($L \times W$)	12.8cm× 10.0cm
	Mask thickness	0.635 cm
Applied load	Lighting power	0.1 W/cm^2
Pattern characteristics	Glass absorption coefficient	0.4% 1/cm
	Chrome absorptivity	50%
	Chrome coverage	90%
Heat transfer characteristics	Ambient temperature T_∞	300 K
	Top surface Emissivity	0.9
	Bottom surface Emissivity	0.5
	Top heat transfer coefficient	15e-4 W/ cm^2-K
	Bottom heat transfer coefficient	4e-4 W/ cm^2-K
Model parameters	Modeling method	Overlapping Strip
	Light beam width δ	21.1 mm
	Scan velocity V	400 mm/sec
	Scan delay	0.1 sec
	Wafer delay	15 sec
	Number of field/wafer (n_scan)	30
	Number of wafers (n_wafer)	3 (test case)
Material properties (Fused Silica)	Thermal conductivity k	0.0138 W/cm-K
	Density ρ	2202 E-6 g/cm^3
	Specific heat C	746 J/kg-K

The thermal boundary conditions for this model included convection and radiation from the top and the bottom surfaces (with different heat transfer coefficients and emissivities to account for the pellicle and the chrome layer) and conduction to the mounting mechanism. As the thermal mass of the mounting mechanism was assumed to be much larger than that of the mask, the temperature was assumed to be fixed at the ambient temperature at the common region of contact.

As the full light beam width (δ) is around 20 mm, and the exposure area length is 128 mm then 6.4 beams will be needed to complete the full length. To avoid the unnecessary complication of non-integer number of beams the beam width was assumed to be 21.1 mm which means six beams (*ney*) are needed to scan the mask. To apply the overlapping idea, the beam width has to be refined to the desired number. For quarter width beam, the refinement number (*r*) must be four. Thus, the number of steps (n_{steps}) needed to complete one scan is calculated as:

$$n_{steps} = [ney * r + (r - 1)] \tag{5.1}$$

The time needed for one step is similar to that calculated in the "one strip" model but divided by the refinement number (*r*). According to equation 5.1 and the previous numbers, the number of steps needed to complete one scan is 27 steps, adding one step for delay time between scans, then 28 steps are needed for each scan. For 30 scans per wafer, 840 steps are needed. Adding one step for the delay between wafers, then 841 steps are needed for completing one wafer. Each step in the simulation typically uses at least 4 sub-steps and for the thermal simulations the temperature must be solved for at all nodes. The number of nodes must be reasonably high because the same mesh will be used in the structural simulation, which must be fine enough to get good results. To reduce the number of nodes a half symmetry model was used in the simulation. This transient analysis results in a very long computational times and large computer storage files are needed to store all this data.

Figure 5.11 shows a schematic of the geometry used in the simulation (half symmetry model). The figure shows the positions of the nodes, which are used for representing the simulation results. Four elements in the depth are used to have a sufficient fine mesh for the structural analysis. Figure 5.12 shows the temperature response for different nodes from the ANSYS® simulation using the parameters in Table 5.2. The simulation results given in Figure 5.12 show the temperature variation with the time for the nodes shown in Figure 5.11. The temperature is always higher on the chrome-patterned surface (bottom surface) than on the unpatterned surface (top surface) and the maximum temperature always occurs at node 179. The time delay time can be shown in the figure as the temperature drops due to heat loss.

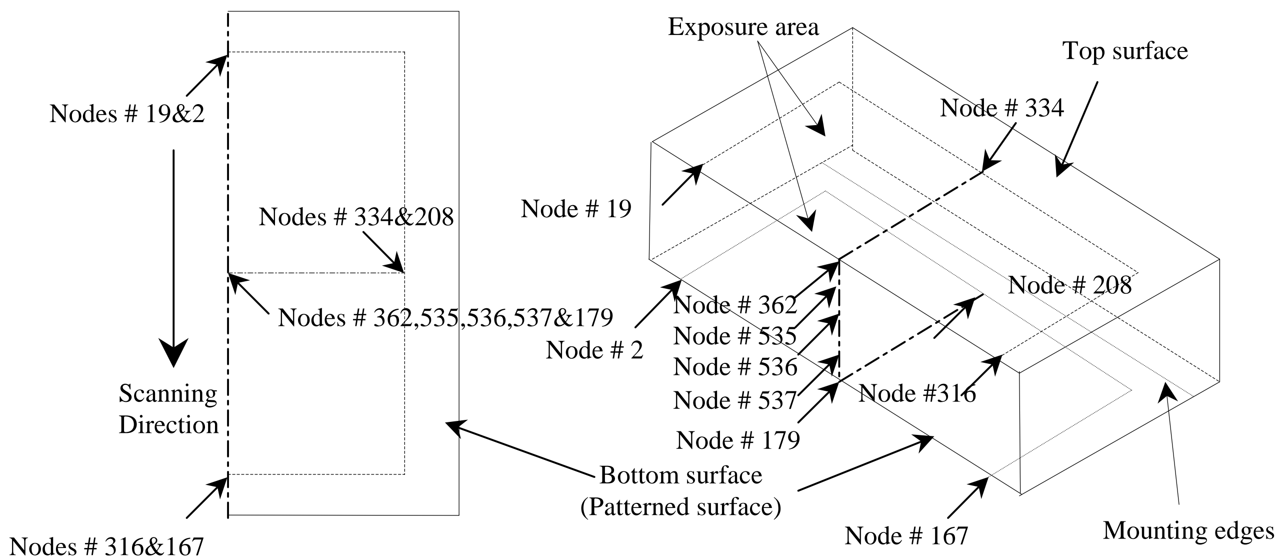

Figure 5.11 Geometry used in the finite element simulation.

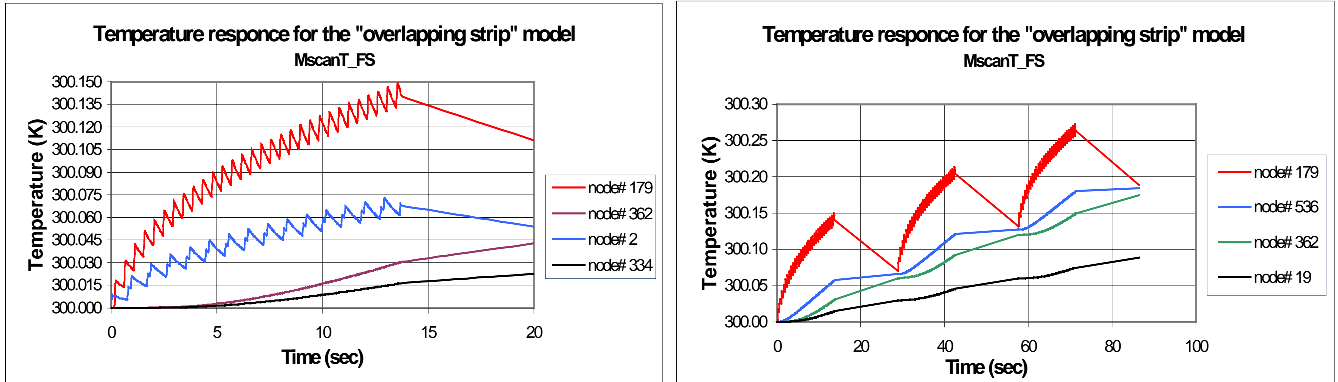

Figure 5.12 Short and long term temperature response of the optical mask.

Figure 5.13 shows ANSYS® contour plot result (half symmetry model) for the first step, where the beam position is in the first scanning position on the mask surface. The temperature contour of the last step of the first scan is presented in Figure 5.14.

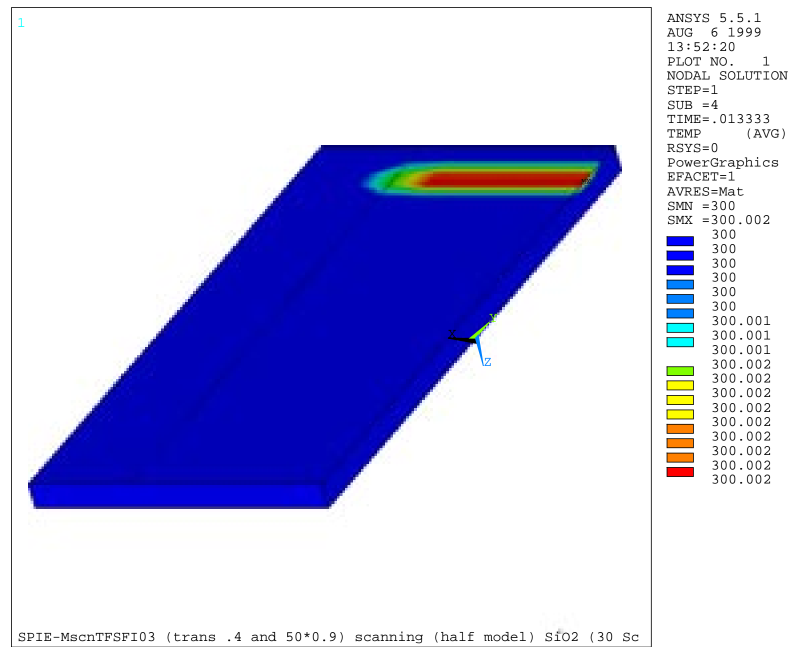

Figure 5.13 ANSYS® temperature contour for the first beam position.

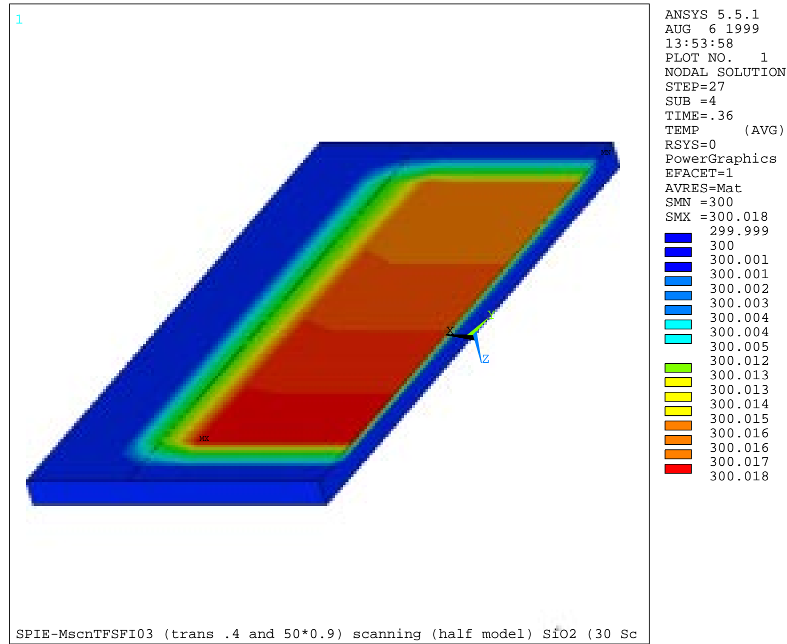

Figure 5.14 ANSYS® temperature contour for the last beam position in the first scan.

The temperature contour plot for the first step in the last scan is shown in Figure 5.15, the light beam heating effect can be noticed from the hot spot at the lower portion of the mask. The input parameters used for this simulation are given in Table 5.2. Figure 5.16 shows the temperature distribution at the last step, just after the wafer delay time.

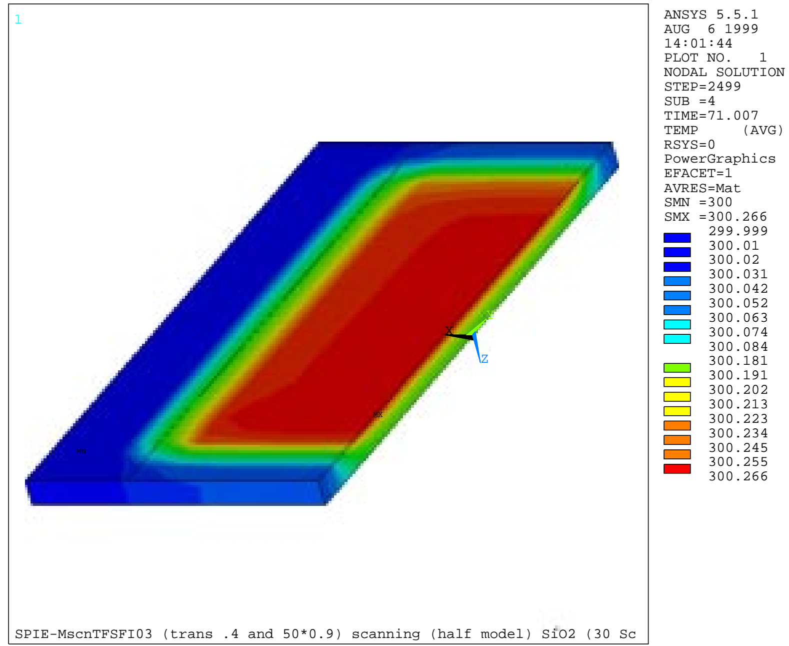

Figure 5.15 ANSYS® temperature contour for the first beam position in the last scan.

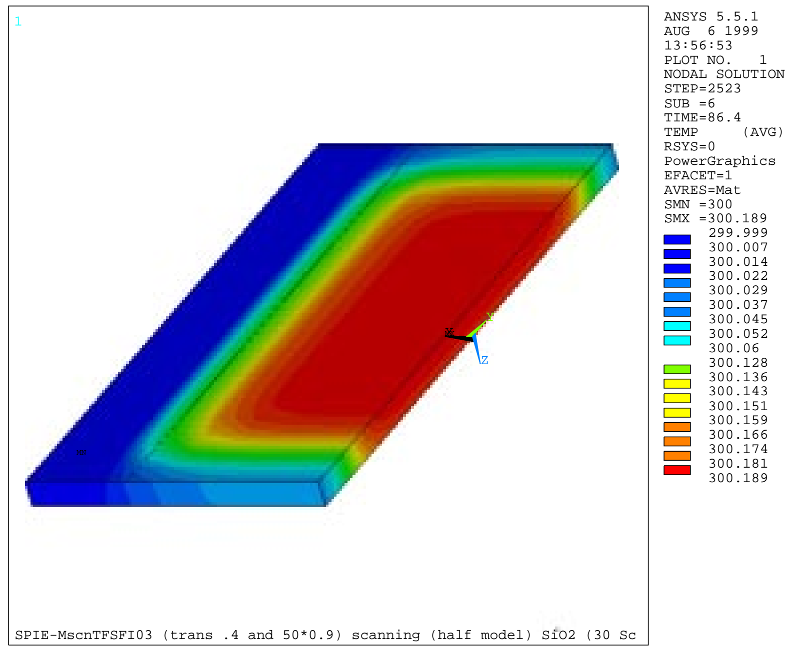

Figure 5.16 ANSYS® temperature contour for the last step.

5.4 Scanning modeling conclusion

The most important conclusion which can be deduced from the results of two different scanning methods presented in this chapter is that even though the thermal loading is not uniform but the final temperature contours after each scan look very uniform. The scanning simulations using ANSYS® takes very much computational time and very much computational storage spacing, the final temperature contour is as if a uniform heating was used, Figure 5.16 is a very clear example of that.

Because there is no other alternative for simulating the scanning process as a transient problem, and because the mesh must be fine to insure good results for the structural modeling (the thermal model does not need such a fine mesh), an equivalent heating model must be considered. This approximation will be discussed in a later chapter [ref. 5.2].

5.5 References

[5.1] P. Rai-Choudhury, "Microlithography, Micromachining, and Microfabrication", Volume 1: Microlithography, SPIE Optical Engineering Press, 1997.

[5.?] J. Chang, A. Abdo, B. Kim, T. Bloomstein, R. Engelstad, E. Lovell, W. Beckman and J. Mitchell, "Thermomechanical Distortions of Advanced Optical Reticles during Exposure," Proceedings of the 1999 SPIE symposium on Emerging Lithography Technologies III, Vol. 3676, pp. 756-767, 1999.

Chapter Six
Thermal distortion during exposure – Scanning Exposure

6.1 Introduction

In this chapter the thermal distortion resulting from the scanning exposure is presented. The structural result is presented for both scanning techniques previously presented in chapter five i.e., the "one strip" scanning model and the "overlapping strip" scanning model. The results from the thermal response are used as input in the structural model to get the thermal distortion.

6.2 One strip model

For the "one strip" model previously described in section 5.2, the input parameters for the structural model are the same given in Table 5.1. Table 6.1 represents a summary of the structural material properties of the fused silica used in the simulation.

The mechanical boundary conditions for this model is such that the central node is completely clamped (fixed from translation) in the three directions. With this boundary condition the mask can expand freely in all directions. The largest in-plane distortion (IPD) in the patterned area will be the *y*-direction translation component of the middle node on the short side of the mask (node number 33 in Figure 5.5). Figure 6.1 shows

ANSYS® contour plot for the *y*-direction translation and Figure 6.2 shows the *y*-direction translation of node 33 with the time.

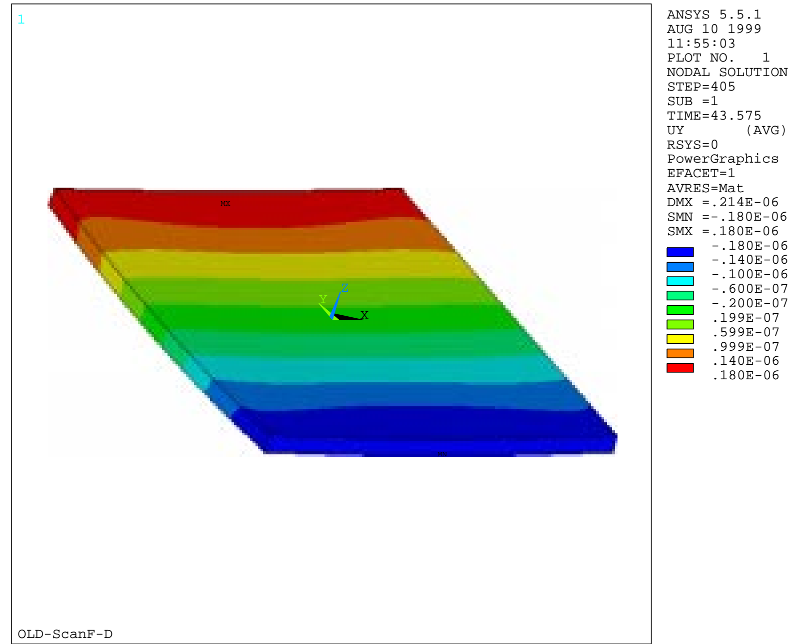

Figure 6.1 ANSYS® IPD contour plot distribution for the “one strip” model.

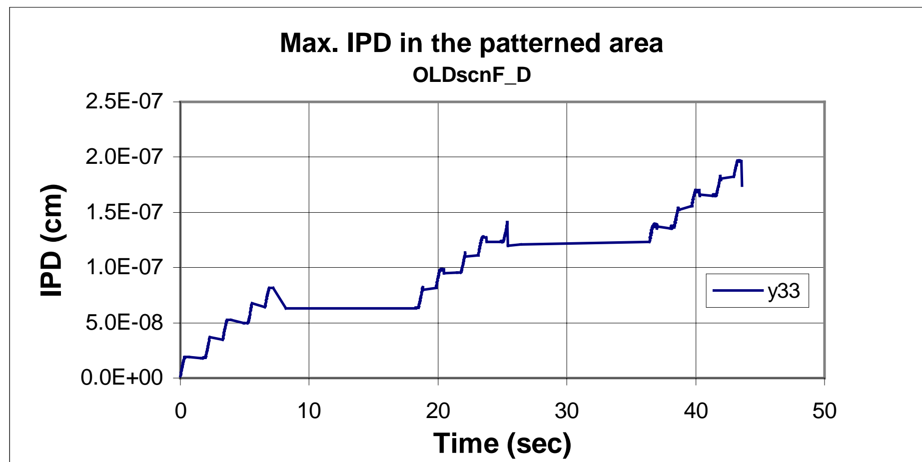

Figure 6.2 Maximum y-direction translation in the patterned area as a function of time.

Table 6.1 Structural properties for the "one strip" scanning model structural model.

Material properties (Fused Silica)	Young's modulus of elasticity E	72.6E5 N/ cm^2
	Poisson's ratio ν	0.164
	Thermal expansion coefficient α	0.51E-6 1/K

6.3 Overlapping strip model

The ANSYS® thermal distortion solution for the case of the "overlapping strip" scanning model corresponds to the thermal results presented in section 5.3. The input parameters are the same given in Table 5.2 and the structural material properties are the same given in Table 6.1 as fused silica is the same mask material used in this model. The mechanical boundary condition is completely different than that in the "one strip" scanning model as it was assumed that the mask is clamped on the bottom surface (chrome patterned surface) along two sides as shown in Figure 3.34. This mechanical boundary condition allows the use of a half symmetry in both the structural analysis and the thermal analysis. The maximum IPD in the patterned area is always located in the same place, on the axis of symmetry and on the edge of the patterned area (node number 2 in Figure 5.11). Figure 6.3 shows the y-direction translation for node number 2 as a function of the time.

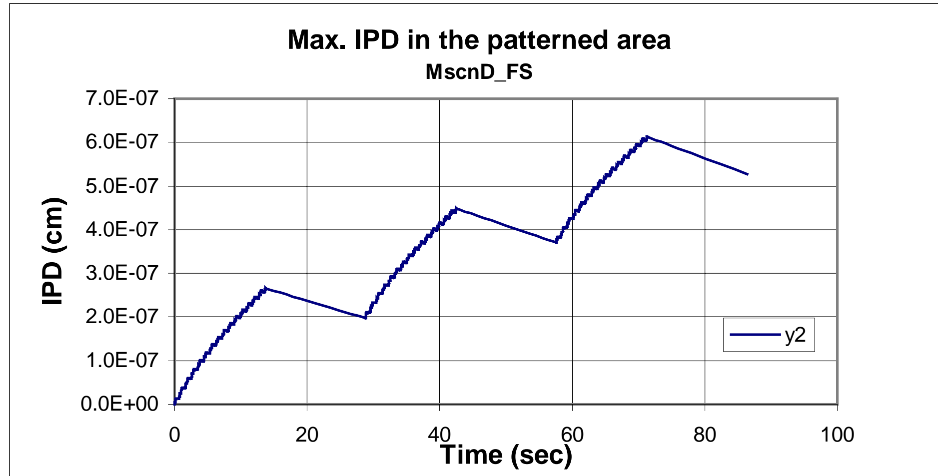

Figure 6.3 Maximum y-direction translation in the patterned area as a function of the time.

Figure 6.4 shows ANSYS® IPD contour plot distribution for the half symmetry model used for modeling the "overlapping strip" scanning model.

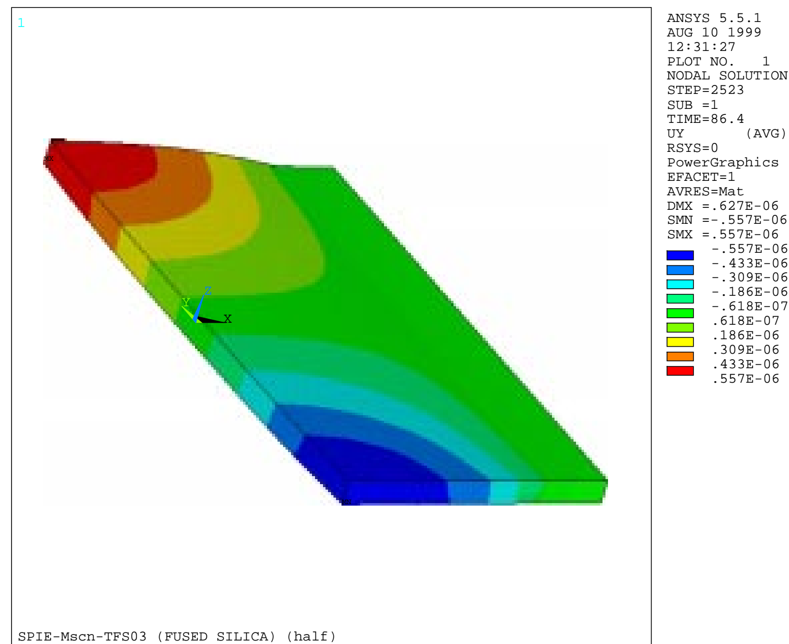

Figure 6.4 ANSYS® IPD contour plot distribution for the "overlapping strip" model.

6.4 Structural modeling summery

In this chapter, ANSYS® structural modeling results were presented for the thermal models developed in the previous chapter. As mentioned at the end of the previous chapter the temperature contours for the scanning model are similar to the temperature contours of a uniform heating model. From Figures 6.1 and 6.4, the contour plots of the IPD, from their symmetry, one can conclude that a uniform heating with quarter symmetry model may lead to the same distortion result [ref. 6.1].

6.5 References

[6.1] J. Chang, A. Abdo, B. Kim, T. Bloomstein, R. Engelstad, E. Lovell, W. Beckman and J. Mitchell, "Thermomechanical Distortions of Advanced Optical Reticles during Exposure," Proceedings of the 1999 SPIE symposium on Emerging Lithography Technologies III, Vol. 3676, pp. 756-767, 1999.

Chapter Seven
An averaging technique to simulate the thermal response during the scanning and full field exposure processes

7.1 Introduction

It was demonstrated in chapters three and five that during scanning exposure the temperature contours and the IPD contours are very uniform at the end of each scan. This means that an equivalent model, where the full exposure area is uniformly illuminated (flashed), may leads to acceptable results for the scanning exposure simulations.

In this chapter an equivalent modeling technique is developed and used to predict the temperature response of an optical mask during both scanning and full field exposures. The motivation for developing of such equivalent models is to reduce the very long computational time required for simulating the actual processes presented in chapters three and five. The equivalent model used for simulating the thermal response during scanning exposure is the same model used in chapter three to simulate the full field exposure i.e., the Thermal Detailed-Flashing Model (TDFM) with an equivalent incident light power and equivalent timing. Results from that equivalent model i.e., the TDFM are compared with the Thermal Detailed-Scanning Model (TDSM) for some test cases.

Despite the fact that the TDFM does not require as much computational time as the TDSM and as the average flashing technique is a good approximation to the scanning process, it can be used also for the full field exposure simulation by developing another equivalent model i.e., the Thermal Equivalent-Flashing Model TEFM. After confirming that the averaging technique is sufficiently accurate, both the TDFM (with equivalent parameters) and the TEFM replace the TDSM and the TDFM respectively to reduce the computational time required for simulating the actual exposure processes.

7.2 Testing the equivalent model

In this section, a test run is used to verify the equivalent modeling using the TDSM. The basic idea is to approximate the detailed scanning process used in the TDSM by a full field flash process simulated in the TDFM. The input parameters differ slightly from the actual scanning process but these runs are used only to verify the equivalent model so an exact parameter match is not needed. A half symmetry model is used and the mesh is constructed to be fine enough to make judgement about the suitability of the model. Table 7.1 presents a summary of the ANSYS® input parameters used for the simulations.

As shown in Figure 7.1, three numbers are needed for this approximation. The first number is the equivalent power of the light beam ($q''_{equivalent}$) to be used in the TDFM. The second and third numbers are the equivalent timing for the scanning process, i.e., how much time the equivalent flashing light in the TDFM must be "on" (τ_{on}) and how much time it must be "off" (τ_{off}) as shown in Figure 7.1. The amount of energy input in

the TDFM is calculated first. Equation 7.1 calculates the amount of energy (E) input to the mask for completing one wafer.

Table 7.1 Input parameters for the scanning test case.

Dimensions	Outer sides length	15.24 cm
	Exposure sides length	13.2 cm
	Mask thickness δ	0.635 cm
Applied load	Lighting power	0.1 W/cm^2
Pattern characteristics	Glass absorption coefficient	0.4% 1/cm
	Chrome absorptivity	50%
	Chrome coverage	90%
Heat transfer characteristics	Ambient temperature T_∞	300 K
	Emissivity ε	0.9
	Top heat transfer coefficient	5e-4 W/ cm^2-K
	Bottom heat transfer coefficient	2.5e-4 W/ cm^2-K
Model parameters	Modeling method	One Strip
	Light beam width δ	22 mm
	Scan velocity V	200 mm/sec
	Scan delay	1 sec
	Wafer delay	10 sec
	Number of field/wafer (n_scan)	5 (test case)
	Number of wafers (n_wafer)	10 (test case)
Material properties	Thermal conductivity k	0.0138 W/cm-K
	Specific heat C	746 J/kg-K

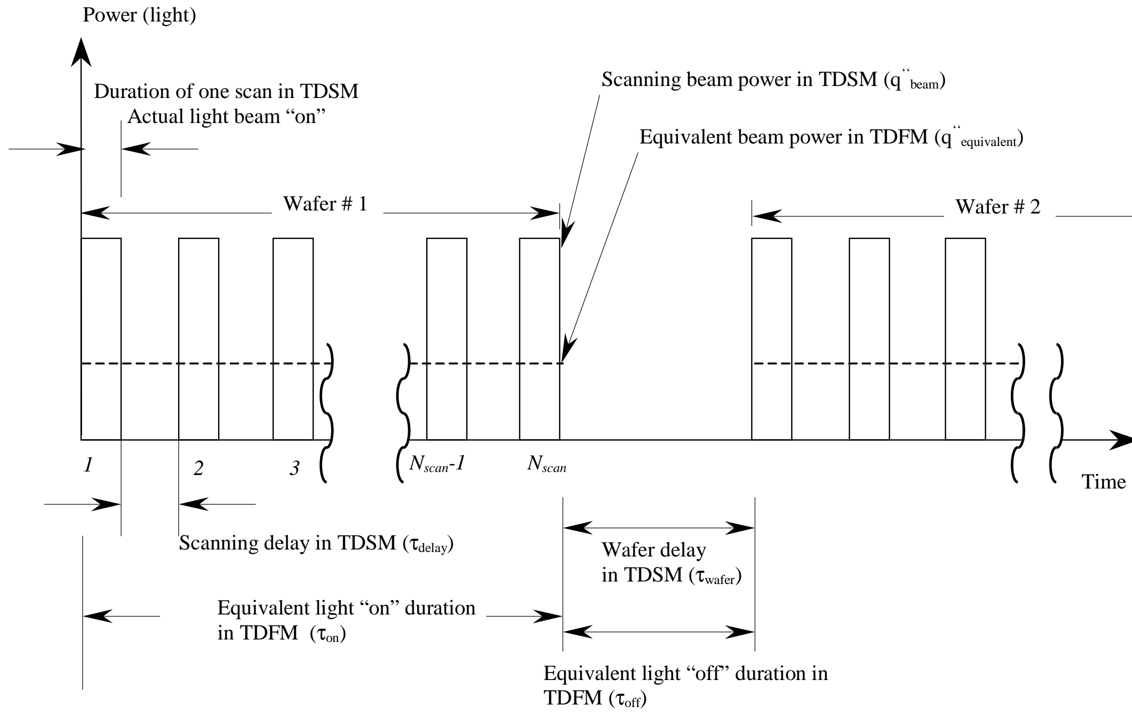

Figure 7.1 Schematic showing the parameters of the averaging technique TDFM Vs the detailed simulation TDSM.

$$E = q''_{beam} A_{beam} \tau_{strip} N_{strips} N_{scan} \tag{7.1}$$

Where q''_{beam} is the heat flux from the light beam, A_{beam} is the light beam area, τ_{strip} is the time needed for exposing one strip, N_{strips} is the number of strips per scan and N_{scan} is the number of scans per wafer. Dividing this amount of energy by the total exposure area, A_{exposure} defined by equation 7.2, and by the equivalent time where the equivalent light will be "on" which is τ_{on} defined by equation 7.3, leads to the equivalent heat flux $q''_{\text{equivalent}}$.

$$A_{exposure} = A_{beam} N_{strips} \tag{7.2}$$

$$\tau_{on} = \tau_{strip} N_{strips} N_{scan} + \tau_{delay} (N_{scan} - 1) \tag{7.3}$$

$$q''_{equivalent} = \frac{E}{(A_{exposure} \tau_{on})} = \frac{h_{beam} N_{scan} \tau_{strip}}{[\tau_{strip} N_{strip} N_{scan} + \tau_{delay} (N_{scan} - 1)]} \tag{7.4}$$

The TDFM averages all the scanning process for completing one wafer to only one full field exposure process. The equivalent light "off" time can be calculated from equation 7.5.

$$\tau_{off} = \tau_{delay} + \tau_{wafer} \tag{7.5}$$

The times τ_{delay} and τ_{wafer} are the scan delay and wafer delay times given in Table 7.1 and illustrated in Figure 7.1. A summary of the input parameters for TDFM using ANSYS® is given in Table 7.2.

Figure 7.2 represents the temperature contour from an ANSYS® simulation for the scanning exposure using TDSM at the end of the last scanning step in the test problem. The thermal boundary conditions for this test are such that heat losses by convection from top and bottom have different heat transfer coefficients. Also, radiation heat loss is assumed from all the free surfaces. The thermal model includes three-dimensional heat conduction but no mounting effects were included in this test problem. These boundary conditions are used for both detailed scanning TDSM and equivalent scanning TESM.

Table 7.2 Input parameters for the equivalent scanning simulation.

Dimensions	Outer sides length	15.24 cm
	Exposure sides length	13.2 cm
	Mask thickness δ	0.635 cm
Applied load	Equivalent lighting power	Equation 7.4
Pattern characteristics	Glass absorption coefficient	0.4% /cm
	Chrome absorptivity	50%
	Chrome coverage	90%
Heat transfer characteristics	Ambient temperature T_∞	300 K
	Top emissivity	0.9
	Bottom emissivity	0.5
	Top heat transfer coefficient	5e-4 W/ cm^2-K
	Bottom heat transfer coefficient	2.5e-4 W/ cm^2-K
Model parameters	Modeling method	Flashing
	Light applied duration (τ_{on})	Equation 7.3
	Flash delay (τ_{off})	Equation 7.5
Material properties (Fused Silica)	Thermal conductivity k	0.0138 W/cm-K
	Density ρ	2202 E-6 g/cm^3
	Specific heat C	746 J/kg-K

Figure 7.3 shows the temperature contours for the equivalent model using the TDFM model. Figure 7.4 shows the temperature contours on the back surface (chrome patterned surface) for the first step of scanning using the TDSM. The approximate width of the light beam is clearly evident.

Comparing Figures 7.2 and 7.3, it can be seen that both modeling techniques give the same temperature distribution at the last step.

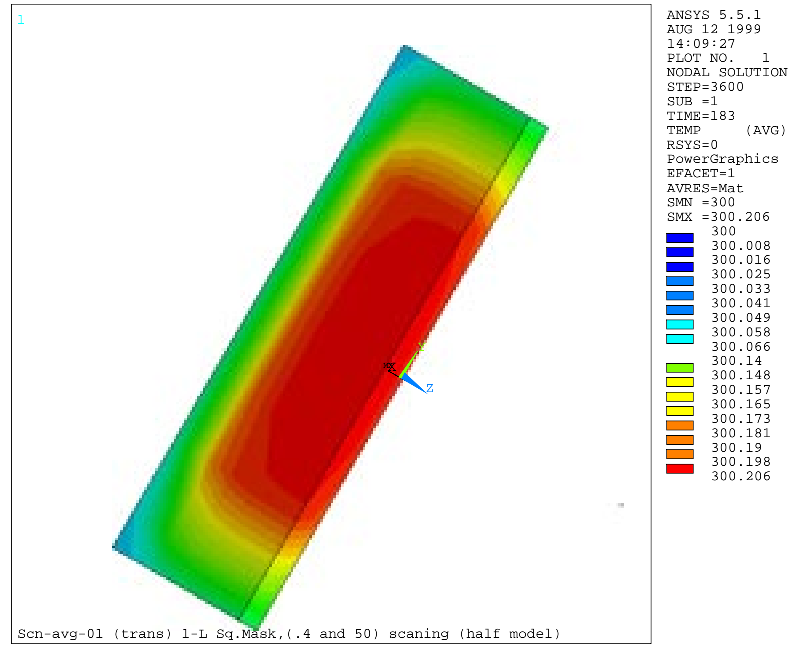

Figure 7.2 temperature contour for the last step in scanning using the TDSM.

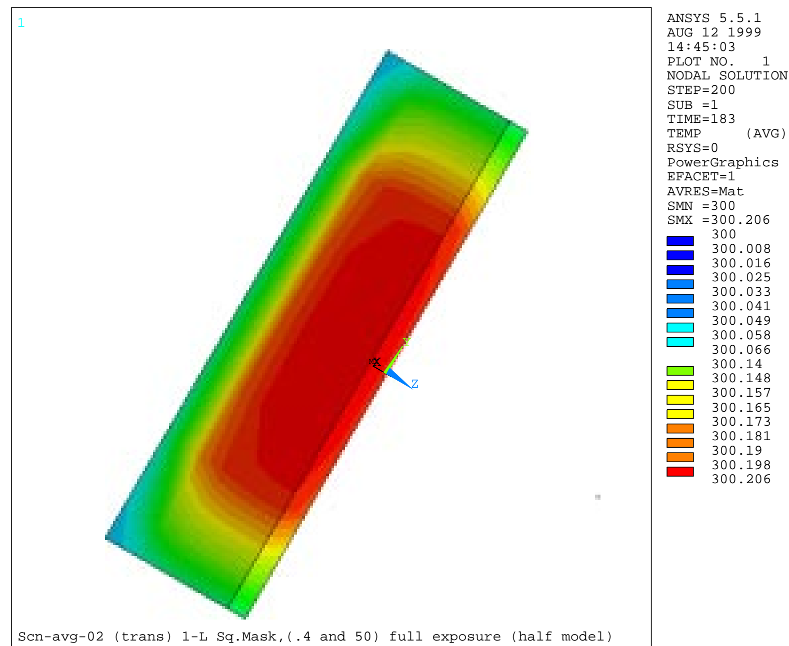

Figure 7.3 temperature contour for the last step in the scanning using the TDFM.

Figure 7.4 temperature contour for the first step in scanning using the TDSM.

Figure 7.5 Temperature history during scanning using TDSM (from highest to lowest temperature 143, 1, 198, 53, 13, 237).

In order to compare both simulation methods i.e., detailed scanning using TDSM and equivalent scanning using TESM, Figure 7.5 and 7.6 were prepared to show the temperature behavior for ten different nodes on the mask; excellent agreement was found.

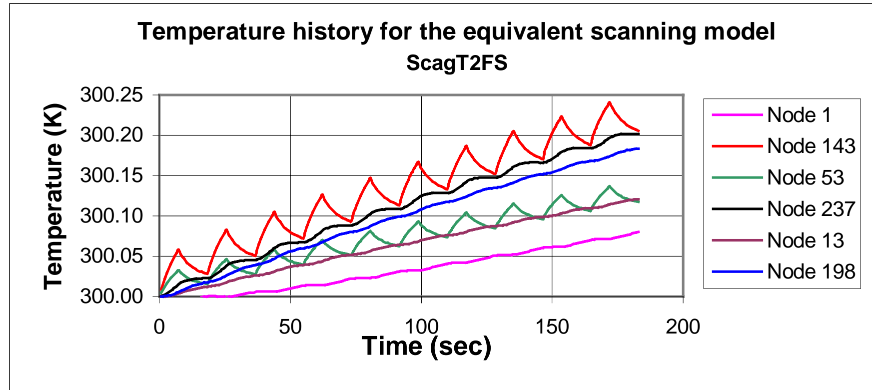

Figure 7.6 Temperature history during scanning using the equivalent-scanning model TDFM (from highest to lowest temperature 143, 1, 198, 53, 13, 237).

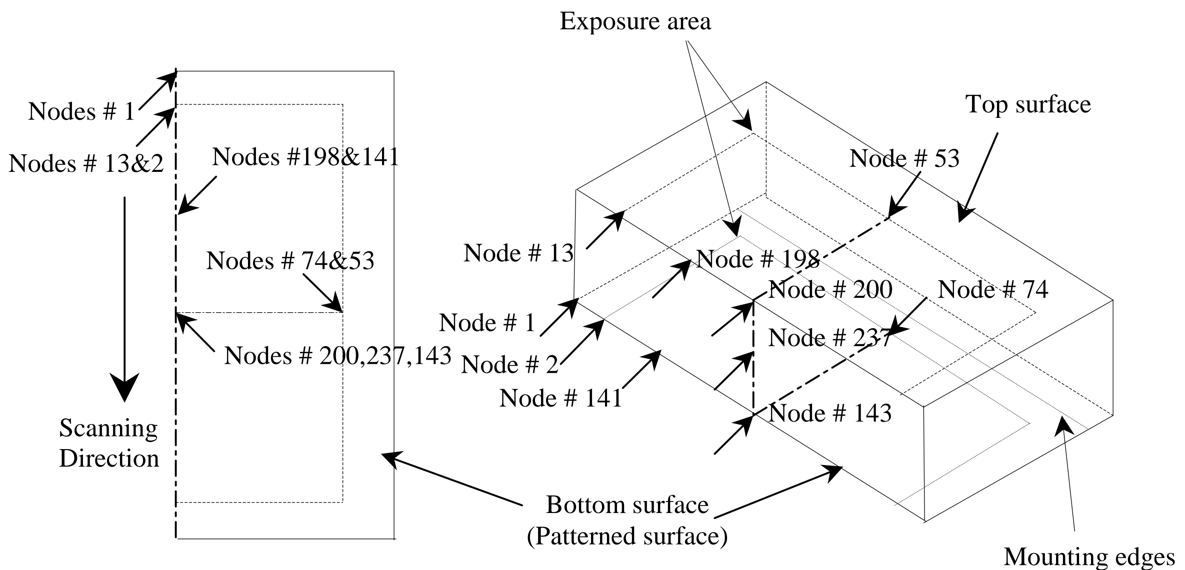

Figure 7.7 Schematic of the mask model showing the relative positions of the nodes.

Figure 7.7 shows the positions of the ten nodes used for presenting the results. The nodes were selected to be sure that the equivalent model is doing a good job in predicting the thermal behavior of the mask during scanning exposure. Both modeling techniques are meshed similarly so that Figure 7.7 represents both models.

Comparing Figure 7.5, the detailed scanning model TDSM with Figure 7.6, the equivalent scanning model TDFM, it can be seen that the only difference in the results is that the TDSM shows more small details, i.e., small peaks, each peak representing one complete scan. These peaks are averaged in the TDFM. The equivalent model is significantly faster from a computational viewpoint relative to the detailed scanning model. To demonstrate the computational saving, the number of load steps is calculated. For the detailed scanning modeling the results represented in chapter five, one wafer completion step is equivalent to (N_{steps}+1) steps (i.e., N_{steps} steps, in each step the load is applied on a strip, and the one step after those is the time delay load step). The resulting number is multiplied by the number of scans N_{scan} to get the total load steps required for one wafer exposure, or numerically (27+1) multiplied by 30 which is 840 load steps each wafer. One load step in the equivalent model TDFM shown, i.e., one peak shown in Figure 7.6, represents 840 load steps (using the parameters given in Table 5.2).

In order to understand the importance of using the TDFM instead of the TDSM from the computational time and required storage saving point of view a test run was performed using a half symmetry model with course grid (N_{steps} =6) to perform 30 scans per wafer for 10 wafers, the solution using TDSM needed 2 hours to be finished, 12.9 MB storage space. For the same half symmetry model but using the TDFM the solution needed only 8 minutes with 3.8 MB storage space, and by using a quarter symmetry model the solution takes only 5 minutes and 2.8 MB storage space. These runs were performed on a Pentium® II 450 MHz CPU with Windows NT ® operating system.

Based on the comparison of Figures 7.5 and 7.6 one can conclude that the equivalent scanning modeling technique for the scanning exposure, the TDFM, is doing a very good job and can be used for modeling the actual scanning process. A later section in this chapter presents the scanning exposure results for some cases with different input parameters. The equivalent-scanning model TDFM will be used since it has been shown that a good result can be obtained with this model.

The testing of the equivalent modeling using TDFM was done for the case of scanning using "one strip" scanning discussed in chapter five. The TDFM was also tested for the "overlapping strip" scanning and it was found that the averaging technique also works for this case. For the "overlapping strip" scanning modeling, the input parameters given by equations 7.1 to 7.5 are slightly different. The time duration needed for one step exposure i.e., duration of exposing the light beam before moving forward to another beam position τ_{strip} is given by equation 7.6, while the time needed for completing one scan τ_{scan} is given by equation 7.7.

$$\tau_{strip} = \frac{\tau_{scan}}{(N_{strip} r)} \tag{7.6}$$

$$\tau_{scan} = N_{strip} \tau_{strip} \tag{7.7}$$

Where r is the refinement number explained in section 5.3. Equation 7.8 can be used for calculating the number of step N_{steps} needed to complete one scan.

$$N_{steps} = [N_{strip} r + (r-1)] \tag{7.8}$$

Equation 7.9 is used for calculating the equivalent time during which the equivalent light must be "on" and equation 7.10 calculates the equivalent time where the equivalent light must be "off".

$$\tau_{on} = [\tau_{scan} N_{scan} + \tau_{delay} (N_{scan} - 1)] \tag{7.9}$$

$$\tau_{off} = (\tau_{delay} + \tau_{wafer}) \tag{7.10}$$

The energy input to the mask during the time needed for completing one wafer can be calculated from equation 7.11 as follows:

$$E = q''_{beam} \{2F + r[r + N_{scan} - (r-1)]\} \tau_{strip} N_{scan} A_{beam} \tag{7.11}$$

Where F is the summation given by equation 7.12 and A_{beam} is the light beam area.

$$F = \sum_{x=1}^{r} x \tag{7.12}$$

The equivalent heat input from the equivalent light that must be used as input in the equivalent model is the energy input during the equivalent time period divided by that time and by the total area, which leads to equation 7.13.

$$q''_{in} = \frac{E}{\{A_{beam} (N_{strip} r) [\tau_{scan} N_{scan} + \tau_{delay} (N_{scan} - 1)]\}} \tag{7.13}$$

Equations 7.6-7.13 are needed for modeling the scanning exposure presented in the next section.

7.3 Modeling the actual scanning exposure process

In this section, the thermal detailed scanning model (TDFM) is used for calculating the temperature behavior of the optical mask during scanning exposure. Figure 7.1 illustrates

the timing in the TDFM used to simulate the scanning exposure. The scanning exposure is approximated as a light flash problem with equivalent input parameters.

Two different mask glass materials are used in the simulation. The first material is fused silica (SiO_2) which is an excellent material for optical mask with wavelengths greater than 157 nm. However, for wavelengths shorter than 157 nm, fused silica become opaque and it can not be used [ref. 7.1]. The other material is calcium fluoride (CaF_2) which is one of the alternative materials proposed to replace fused silica at low input light wavelengths as it has better optical properties at sub-157 nm wavelengths. Starting from this point, two simulations (for the two materials) are always presented. Table 7.3 represents the input parameters common to both materials, while Table 7.4 and 7.5 present the thermal properties of fused silica and calcium fluoride respectively.

The thermal boundary condition used for this simulation is such that a fixed temperature is used for the nodes on the bottom of the mask which are in direct contact with the mounting frame. It is assumed that the mass of the mounting frame is large enough relative to the glass mask, so that the heat by conduction from the mask to the mounting frame is negligible and will not change the mounting frame temperature.

Figure 7.8 represents the thermal result for two nodes from an ANSYS® simulation using SiO_2. These two nodes are the node where the maximum temperature should occur

(central node of the patterned area) and the node where the maximum in plane distortion (IPD) should occur (half way from the free edge of the patterned area).

Table 7.3 Input parameters for the "equivalent to the overlapping strip" scanning model.

Dimensions	Mask outer dimensions	15.24cm (Square)
	Exposure area ($L \times W$)	12.8cm× 10.0cm
	Distance between mounting edges	11.7 cm
	Mask thickness	0.635 cm
Applied load	Actual lighting power	0.1 W/cm^2
	Equivalent Lighting power	Equation 7.12
Pattern characteristics	Glass absorption coefficient	0.4% 1/cm
	Chrome absorptivity	50%
	Chrome coverage	90%
Heat transfer characteristics	Ambient temperature T_∞	300 K
	Top surface emissivity	0.9
	Bottom surface emissivity	0.5
	Top heat transfer coefficient	15e-4 W/ cm^2-K
	Bottom heat transfer coefficient	4e-4 W/ cm^2-K
Model parameters	Modeling method	Equivalent to the Overlapping Strip
	Light beam width δ	21.1 mm
	Refinement number	4
	Scan velocity V	400 mm/sec
	Scan delay	0.1 sec
	Wafer delay	15 sec
	Equivalent light "on"	Equation 7.9
	Equivalent light "off"	Equation 7.10
	Number of field/wafer (n_scan)	30
	Number of wafers (n_wafer)	Till periodic Steady state

Table 7.4 Input thermal properties for Fused Silica.

Material properties (Fused Silica)	Thermal conductivity k	0.0138 W/cm-K
	Density ρ	2202 E-6 g/cm^3
	Specific heat C	746 J/kg-K

Table 7.5 Input thermal properties for Calcium Fluoride.

Material properties (Calcium Fluoride)	Thermal conductivity k	0.097 W/cm-K
	Density ρ	3181 E-6 g/cm^3
	Specific heat C	911.3 J/kg-K

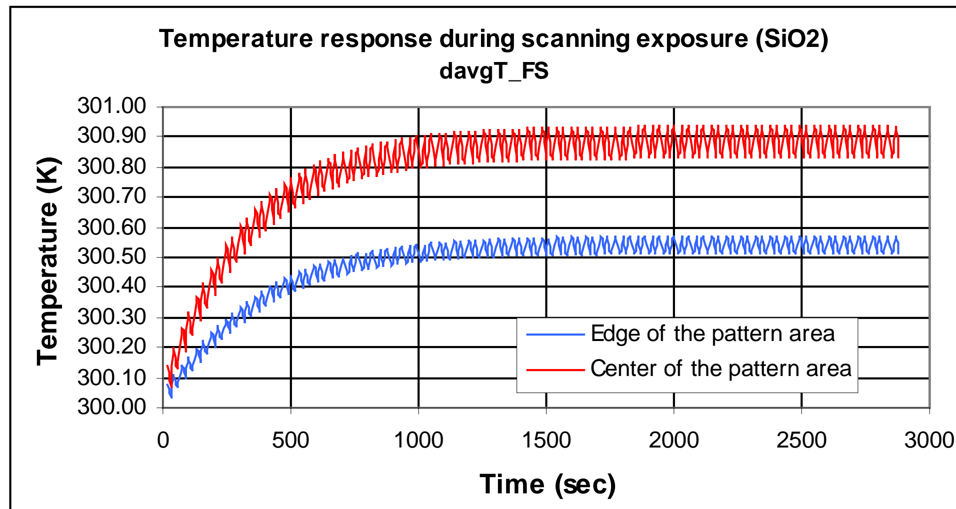

Figure 7.8 Temperature history for SiO_2 using TDFM.

Figure 7.8 also shows that the simulation continued until periodic steady state is reached. The maximum temperature rise is around 0.9 degrees for fused silica.

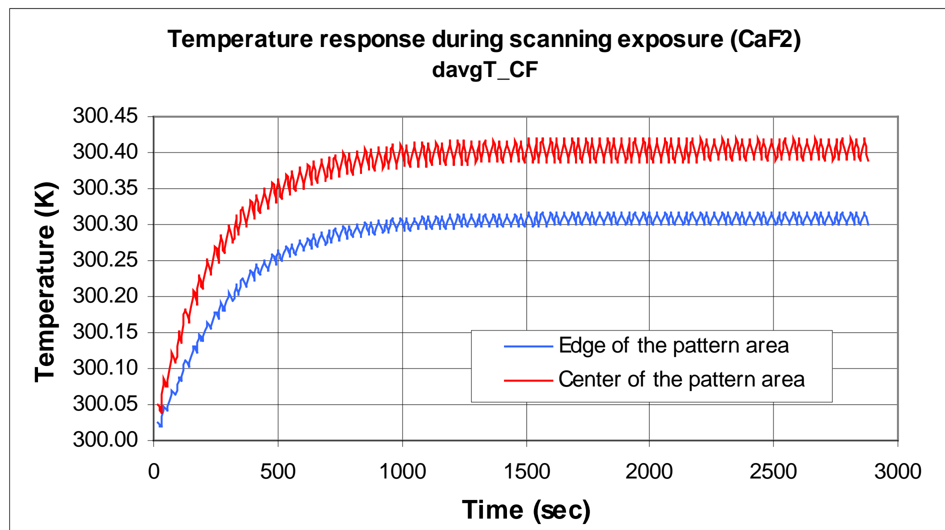

Figure 7.9 Temperature history for CaF_2 using TDFM.

Figure 7.9 shows the temperature history for Calcium Fluoride material, using the same input parameters given in Table 7.3 and the same boundary conditions but with the thermal material properties given in Table 7.5.

From Figures 7.8 and 7.9 it can be seen that the maximum temperature for CaF_2 is almost half of that of SiO_2. This reduced temperature difference is due to the higher thermal conductivity of the CaF_2 (which is more than eight times that of SiO_2). Also seen in these two figures is that the difference between the peak and the valley temperatures in the CaF_2 is lower than that of SiO_2 which is due to the difference in thermal diffusivity of the two materials [ref. 7.2].

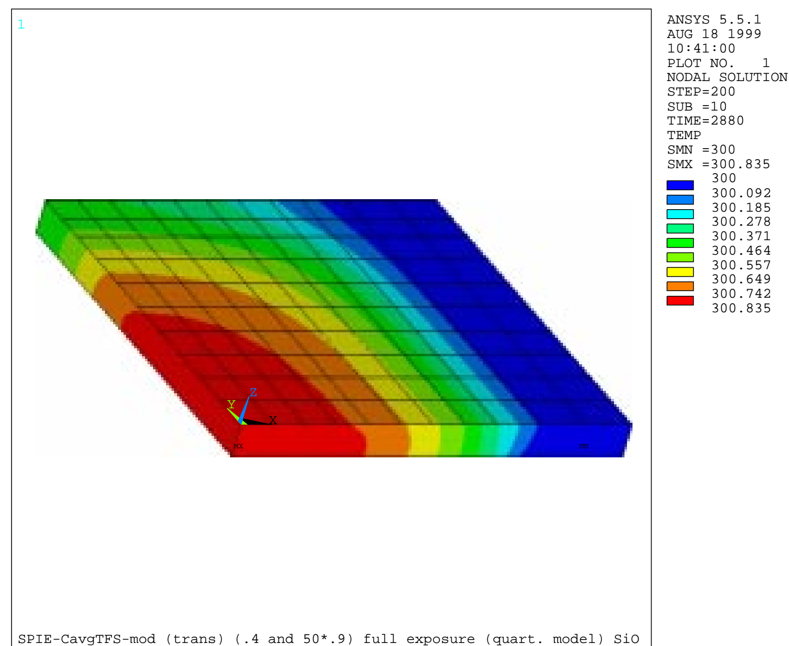

Figure 7.10 ANSYS® temperature contours for SiO_2 at the last step of the simulation.

Figure 7.10 and 7.11 shows the temperature contours at the last step, for both materials. Because of the symmetry condition in the TDFM, a quarter symmetry model is used to cut down the computational time.

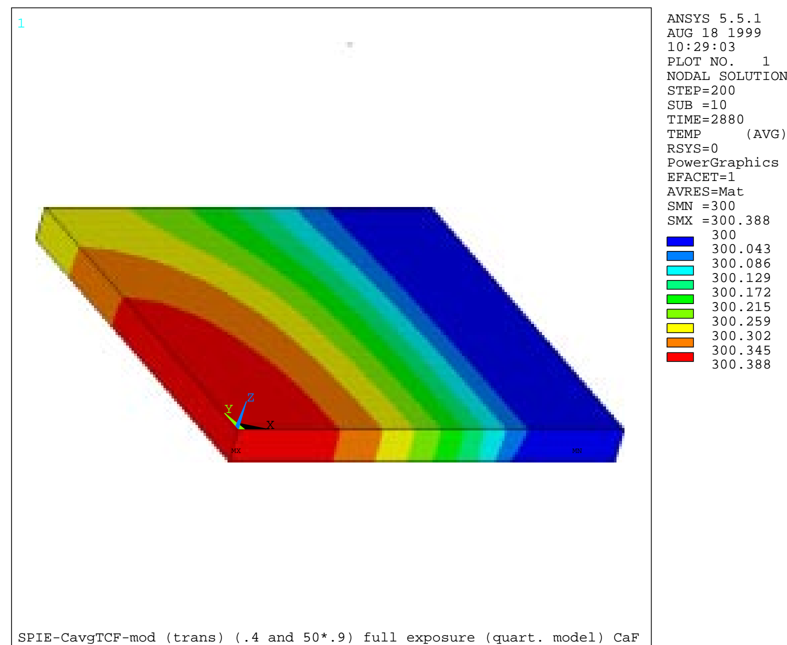

Figure 7.11 ANSYS® temperature contours for CaF_2 at the last step of the simulation.

7.4 Modeling of the actual full field exposure process

As the equivalent model reduced the computational time significantly, it can also be used for cutting the computational time for the full field exposure process. In this section, an equivalent model is used for simulating the full field exposure, Figure 7.12 shows a schematic of the duty cycle used for the modeling. A thermal equivalent-flashing model (TEFM) is used to replace the thermal detailed-flashing model (TDFM) for simulating the full field exposure process to reduce the computational time.

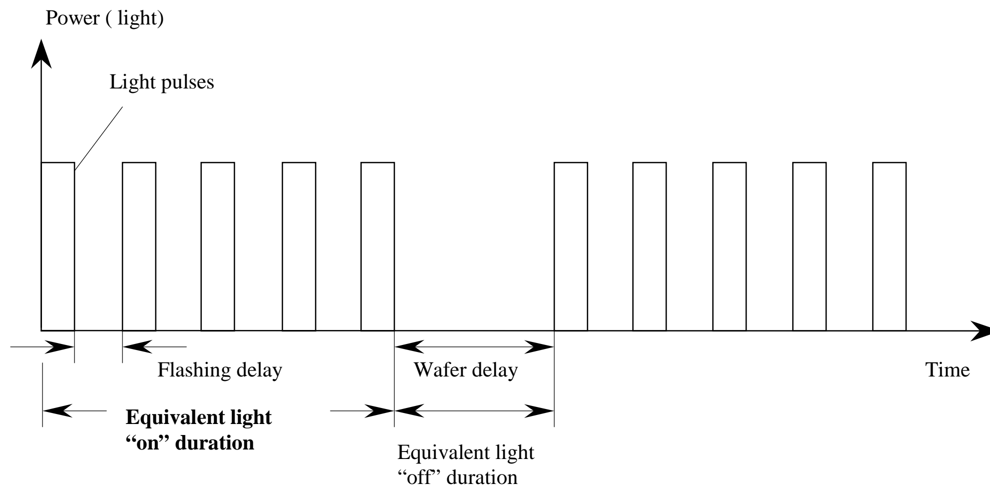

Figure 7.12 Schematic of the duty cycle for the equivalent full field exposure model.

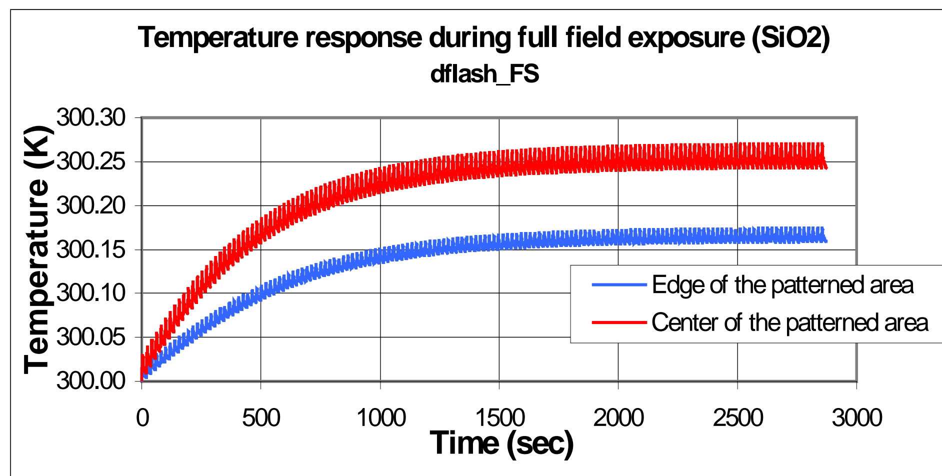

Figure 7.13 Temperature history for SiO_2 using equivalent flashing modelling TEFM.

Figures 7.13 and 7.14 show the temperature history for fused silica and calcium fluoride respectively. The temperature response is represented for two nodes on the chrome patterned (bottom) surface of the mask. These two nodes are where the maximum IPD is expected (the midpoint of the free edge of the patterned surface) and where the maximum temperature is expected (center point on the patterned surface).

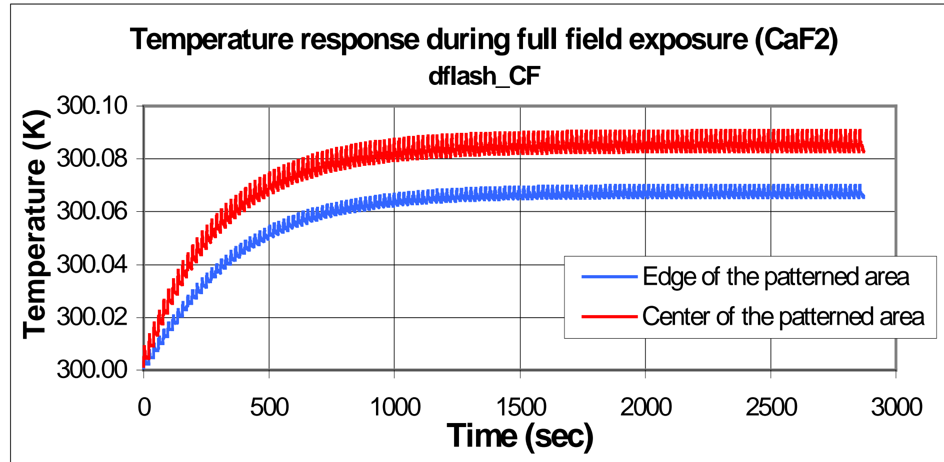

Figure 7.14 Temperature history for CaF_2 using equivalent flashing modeling TEFM.

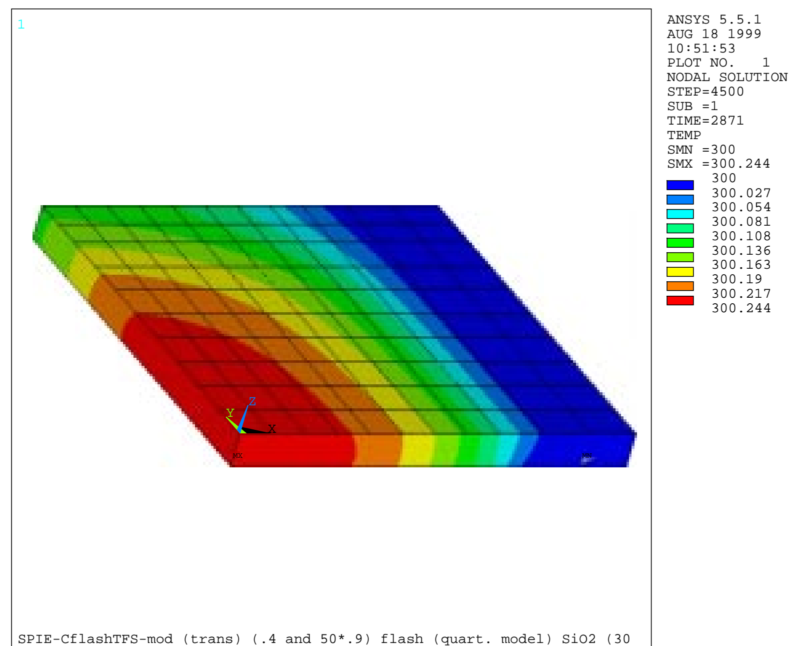

Figure 7.15 ANSYS® temperature contours for SiO_2 at the last step of the simulation.

Figure 7.15 and 7.16 show ANSYS® temperature contour for a quarter symmetry model for both fused silica and calcium fluoride.

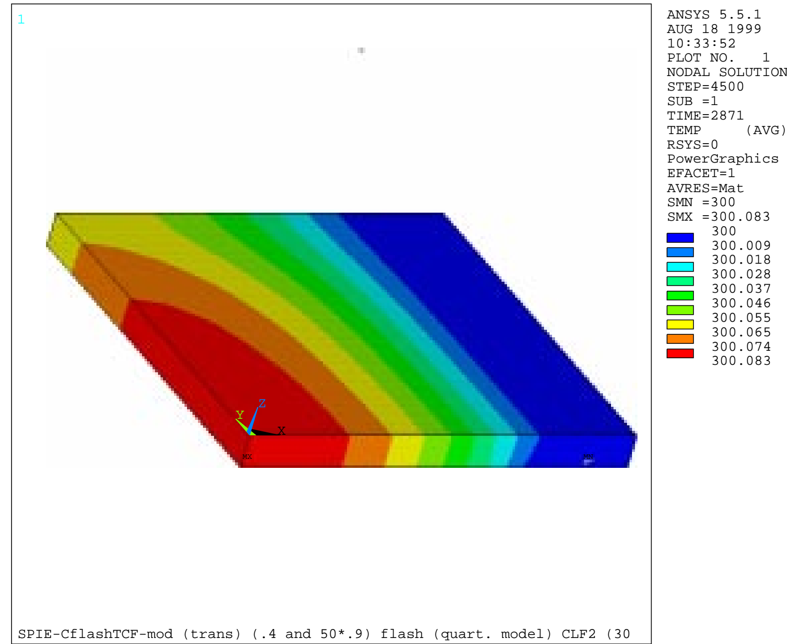

Figure 7.16 ANSYS® temperature contours for CaF_2 at the last step of the simulation.

The main parameters that are needed to be used in the equivalent full field exposure model TEFM are the equivalent power and the "on" and "off" equivalent light application times. The equivalent light power in this case is simple if compared with the case of scanning exposure as the area of exposure is always the same for the actual model and the equivalent model, or in another words the average is just a time averaging. The equivalent heat flux required is given by equation 7.14.

$$q''_{equivalent} = \frac{q''_{beam}\tau_{exposure}N_{flash}}{[\tau_{exposure}N_{flash} + \tau_{delay}(N_{flash} - 1)]} \qquad (7.14)$$

where q''_{beam} is the incident light beam power, τ_{exposure} is the duration of one mask exposure, N_{flash} is the number of flashes per wafer and τ_{delay} is the delay time between lights flashes.

Table 7.6 Input parameters for the "equivalent to the full field exposure" model.

Dimensions	Mask outer dimensions	15.24cm (Square)
	Exposure area ($L\times W$)	12.8cm× 10.0cm
	Distance between mounting edges	11.7 cm
	Mask thickness	0.635 cm
Applied load	Actual lighting power	0.01664 W/cm^2
	Equivalent Lighting power	Equation 7.14
Pattern characteristics	Glass absorption coefficient	0.4% 1/cm
	Chrome absorptivity	50%
	Chrome coverage	90%
Heat transfer characteristics	Ambient temperature T_∞	300 K
	Top surface emissivity	0.9
	Bottom surface emissivity	0.5
	Top heat transfer coefficient	5e-4 W/ cm^2-K
	Bottom heat transfer coefficient	2.5e-4 W/ cm^2-K
Model parameters	Modeling method	Equivalent to the Full field exposure
	Actual exposure time	0.038 sec
	Flash delay	0.1 sec
	Wafer delay	15 sec
	Equivalent light "on"	Equation 7.15
	Equivalent light "off"	Equation 7.16
	Number of field/wafer (n_scan)	30
	Number of wafers (n_wafer)	Till-periodic Steady State

The equivalent light must be "on" during a period of time τ_{on} defined by equation 7.15 and it must be "off" during a period of time τ_{off} defined by equation 7.16.

$$\tau_{on} = [\tau_{exposure} N_{flash} + \tau_{delay}(N_{flash} - 1)] \tag{7.15}$$

$$\tau_{off} = (\tau_{delay} + \tau_{wafer}) \tag{7.16}$$

The times τ_{delay} and τ_{wafer} are the scan delay and wafer delay times given in Table 7.1 and they are shown in Figure 7.1. The input parameters for the equivalent flashing model TEFM are summarized in Table 7.6.

7.5 Summary

In this chapter an equivalent modeling technique is presented to cut down the long computational time needed for the simulation of the thermal response of optical masks during scanning and full field exposures. The thermal detailed scanning model TDSM presented in chapter five, is replaced by an equivalent model, based on the thermal detailed flashing model TDFM used in chapter three. Also to cut down the computational time during full field exposure simulation the thermal detailed flashing model is replaced by an equivalent model thermal equivalent-flashing model TEFM. Equivalent models were tested and used for simulating the actual exposure processes.

7.6 References

[7.1] T. M. Bloomstein, M. W. Horn, M. Rothschield, R. R. Kunz, S. T. Palmacci, and R. B. Goodman, "Lithography with 157 nm lasers," J. Vac. Sci. Technology B 15 (6), pp. 2112-2116, Nov/Dec 1997, ©1997 American Vacuum Society.

[7.2] J. Chang, A. Abdo, B. Kim, T. Bloomstein, R. Engelstad, E. Lovell, W. Beckman and J. Mitchell, "Thermomechanical Distortions of Advanced Optical Reticles during Exposure," Proceedings of the 1999 SPIE symposium on Emerging Lithography Technologies III, Vol. 3676, pp. 756-767, 1999.

Chapter Eight
An equivalent modeling technique to simulate the thermal distortion during scanning and full field exposure processes

8.1 Introduction

In Chapter seven an equivalent modeling technique was developed for the temperature response of both the scanning and full field exposures. The equivalent modeling technique allows simulating the thermal response during scanning exposure with the thermal equivalent scanning model TESM (which is actually the thermal detailed flashing model TDFM) instead of the thermal detailed scanning model TDSM. Also for the full field exposure, the equivalent modeling allows the use of the thermal equivalent flashing model TEFM instead of the thermal detailed flashing model TDFM. In this chapter the averaging technique is extended to calculate the distortion due to the thermal loading. The structural detailed scanning model SDSM is replaced with the average model, the structural equivalent scanning model (or actually the structural detailed flashing model SDFM) and for the full field exposure, the structural detailed flashing model SDFM is replaced by its equivalent model, the structural equivalent flashing model SEFM.

The thermal results represented in the previous chapter are used as input to the structural model to obtain the thermal distortion. Just like the previous chapter, the proposed averaging technique must be tested first. In the next, the comparison between the structural detailed scanning model SDSM with its equivalent model SDFM is presented

as an example for the testes done for checking the equivalent modeling technique. Once the average technique is shown to be valid, it is used for simulating the actual exposure processes. Both scanning exposure and full field exposure for two different mask materials are simulated and presented in the following sections.

8.2 Testing the equivalent modeling

The same test run used in Section 7.2 is used to test the equivalent model for the thermal distortion. The thermal results presented in Section 7.2 are used as input to obtain the thermal distortion for the same nodes shown in Figure 7.7, for both the structural detailed scanning model SDSM and the averaged model using the SDFM.

The input operating parameters are given in Table 7.1 and the material properties are given in Table 8.1. The comparison between the SDSM and the SDFM is presented only for fused silica but it was done also for calcium fluoride. The mechanical boundary condition for this test model is such that the central node in the mid-plane is completely constrained from translation in the three directions. This boundary condition allows the mask to expand freely due to thermal loading. This boundary condition is used for both the detailed model SDSM and the equivalent model SDFM.

Table 8.1 Structural properties for the test run.

Material properties (Fused Silica)	Young's modulus of elasticity E	72.6E5 N/ cm^2
	Poisson's ratio ν	0.164
	Thermal expansion coefficient α	0.51E-6 1/K

Figure 8.1 shows a contour plot of the displacement summation (vector summation) results for the structural detailed scanning model SDSM. The resulting displacement shown in Figure 8.1 as the mask expands freely in all directions is expected as the obvious effect of the boundary conditions used. The mask is only constrained from the central node at the mid plane and it is not constrained from any edge of its edges.

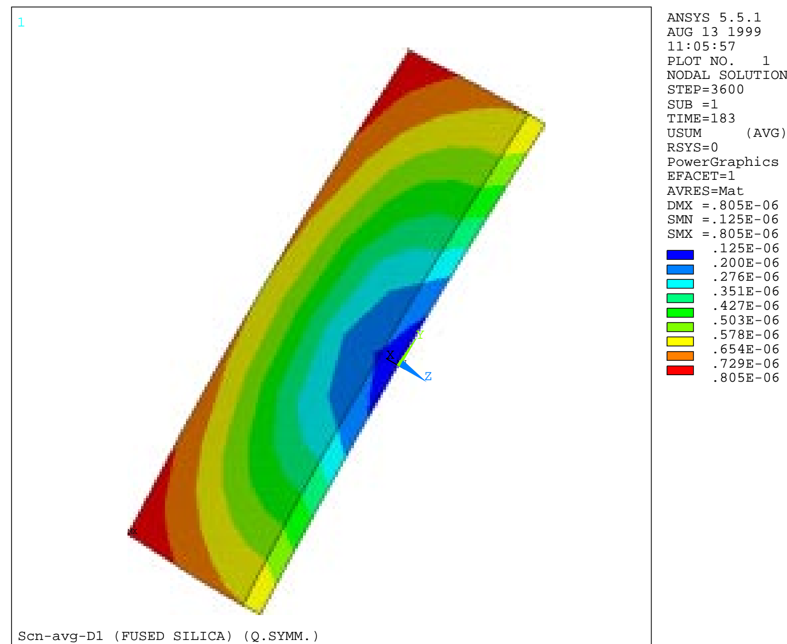

Figure 8.1 Contour plot of vector summation of displacements using the SDSM.

Figure 8.2 shows the same vector summation of the displacement but using the equivalent-scanning model SDFM. By comparing the maximum values in both Figures 8.1 and 8.2 one can see that the difference is 0.4e-8 cm which is less than 0.5% which means that the averaging technique is working very well for this case.

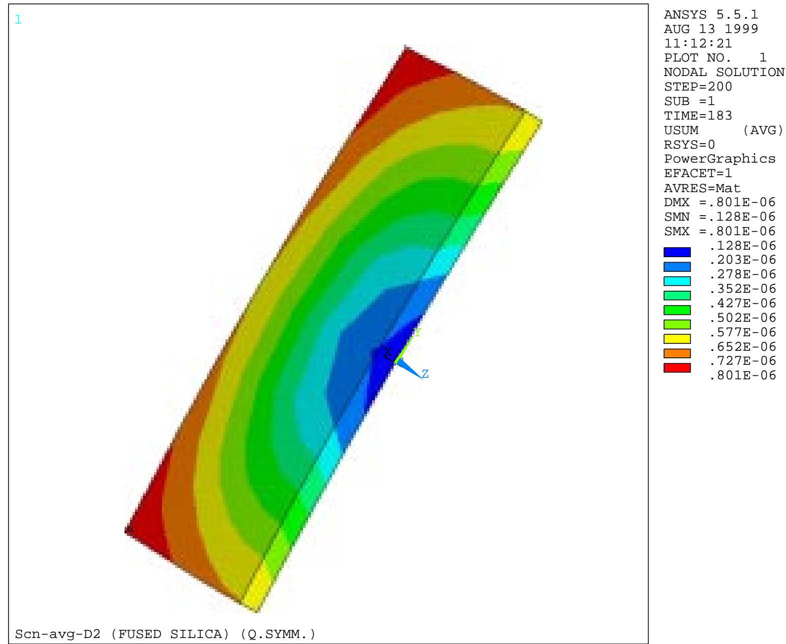

Figure 8.2 Contour plot of vector summation of displacements using the SDFM.

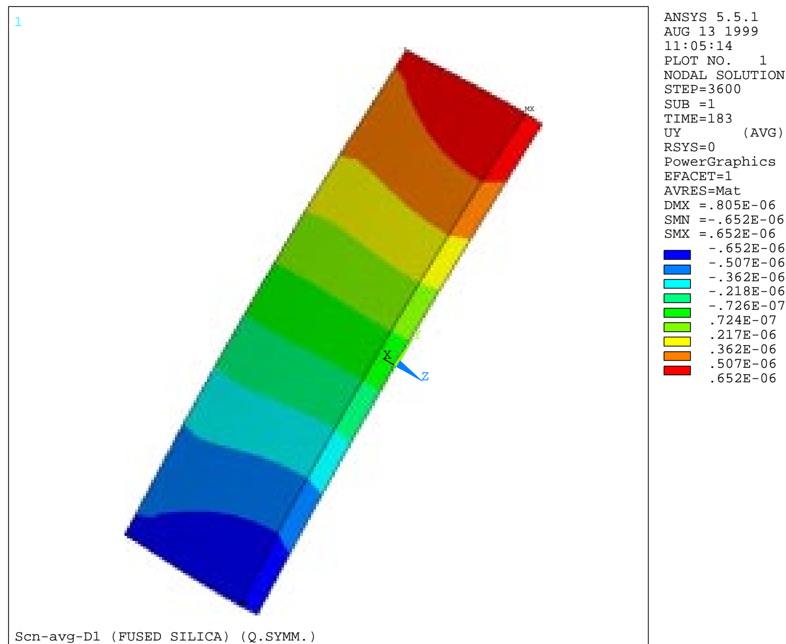

Figure 8.3 Contour plot of maximum IPD (U_y) during scanning using the SDSM.

Figures 8.3 and 8.4 show a contour plot of the maximum in-plane distortion IPD (i.e., the U_y component) for both the structural detailed scanning model SDSM and its equivalent model SDFM respectively. The difference between the SDSM and the SDFM maximum IPD results is only 0.1e-8 cm, which is about 0.15 %. Thus it can be concluded that the equivalent model is accurate enough for this steady-state problem.

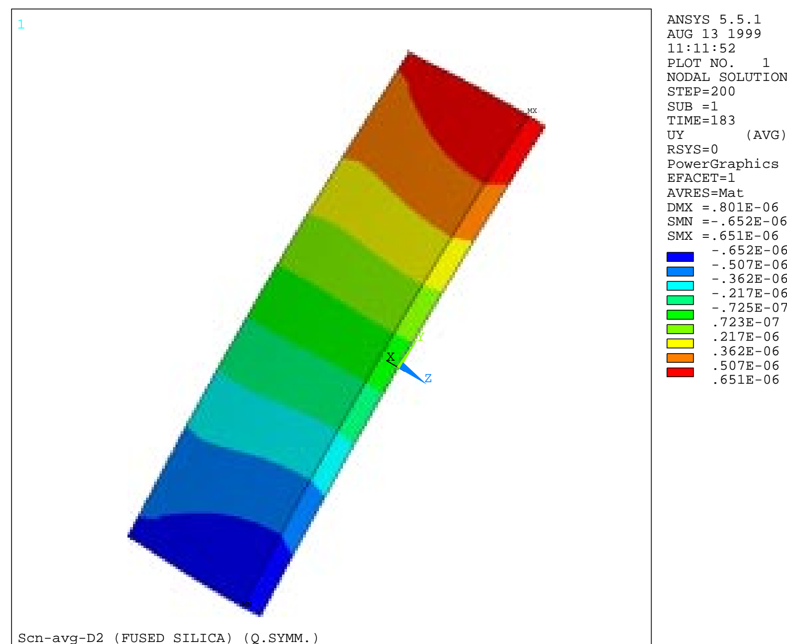

Figure 8.4 Contour plot of maximum IPD (U_y) during scanning using the equivalent model SDFM.

The transient behavior of each node must be compared for both SDSM and SDFM as a final test for gaining confidence in the equivalent modeling technique. Figure 8.5 shows the distortion history for selected nodes (shown in Figure 7.7) for the fused silica mask using the detailed scanning model.

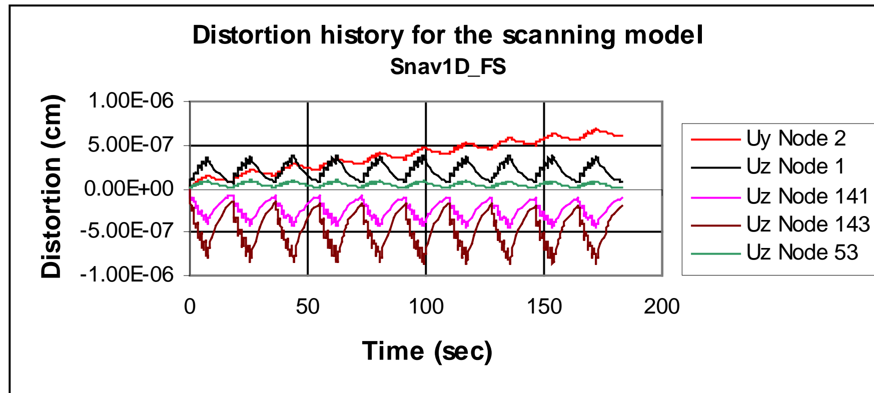

Figure 8.5 Distortion history during scanning using the SDSM.

The distortion history shown in Figure 8.5 corresponds to the thermal results shown in Figure 7.4. The input parameters are those given in Table 7.1 and the structural material properties are given in Table 8.1. Figure 8.6 shows the distortion history for the equivalent scanning model; the structural results correspond to the thermal results given in Figure 7.5 and the node locations are the same shown in Figure 7.7.

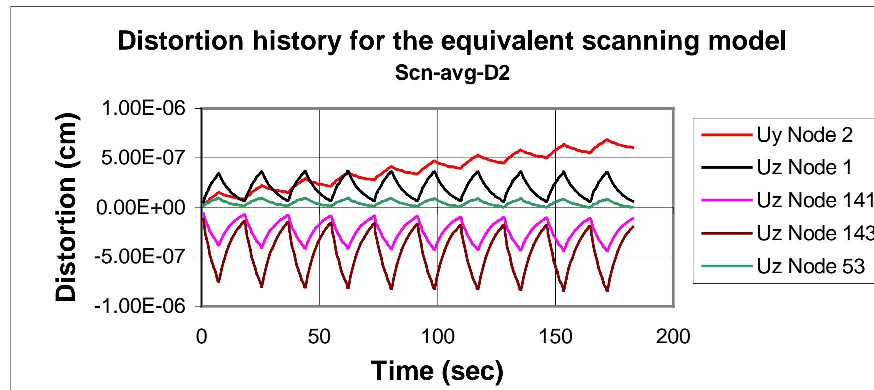

Figure 8.6 Distortion history during scanning using the SDFM.

By comparing the distortion contour plots (Figure 8.1 with 8.2 and 8.3 with 8.4) and the distortion transient history plots (Figure 8.5 with 8.6) one can conclude that the equivalent scanning modeling is doing a good job in predicting the structural behavior of

the optical mask during thermal loading. Since this equivalent modeling technique reduces the computational time significantly, it is used in subsequent calculations for determining the thermal distortion during the actual scanning exposure process.

8.3 Modeling of the actual scanning exposure process

The test problem provides confidence in the performance of the equivalent modeling technique. Consequently, the equivalent modeling technique is used for calculating the thermal distortion of the optical mask during scanning exposure. The thermal results presented Section 7.3 are used as input for the structural model with suitable mechanical boundary conditions for calculating the corresponding thermal distortion. The input parameters are those given in Table 7.3 and the mechanical boundary conditions are such that the strip of nodes that are in contact with the mounting frame are completely constrained from translation in the three directions.

Figure 8.7 shows a contour plot of the maximum IPD at the last step of scanning exposure for fused silica material using the SDFM corresponding to the thermal results shown in Figure 7.15. A quarter symmetry model is used because of the symmetry of the problem and to cut down the computational time. As expected from the nature of the mechanical boundary condition the maximum IPD occurred at the mid-length of the unsupported edge of the mask

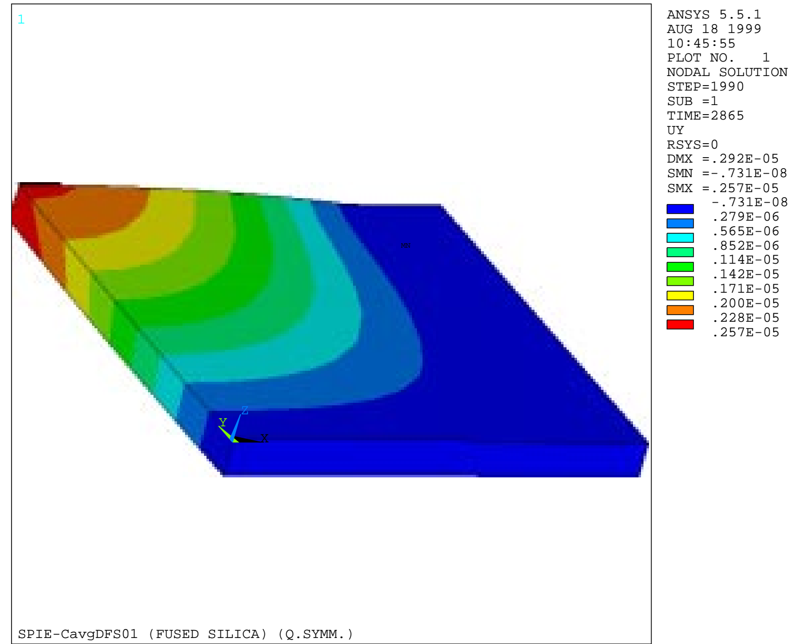

Figure 8.7 IPD contour for a quarter symmetry model for SiO_2 during scanning exposure.

Figure 8.8 shows the contour plot of the IPD distribution for calcium fluoride material during scanning exposure process.

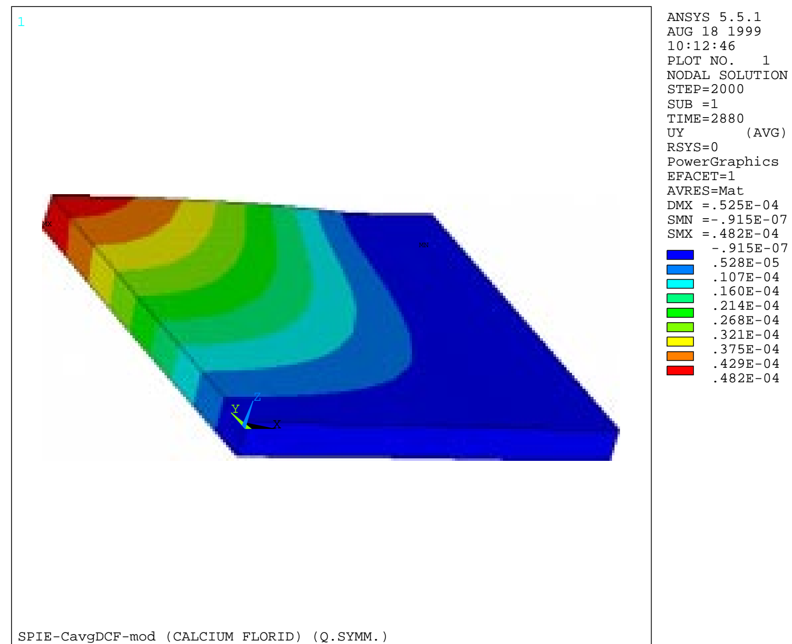

Figure 8.8 IPD contour for a quarter symmetry model for CaF_2during scanning exposure.

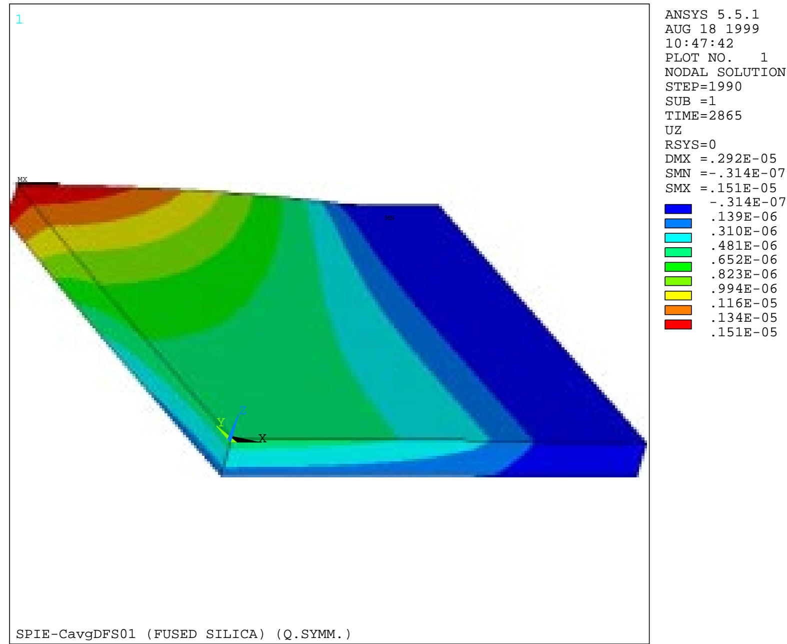

Figure 8.9 OPD contour plot for a quarter symmetry model for SiO_2 during scanning exposure.

The out-of-plane distortions OPD (the z-direction displacement component) for both materials are shown in Figures 8.9 and 8.10, respectively.

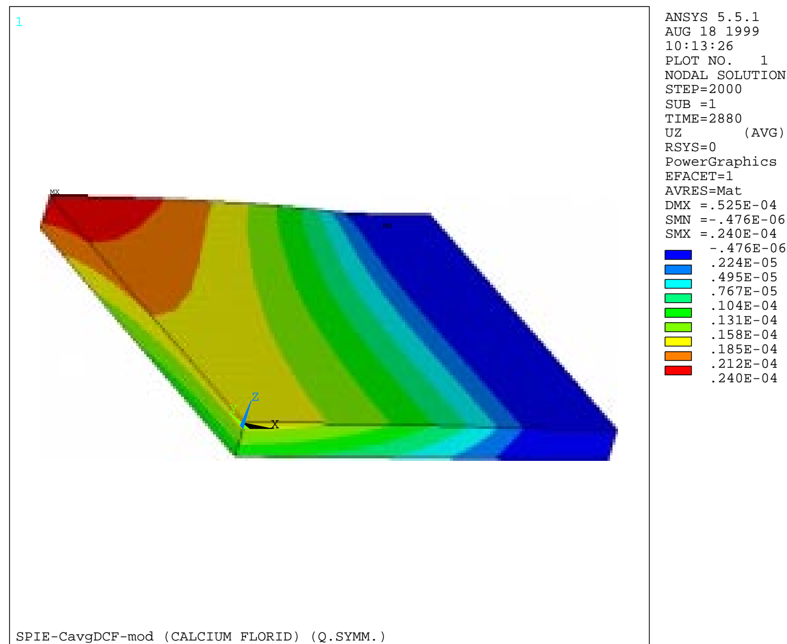

Figure 8.10 OPD contour plot for a quarter symmetry model for CaF_2 during scanning exposure.

A plot of the maximum IPD in the patterned area, which occurred at the middle point of the unsupported length of the glass mask, with time is shown in Figure 8.11 for fused silica material and in Figure 8.12 for calcium fluoride material.

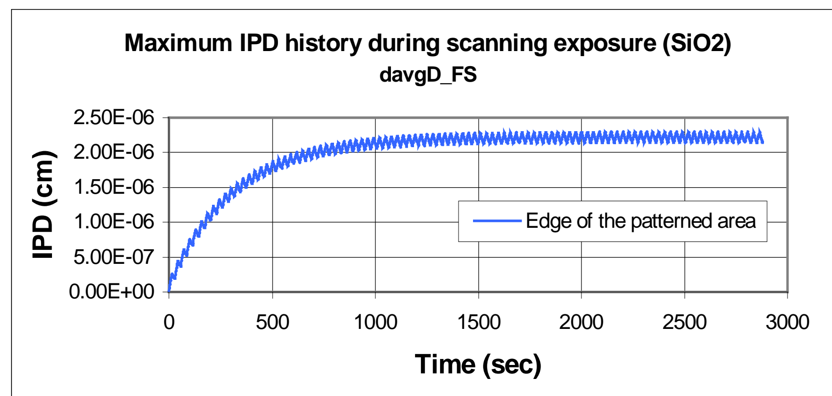

Figure 8.11 Maximum IPD history for SiO_2 during scanning exposure process.

By comparing the periodic steady state value of the IPD for both materials shown in Figures 8.11 and 8.12, it can be noticed that the IPD for CaF_2 is greater than that of SiO_2 by about 20 times (around 22.5 nm maximum distortion for fused silica and 450 nm for calcium fluoride). The reason for the differences is that the coefficient of thermal expansion of calcium fluoride is about 40 times that of fused silica, which means for the same temperature rise the displacement of calcium fluoride should be 40 times that of fused silica. But as the thermal conductivity of calcium fluoride is much higher than that of fused silica (about 8 times higher), the maximum temperature for calcium fluoride is half of that of fused silica; explaining the reason for which the distortion of calcium fluoride is only 20 times that of that of the fused silica. Table 8.2 presents the structural material properties of calcium fluoride. Figures 8.11 and 8.12 are showing the thermal

distortion corresponding to the thermal response given in Figures 7.8 and 7.9. The IPD is presented only for one node on the mask (node number 2 in Figure 7.6) which is the location of maximum IPD.

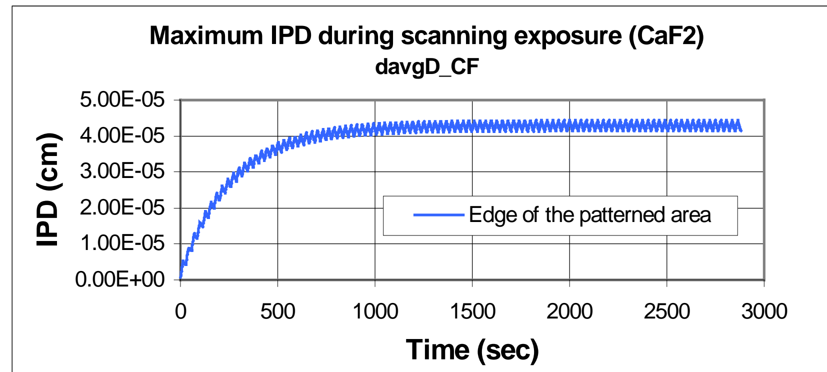

Figure 8.12 Maximum IPD history for CaF_2 during scanning exposure process.

Table 8.2 Structural properties for calcium fluoride.

Material properties (Calcium Fluoride)	Young's modulus of elasticity E	110E5 N/ cm^2
	Poisson's ratio ν	0.29
	Thermal expansion coefficient α	18.9E-6 1/K

8.4 Modeling of the actual full field exposure process

As it was done for the thermal modeling in chapter seven, The averaging technique is used for modeling the distortion response during full field exposure process, in another words, the structural detailed flashing model SDFM is replaced with an average model which is the structural equivalent flashing model SEFM. The thermal results from section 7.4 are used as input to calculate the distortion behavior for both fused silica and calcium fluoride mask materials.

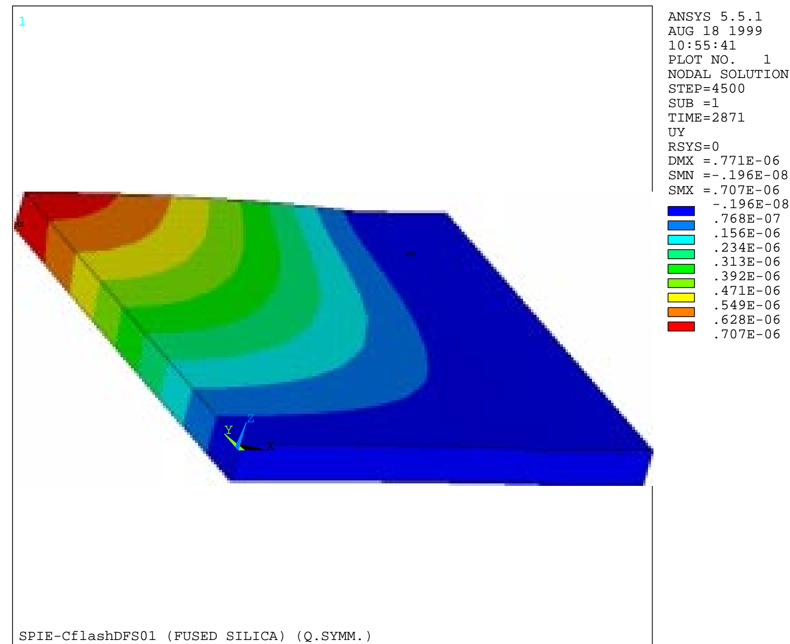

Figure 8.13 ANSYS® contour plot of the IPD of SiO_2
during full field exposure process.

The mechanical boundary conditions used for this model are exactly the same as used for the scanning exposure process. The structural material properties used for fused silica and calcium fluoride materials are both given in Tables 8.1 and 8.2, respectively. The input parameters for this case are given in Table 7.6.

Figures 8.13 and 8.14 show the in-plane distortion IPD contour plot for a quarter symmetry model from an ANSYS® simulation using the averaging model SEFM for fused silica and calcium fluoride material respectively. Figures 8.15 and 8.16 show the out-of-plane distortion (OPD) contour plot for a quarter symmetry model from an ANSYS® simulation using SEFM for both fused silica and calcium fluoride respectively.

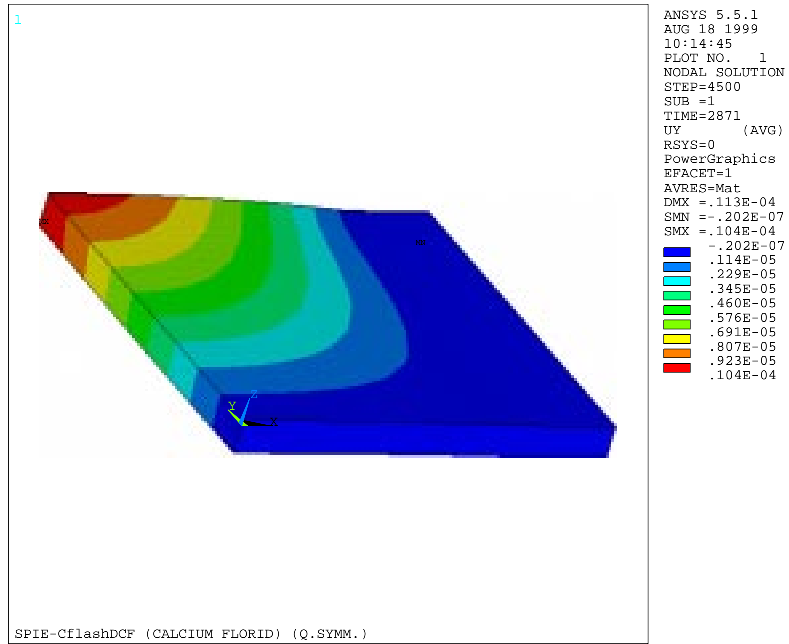

Figure 8.14 ANSYS® contour plot for IPD of CaF_2 during full field exposure process.

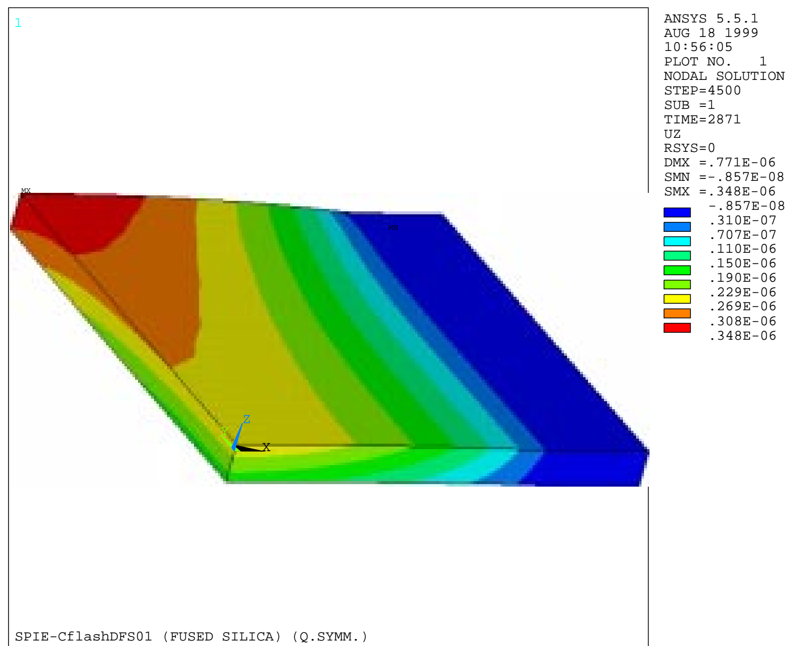

Figure 8.15 ANSYS® contour plot for OPD of SiO_2 during full field exposure process.

From Figures 8.15 and 8.16 one can see that the location of the maximum OPD in the patterned area is the same as that of the maximum IPD, which is the edge of the unsupported length in the optical mask (node number 2 in Figure7.6).

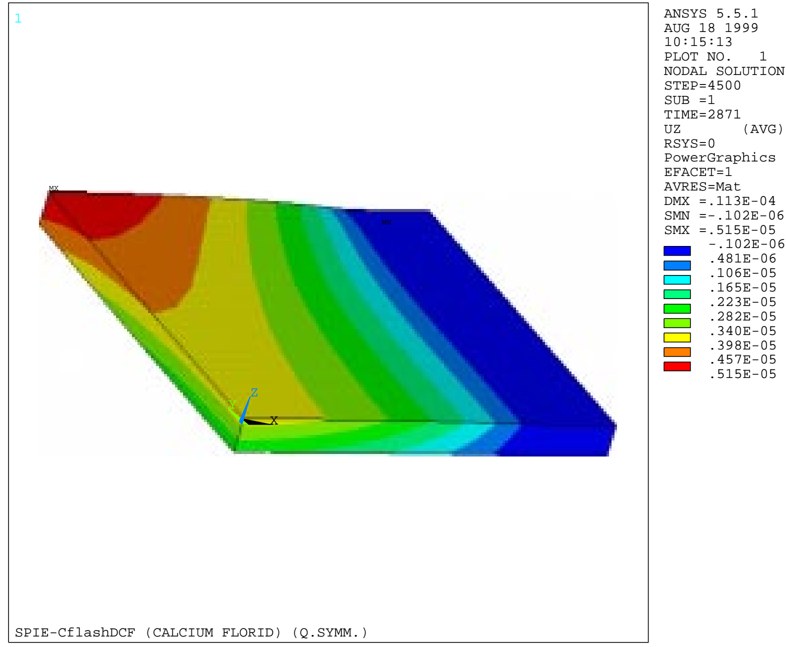

Figure 8.16 ANSYS® contour plot for the OPD of CaF_2 during full field exposure process.

Figures 8.17 and 8.18 represent the maximum IPD history from an ANSYS® transient simulation using the averaging model SDEM for fused silica and calcium fluoride, respectively.

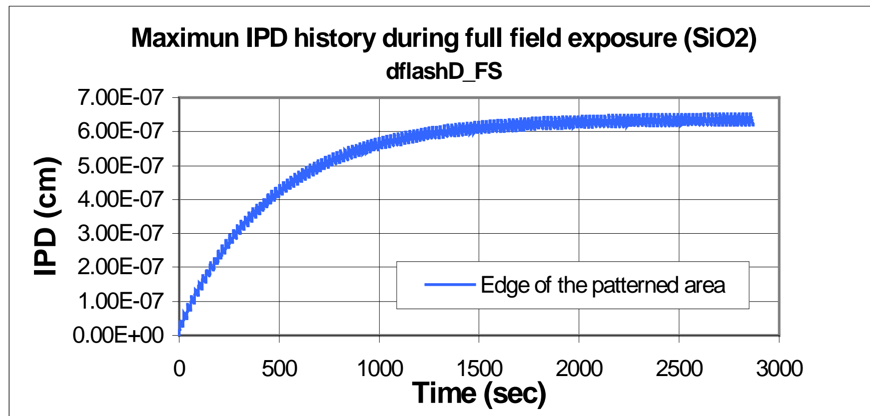

Figure 8.17 Maximum IPD history for SiO_2 during full field exposure process.

Figures 8.17 and 8.18 show that the maximum IPD at the periodic steady state for fused silica is about 6.5 nm while for calcium fluoride it is about 98 nm which is again around the 20 times larger for calcium fluoride than for fused silica.

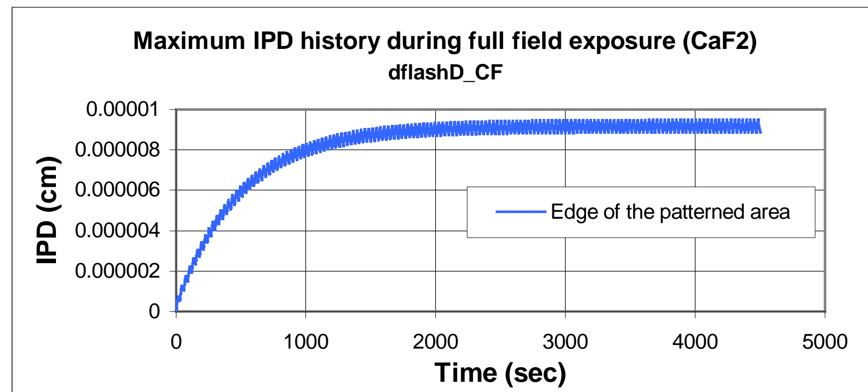

Figure 8.18 Maximum IPD history for CaF_2 during full field exposure process.

8.5 Summary

In this chapter the equivalent modeling technique was shown to be a very good solution for cutting down the large computational time required for the actual exposure processes. The structural detailed scanning model SDSM is replaced with the structural equivalent-scanning model SESM (which is really the structural detailed flashing model SDFM). Also for the full field exposure process, the structural detailed flashing model SDFM is replaced with its equivalent model, the structural equivalent-flashing model SEFM. The test run presented in Section 8.2 with Figures 8.5 and 8.6 shows that the averaging technique works well for the distortion modeling as well as the thermal modeling as shown in chapter 7.

By comparing the structural material properties given in Tables 8.1 and 8.2, one can see that because of the difference in the thermal expansion coefficient between fused silica and calcium fluoride, for the same temperature rise, the distortion for the calcium fluoride should be larger by about 40 times that of fused silica. But as there is a difference in thermal conductivity (given in Tables 7.4 and 7.5), the temperature distribution will not be the same for the same thermal loading in both materials. The result is that the calcium fluoride is about 20 times that of silicon dioxide [ref. 8.1].

The thermal distortion for calcium fluoride is too high for using it as an alternative for the fused silica material.

8.6 References

[8.1] J. Chang, A. Abdo, B. Kim, T. Bloomstein, R. Engelstad, E. Lovell, W. Beckman and J. Mitchell, "Thermomechanical Distortions of Advanced Optical Reticles during Exposure," Proceedings of the 1999 SPIE symposium on Emerging Lithography Technologies III, Vol. 3676, pp. 756-767, 1999.

Chapter Nine
Summary and conclusions

9.1 Summary

In this section a summary of the work represented in this thesis is given. The current work is concerned with the distortion due to the thermal loading on the optical masks during the exposure process. Full field and scanning exposure are both presented in this work (part one and part two respectively). Two glass materials are investigated; fused silica (SiO_2) and calcium florid (CaF_2). Thermal and distortion transient simulations are performed using ANSYS®. Test cases are used to benchmark the ANSYS® models. EES is used to obtain values of analytical and/or finite difference benchmark solution that are compared with ANSYS® finite element models.

Chapter one is an introduction to the lithographic process, Chapter two discusses optical lithography. Chapters three and four form part one, the full field exposure; Chapters five and six form part two the scanning exposure; and Chapters seven and eight form part three the averaging technique. The model averaging technique is used to cut the simulation time for both full field and scanning exposure. As the thermal results are used as inputs to the distortion model, the first chapter in each part is about thermal response and the second chapter is about thermal distortion.

9.2 Conclusions

There are many conclusions in this work. Specific simulation results are given throughout the thesis. In this section general conclusions are briefly discussed.

The most important conclusion is that calcium fluoride can not replace fused silica as optical mask material because the thermal distortion of the calcium fluoride is not acceptable.

The most important modeling conclusion concerns the model averaging technique presented in Chapters seven and eight. The model averaging technique was surprisingly successful in reducing the computational time relative to simulating the full process. For the conditions investigated no meaningful differences exists between the full modeling and the averaging mode.